

UNIVERSITY OF SOUTHAMPTON

Disc Winds Matter: Modelling Accretion and Outflow on All Scales

by

James Matthews

A thesis submitted in partial fulfillment for the
degree of Doctor of Philosophy

in the
Faculty of Physical Sciences and Engineering
Department of Physics & Astronomy

April 2016

“Here, on the edge of what we know, in contact with the ocean of the unknown, shines the mystery and the beauty of the world.

And it’s breathtaking.”

Seven Brief Lessons on Physics, Carlo Rovelli

“Good enough for government work.”

Christian Knigge

UNIVERSITY OF SOUTHAMPTON

Abstract

Faculty of Physical Sciences and Engineering
Department of Physics & Astronomy

Doctor of Philosophy

by James Matthews

Outflows are ubiquitous in accreting systems across 10 orders of magnitude in mass. They can take the form of highly collimated radio jets, or less collimated, mass loaded winds emanating from the accretion disc. Perhaps the most spectacular evidence for accretion disc winds is the blue-shifted, broad absorption lines (BALs) in UV resonance lines, seen in cataclysmic variables (CVs) and approximately 20% of quasars. In addition to directly producing absorption in the spectrum, it is possible that accretion disc winds may significantly affect the line and continuum *emission* from CVs and quasars – as a result, they may even dominate the spectral appearance of such objects. When one considers that disc winds are also a possible mechanism for AGN feedback, it becomes clear that understanding the physics and true spectral imprint of these winds is of wide-ranging astrophysical significance.

In this thesis I use the confusingly named Monte Carlo radiative transfer (MCRT) code, PYTHON, to conduct a series of MCRT and photoionization simulations designed to test simple biconical disc wind models. I provide a detailed description of these methods, focusing particularly on the macro-atom implementation developed by Leon Lucy. First, I apply them to the optical spectra of CVs. Second, I conduct tests of quasar unification models. Finally, informed by the previous study, I use Sloan Digital Sky Survey and Hubble Space Telescope data to test the models in an empirical way, by using emission line equivalent widths as a probe of unification geometries.

Overall, the work presented here suggests that *disc winds matter*. They not only act as a spectral ‘filter’ for the underlying accretion continuum, but may actually dominate the emergent spectrum from accreting objects. As a result, unveiling their driving mechanisms, mass-loss rates, and ionization structure is an important goal for the astronomical community.

Contents

| | |
|--|-------------|
| Abstract | ii |
| List of Figures | vi |
| List of Tables | viii |
| 1 Introduction | 1 |
| 1.1 The Physics of Accretion | 3 |
| 1.1.1 Spherical Accretion and The Eddington Limit | 4 |
| 1.1.2 Accretion Discs | 5 |
| 1.1.2.1 Steady-state Accretion Discs: The α -prescription | 6 |
| 1.1.3 Boundary layers, black hole spin and the ISCO | 7 |
| 1.1.4 The emergent spectrum | 9 |
| 1.2 Accreting Compact Binaries | 11 |
| 1.2.1 Roche Lobe-Overflow | 13 |
| 1.2.2 Cataclysmic Variables | 14 |
| 1.2.2.1 Dwarf Novae and the Disc-instability Model | 15 |
| 1.2.2.2 Nova-like Variables | 15 |
| 1.2.3 Low Mass X-ray Binaries | 16 |
| 1.3 Quasars and Active Galactic Nuclei | 20 |
| 1.3.1 AGN Unification and the dusty Torus | 21 |
| 1.3.2 X-ray Properties of AGN | 24 |
| 1.3.2.1 The Soft X-ray Excess | 25 |
| 1.3.3 The Broad Line Region: Connection to winds and unification | 26 |
| 1.4 The Current Understanding of the Disc Continuum | 26 |
| 1.4.1 The Spectral shape of CV discs | 27 |
| 1.4.2 The Big Blue Bump in AGN | 28 |
| 1.4.2.1 The Accretion Disc Size Problem | 28 |
| 1.4.2.2 Fitting AGN Spectra and the 1000Å Break | 29 |
| 1.5 The Universality of Accretion | 29 |
| 1.5.1 The RMS-flux relation | 30 |
| 1.5.2 Accretion states and disc-jet coupling | 30 |
| 1.5.3 A Global Picture | 31 |
| 2 Accretion Disc Winds | 33 |

| | | |
|----------|---|-----------|
| 2.1 | Observational Evidence | 33 |
| 2.1.1 | Cataclysmic Variables | 34 |
| 2.1.2 | X-ray Binaries | 37 |
| 2.1.3 | AGN and Quasars | 38 |
| 2.1.3.1 | Broad Absorption Line Quasars | 38 |
| 2.1.3.2 | Warm Absorbers | 41 |
| 2.1.3.3 | Ultra-fast Outflows | 42 |
| 2.1.4 | Stellar Winds | 43 |
| 2.1.4.1 | Clumping in Stellar Winds | 44 |
| 2.1.5 | Outflow Physics | 45 |
| 2.2 | Driving Mechanisms | 46 |
| 2.2.1 | Thermal Winds | 47 |
| 2.2.2 | Radiatively Driven Winds | 47 |
| 2.2.3 | Line-driven Winds | 48 |
| 2.2.4 | Magnetic Winds | 49 |
| 2.3 | Accretion Disc Wind Models | 50 |
| 2.3.1 | MCGV95: A Line-driven Wind Model for AGN | 50 |
| 2.3.2 | De Kool & Begelman: A Radiatively Driven, Magnetically Confined Wind | 51 |
| 2.3.3 | Elvis 2000: A Structure for Quasars | 52 |
| 2.3.4 | Proga et al.: Line-driven Hydrodynamic Models for AGN and CVs | 53 |
| 2.4 | A Kinematic Prescription for a Biconical Wind | 55 |
| 2.5 | The big picture: AGN Feedback | 58 |
| 2.5.1 | Observational evidence for feedback | 59 |
| 2.5.2 | Alternative Explanations | 63 |
| 3 | Testing Quasar Unification: Radiative Transfer In Clumpy Winds | 64 |
| 3.1 | Introduction | 64 |
| 3.2 | A Clumpy Biconical Disk Wind Model for Quasars | 65 |
| 3.2.1 | Photon Sources | 65 |
| 3.2.2 | A Simple Approximation for Clumping | 67 |
| 3.2.3 | The Simulation Grid | 70 |
| 3.3 | Results and Analysis From A Fiducial Model | 71 |
| 3.3.1 | Physical Conditions and Ionization State | 71 |
| 3.3.2 | Synthetic Spectra: Comparison to Observations | 74 |
| 3.3.2.1 | Broad absorption lines ('BALQSO-like' angles) | 76 |
| 3.3.2.2 | Broad emission lines ('quasar-like' angles) | 79 |
| 3.3.3 | X-ray Properties | 80 |
| 3.3.4 | LoBALs and Ionization Stratification | 81 |
| 3.4 | Discussion | 83 |
| 3.4.1 | Parameter Sensitivity | 83 |
| 3.4.2 | Inclination Trends: FWHM and EW | 83 |
| 3.4.2.1 | FWHM and Black Hole Mass Estimates | 86 |
| 3.5 | Summary And Conclusions | 87 |
| 4 | Quasar Emission Lines as Probes of Orientation and Unification | 89 |
| 4.1 | Introduction | 89 |

| | | |
|---------------------|---|------------|
| 4.2 | Data Sample | 90 |
| 4.3 | The Angular Distribution of Emission from an Accretion Disc | 93 |
| 4.3.1 | Standard Thin Disc Models | 94 |
| 4.3.2 | Including GR, Comptonisation and Opacity Effects | 94 |
| 4.4 | Predicted EW distributions compared to observations: A Monte Carlo approach | 94 |
| 4.5 | Discussion | 98 |
| 4.5.1 | Eigenvector 1 | 98 |
| 4.5.2 | Radio Observations | 100 |
| 4.5.3 | Polarisation | 100 |
| 4.5.4 | Theoretical Considerations | 101 |
| 4.6 | Conclusions | 101 |
| 5 | Conclusions | 105 |
| 5.1 | Suggestions for Future Work | 105 |
| 5.1.1 | CVs as Accretion and Outflow Laboratories | 105 |
| 5.1.2 | Improving the Treatment of Clumping | 105 |
| 5.1.3 | Expanding the Capabilities of PYTHON | 105 |
| 5.1.4 | Obtaining Reliable Orientation Indicators | 105 |
| 5.2 | Closing Remarks | 105 |
| Bibliography | | 106 |

List of Figures

| | | |
|------|--|----|
| 1.1 | The temperature profile of an accretion disc for three different classes of compact object. | 8 |
| 1.2 | Angular velocity as a function of radius in an accretion disc around a rotating compact object. | 9 |
| 1.3 | The radius of the ISCO, R_{ISCO} , and the horizon, R_H , is as a function of the BH spin parameter, a_* | 10 |
| 1.4 | Accretion disc SEDs for three different compact objects. | 10 |
| 1.5 | A comparison between an accretion disc spectrum computed with black-body and stellar atmosphere spectra. | 11 |
| 1.6 | Artists impression of an LMXB and CV. | 12 |
| 1.7 | The Roche potential in a binary system | 14 |
| 1.8 | A year in the life of SS Cyg. | 16 |
| 1.9 | Spectra of SS Cyg during an outburst cycle | 17 |
| 1.10 | Optical spectra of three nova-like variables. | 18 |
| 1.11 | UV spectrum of RW Tri in and out of eclipse. | 19 |
| 1.12 | Template spectra, from the AGN atlas, for four common types of AGN. . | 22 |
| 1.13 | A unified scheme for AGN. | 23 |
| 1.14 | Broadband SEDs for different AGN SEDs | 24 |
| 1.15 | Occam's quasar | 27 |
| 1.16 | Hardness-intensity diagrams for three types of accreting objects. | 32 |
| 2.1 | Diagram showing how an expanding envelope or wind with significant line opacity around a continuum source leads to the formation of P-Cygni profiles. The black arrows denote the outflow direction and the blue arrows typical scattering interactions. | 34 |
| 2.2 | UV spectrum of the DN TW Vir during outburst. | 35 |
| 2.3 | UV spectrum of Z Cam, compared to a synthetic spectrum from MCRT simulations. | 35 |
| 2.4 | The effect of a disc wind on a double-peaked line profile. | 36 |
| 2.5 | A cartoon illustrating the expected geometry of soft-state LMXB winds. . | 37 |
| 2.6 | Hardness-intensity diagram for four dipping LMXBs. | 38 |
| 2.7 | Five examples of BAL quasar spectra, from HST and SDSS. | 39 |
| 2.8 | X-ray spectrum of PDS 456 fitted with a P-Cygni profile. | 44 |
| 2.9 | UV spectrum of one of the O4 supergiant ζ Puppis. | 45 |
| 2.10 | Cartoon showing the geometry of the MCGV95 model. | 51 |
| 2.11 | A cartoon showing the components in the De Kool & Begelman model. . | 52 |
| 2.12 | A schematic showing the main features of the Elvis model. | 53 |
| 2.13 | Density snapshot of the PK04 model. | 54 |

| | |
|---|-----|
| 2.14 A schematic showing the geometry and kinematics of the SV93 model | 56 |
| 2.15 The SV93 velocity law for various values of the acceleration exponent, α | 58 |
| 2.16 The $M_{BH} - \sigma_*$ correlation. | 60 |
| 2.17 The $M_{BH} - M_{bulge}$ correlation. | 60 |
| 2.18 Figure adapted from Fabian 2012. Chandra X-ray images showing two examples of X-ray cavities, illustrating how a radio jet from an AGN can have a dramatic impact on its environment. a) The RBS 797 Cluster (Cavagnolo et al. 2011). b) elliptical galaxy NGC 5813 (Randall et al. 2011). | 61 |
| 2.19 Results of Gaussian line profile fitting to integral field spectroscopy of Mrk 231. | 62 |
| | |
| 3.1 A cartoon showing the geometry and some key parameters of our biconical quasar wind model. | 66 |
| 3.2 The input spectrum used for our quasar modelling. | 67 |
| 3.3 Some typical length scales for the fiducial model. | 69 |
| 3.4 Contour plots showing the logarithm of some important physical properties of the quasar outflow. | 72 |
| 3.5 The electron density in the fiducial model on linear axes. | 73 |
| 3.6 Synthetic spectra at four viewing angles for the fiducial quasar model. | 75 |
| 3.7 A schematic showing the broad classes of sightline in the fiducial model. | 76 |
| 3.8 Synthetic spectra at two viewing angles compared to the non-BAL SDSS quasar composite. | 77 |
| 3.9 X-ray properties of the clumped quasar model compared to H13 and samples from the literature. | 80 |
| 3.10 C IV, Mg II, Al III and Fe II line profiles for wind viewing angles. | 82 |
| 3.11 Equivalent widths and BALnicities of some important lines for the quasar wind grid. | 84 |
| 3.12 $W_{\lambda, RW}$ as a function of inclination in the fiducial model. | 85 |
| 3.13 f_{FWHM} as a function of inclination | 87 |
| | |
| 4.1 BH mass and Eddington fraction for the BAL samples plotted over the overall quasar sample from S11. | 91 |
| 4.2 Histograms of equivalent widths for three emission lines from the two different samples. | 92 |
| 4.3 Monochromatic continuum luminosities from AGNSPEC and classical thin disc models. | 95 |
| 4.4 The geometry of the toy model used to carry out the Monte Carlo simulations | 96 |
| 4.5 Contour plots from the Monte Carlo simulations. | 97 |
| 4.6 Eigenvector 1 for BAL and non-BAL quasars. | 100 |
| 4.7 LoBAL fraction compared to mean LoBAL fraction in Eigenvector 1 space. | 101 |
| 4.8 Top: Polarisation percentages as a function of measured inclination from Marin et al. (2015) for Type I and Type II AGN. Bottom: Histograms of polarisation percentages for BAL quasars from Schmidt et al. (1999) together with the Marin et al. (2015) AGN sample. | 102 |

List of Tables

| | | |
|-----|---|----|
| 3.1 | The grid points used in the parameter search for quasar wind models | 71 |
| 3.2 | Model parameters for the fiducial quasar model. | 73 |
| 3.3 | Some derived spectral properties of the fiducial model compared to ob- servations. | 78 |
| 4.1 | Eigenvector 1 correlation coefficients | 98 |

Dedicated to my family. Thanks for being awesome....

Chapter 1

Introduction

“And now you’re asking, I don’t know where to begin”

Mike Vennart, *Silent/Transparent*

The release of gravitational potential energy as mass falls towards a compact object is the most efficient energetic process in the universe, even more efficient than nuclear fusion. This *accretion* process is thought to power the huge radiative engines at the centres of many galaxies – accreting supermassive black holes known as active galactic nuclei (AGN). As the matter falls into the potential well of the black hole it often forms an accretion disc. This disc is an efficient radiator of the gravitational potential energy released. and can sometimes outshine the entire stellar population of the galaxy, appearing as a quasi-stellar object (QSO) or *quasar*. As well as powering, AGN, accretion discs are present in X-ray binaries (XRBs), young-stellar objects (YSOs) and cataclysmic variables (CVs). Accretion is a universal process; broadly speaking, the physics is similar regardless of whether matter is falling on to a $\sim 1 M_\odot$ neutron star or white dwarf, or a $\sim 10^{10} M_\odot$ black hole.

Outflows are ubiquitous in accreting systems. We see collimated radio jets in AGN (Hazard et al. 1963; Potash & Wardle 1980; Perley et al. 1984; Marscher 2006) and XRBs (Belloni 2010), and there is even evidence of radio emission in CVs (Benz et al. 1983; Coppejans et al. 2015). These radio jets tend to appear in specific accretion states (Fender 2001; Fender et al. 2004; Körding et al. 2008), implying an intrinsic connection to the accretion process. Even more intriguing, in XRBs less collimated, mass-loaded

outflows or *winds* are observed in the opposite accretion state, possibly emanating from the accretion disc. Evidence for disc winds is widespread across the mass range, but perhaps the most spectacular indication is the blue-shifted, broad absorption lines (BALs) in the rest-frame ultraviolet (UV) seen in high-state CVs (Heap et al. 1978; Greenstein & Oke 1982; Cordova & Mason 1982) and the so-called broad absorption line quasars (BALQSOs) that make up 20 – 40% of quasars (Weymann et al. 1991; Knigge et al. 2008; Allen et al. 2011). BALs and ‘P-Cygni’ profiles (Struve 1935; Rottenberg 1952) are also seen in stellar winds (e.g. Cassinelli 1979) and sometimes even in the optical spectra of CVs (Patterson et al. 1996; Ringwald & Naylor 1998; Kafka & Honeycutt 2004). Broad, blue-shifted absorption is also observed in the Fe K α line in some AGN (Reeves et al. 2003; Pounds & Reeves 2009; Tombesi et al. 2010) – these are known as ultra-fast outflows or UFOs.

The astrophysical significance of disc winds extends, quite literally, far beyond the accretion environment. They offer a potential mechanism by which the central accretion engine can interact with the host galaxy and interstellar medium via a ‘feedback’ mechanism (King 2003; Fabian 2012). Feedback is required in models of galaxy evolution (Springel et al. 2005) and may explain the famous ‘ $M_{BH} - \sigma$ ’ (Silk & Rees 1998; Häring & Rix 2004) and ‘ $M_{BH} - M_{bulge}$ ’ (Magorrian et al. 1998) relations. Winds also offer a natural way to *unify* much of the diverse phenomenology of AGN, CVs and XRBs. This principle of unification can be applied along more than one ‘axis’ of parameter space. For example, there exist elegant models that attempt to explain *all* of the behaviour of quasars with only a central black hole, a jet, an accretion disc, and an associated outflow, just by varying the viewing angle (Elvis 2000). Similarly elegantly, it has been shown that much of the behaviour of XRBs is directly applicable to AGN (McHardy et al. 2006), and models of outflows in CVs have been successfully ‘scaled-up’ and applied to quasars and AGN (e.g. Higginbottom et al. 2013).

Despite their clear importance and ubiquity, there are still many unanswered questions relating to the true impact of winds and their underlying physical origins. Here, I aim to address some of these questions, and take steps towards building a more holistic picture of the impact of winds on the spectral appearance and accretion physics of disc systems. This thesis is structured as follows. In the remainder of this chapter, I will give the background accretion theory and detail the successes and failures of accretion disc models when compared to observations, as well as describing the different classes

of accreting objects in more detail. In chapter 2, I dedicate some time to specifically discussing the theory of, and observational evidence for, accretion disc winds. In chapter 3, I outline the Monte Carlo radiative transfer (MCRT) and photoionization methods I have used in order to investigate the impact of disc winds on the spectra of accreting systems. The next three chapters contain three separate submitted papers, in which I discuss the impact of disc winds on the spectra of CVs (Chapter 4), and test disc wind quasar unification models (Chapters 5 and 6). In chapter 8, I summarise my findings and their astrophysical significance, and discuss potential avenues for future work.

1.1 The Physics of Accretion

The basic phenomenon of accretion- matter falling into a gravitational potential well- is ubiquitous in astrophysics. The energy, ΔE , released by a parcel of mass, Δm , falling from infinity onto an object of mass M and radius R_* is given by

$$\Delta E = \frac{GM\Delta m}{R_*}, \quad (1.1)$$

meaning that the power by mass accreting at a rate \dot{M} is given by

$$L_{acc} = \frac{GM\dot{M}}{R}. \quad (1.2)$$

We can also characterise the efficiency of any energetic process by relating the energy released to the rest mass energy of the parcel of mass, such that

$$\Delta E = \eta\Delta Mc^2, \quad (1.3)$$

where η is the radiative efficiency. Similarly, in terms of luminosity, L ,

$$L = \eta\dot{M}c^2, \quad (1.4)$$

Nuclear fusion is one of the more efficient energetic processes in the universe, with an efficiency of $\eta = 0.007$. If we rearrange the above equations in terms of η we find

$$\eta = \frac{G}{c^2} \frac{M}{R_*}. \quad (1.5)$$

In other words, the efficiency of accretion is directly related to the *compactness*, M/R_* , of the central object.

1.1.1 Spherical Accretion and The Eddington Limit

The simplest geometry one might propose for accretion would be one in which a central mass accretes matter from an all-encompassing cloud. The process of spherical accretion has come to be known as Bondi-Hoyle-Lyttleton accretion ([Hoyle & Lyttleton 1939](#); [Bondi & Hoyle 1944](#)). In particular, [Bondi \(1952\)](#) studied spherically symmetric accretion onto a point mass and derived the Bondi radius,

$$r_B = \frac{GM}{c_S^2}, \quad (1.6)$$

where $c_S = c_S(r_B)$ is the sound speed as a function of radius. The Bondi radius represents a critical point inside which the material is supersonic and will accrete on the free-fall timescale.

When this timescale is long enough, the accreting matter can radiate away its potential energy, generating a luminosity L . This radiation will induce a force on electrons, given by

$$F_{rad} = \frac{L\sigma_T}{4\pi r^2 c}, \quad (1.7)$$

where $\sigma_T = 6.65 \times 10^{-25} \text{ cm}^2$ is the Thomson cross-section. If this radiation force term dominates over the gravitational force, then the material will no longer fall inwards. Consider radiation pressure acting on electron-proton pairs, for which the gravitational force is approximately given by GMm_p/r^2 . Combining this expression with equation 1.7 gives a natural maximum accretion luminosity, known as the *Eddington limit*, of

$$L_{Edd} = \frac{4\pi GMm_p c}{\sigma_T}, \quad (1.8)$$

with an associated Eddington accretion rate of

$$\dot{M}_{Edd} = \frac{L_{Edd}}{\eta c^2}. \quad (1.9)$$

The Eddington limit makes a number of assumptions, namely that the accretion flow is steady, spherically symmetric, ionized, and has its opacities dominated by electron

scattering. Clearly, there are many astrophysical situations where this does not hold. For example, the recent outburst of V404 Cyg showed wildly variable luminosities on short timescales (see, e.g., [Kuulkers et al. 2015](#); [Motta et al. 2015](#), among many, many ATels), and in any binary system or disc dominated system the assumption of spherical symmetry will break down. Nevertheless, the Eddington limit provides a good order of magnitude estimate of the maximum luminosity of an accreting object, and also provides a useful way of parameterising accretion rate, as it scales linearly with mass. It can also be used to characterise the *state* of an accretion disc. In general, sources above $\sim 0.1 L_{Edd}$ find themselves in a ‘soft’ or thin-disc state, whereas for much lower Eddington fractions, sources will possess advection-dominated accretion flows (ADAFs; [Narayan & Yi 1994, 1995](#)). It is also clear that around the Eddington limit radiation pressure must play a major role in determining the disc morphology (see section [2.2.2](#)).

1.1.2 Accretion Discs

In many astrophysical situations – for example, in binary systems and gas clouds orbiting BHs – any accreting matter will possess some net angular momentum. If the medium is dense enough, collisions between particles will be frequent, but the total angular momentum vector of two colliding particles will always be conserved. This provides a mechanism for a gas cloud to relax to its minimum energy state – an accretion disc.

As well as losing gravitational potential energy as it falls towards the central mass, a parcel of matter must also lose its angular momentum. Crucially, accretion discs provide a way for this to happen. If the disc overall maintains the same total angular momentum, it follows that angular momentum must therefore be transported outwards. The mechanism for transporting angular momentum outwards is unknown, and is one of the biggest weaknesses of current accretion disc theory. The most commonly invoked candidate is the magnetorotational instability (MRI; [Balbus & Hawley 1991](#)), in which accretion discs are subject to a strong shearing instability even when the magnetic field is weak. Possible alternative are that the angular momentum is lost via a magneto-hydrodynamic outflow ([Blandford & Payne 1982](#)) or spiral shock waves ([Ju et al. 2016](#)). An efficient mechanism for angular momentum transport is necessary as the viscosity introduced in the next section is generally inefficient in this regard (?).

1.1.2.1 Steady-state Accretion Discs: The α -prescription

The so-called α -disc model developed by [Shakura & Sunyaev \(1973\)](#), hereafter SS73) and [Lynden-Bell \(1969\)](#) is currently the leading candidate for explaining how energy and angular momentum is transported an accretion disc. The starting point for this model is the parameterisation of viscosity, ν' , using the simple form

$$\nu' = \alpha c_s H, \quad (1.10)$$

where H is the scale height of the disc, α is a parameter ≤ 1 and c_s is the sound speed. Viscous torques then allow the conversion of orbital kinetic energy into heat, which can be radiated away. If we make one further assumption, that the accretion rate is constant throughout the disc, we can write down a mass continuity equation valid at all radii, given by

$$\dot{M} \equiv 2\pi R V_R \Sigma = 0, \quad (1.11)$$

where Σ is the surface density at that point. The angular momentum equation then becomes

$$\nu' \Sigma = \frac{\dot{M}}{3\pi} \left[1 - \left(\frac{R}{R_*} \right)^{1/2} \right]. \quad (1.12)$$

The viscous torques throughout the disc cause a local loss of mechanical energy, allowing one to derive (see, e.g. [Frank et al. 1992](#)) a rate of viscous dissipation, per unit area, given by

$$D(R) = \frac{1}{2} \nu' \Sigma (R \Omega')^2. \quad (1.13)$$

Here, $D(R)$ is proportional to the derivative of the angular velocity, $\Omega' = d\Omega/dR$. By combining equations 1.13 and 1.12 we can show that the viscous dissipation rate is

$$D(R) = \frac{GM\dot{M}}{8\pi R^3} \left[1 - \left(\frac{R}{R_*} \right)^{1/2} \right] \quad (1.14)$$

where we have also set the angular velocity to the Keplerian velocity. This expression is independent of viscosity – which is fortunate, because we do not know what value of α to use in equation 1.10. This result comes about because of the implicit assumption that the viscosity regulates the mass accretion rate so as to achieve a steady state.

We can now integrate across both sides of the whole disc to obtain the disc luminosity,

$$L_{disc} = 2 \int_{R_*}^{\infty} D(R) 2\pi R dR = \frac{GM\dot{M}}{2R_*} = \frac{1}{2} L_{acc}. \quad (1.15)$$

This result can also be shown by considering the binding energy of gas at R_* and infinity. From equation 1.14 one can also derive an effective temperature distribution, by setting

$$\sigma T_{eff}^4(R) = D(R), \quad (1.16)$$

which then gives

$$T_{eff}(R) = T_* \left[1 - \left(\frac{R}{R_*} \right)^{1/2} \right]^{1/4}, \quad (1.17)$$

where

$$T_* = \left(\frac{3GMM}{8\pi R_*^3 \sigma} \right)^{1/4}. \quad (1.18)$$

When $R \gg R_*$ this simplifies to

$$T_{eff}(R) = T_* (R/R_*)^{-3/4}. \quad (1.19)$$

Now we have not only derived the total luminosity of an accretion disc, but also the effective temperature profile which will govern the shape of the emergent SED. This temperature profile is shown in figure 1.1 for three different compact objects, assuming an Eddington fraction of 0.2.

1.1.3 Boundary layers, black hole spin and the ISCO

In equation 1.15 I showed that $L_{disc} = 1/2 L_{acc}$. One might then ask: where does the rest of the luminosity go? The answer is dependent on the compact object in question. In an accreting WD, the rotating matter must eventually deposit itself on the surface of the WD. This is illustrated in figure 1.2, which shows the angular velocity as a function of radius in a disc around a compact object rotating with angular velocity Ω_* . The boundary layer (BL) is the region to the left of the dotted line, inside the maximum of Ω_K , the Keplerian angular velocity. The luminosity of the boundary layer is (Frank et al. 1992)

$$L_{BL} = \frac{1}{2} \frac{GM\dot{M}}{R} \left[1 - \left(\frac{\Omega_*}{\Omega_K(R_*)} \right) \right]^2, \quad (1.20)$$

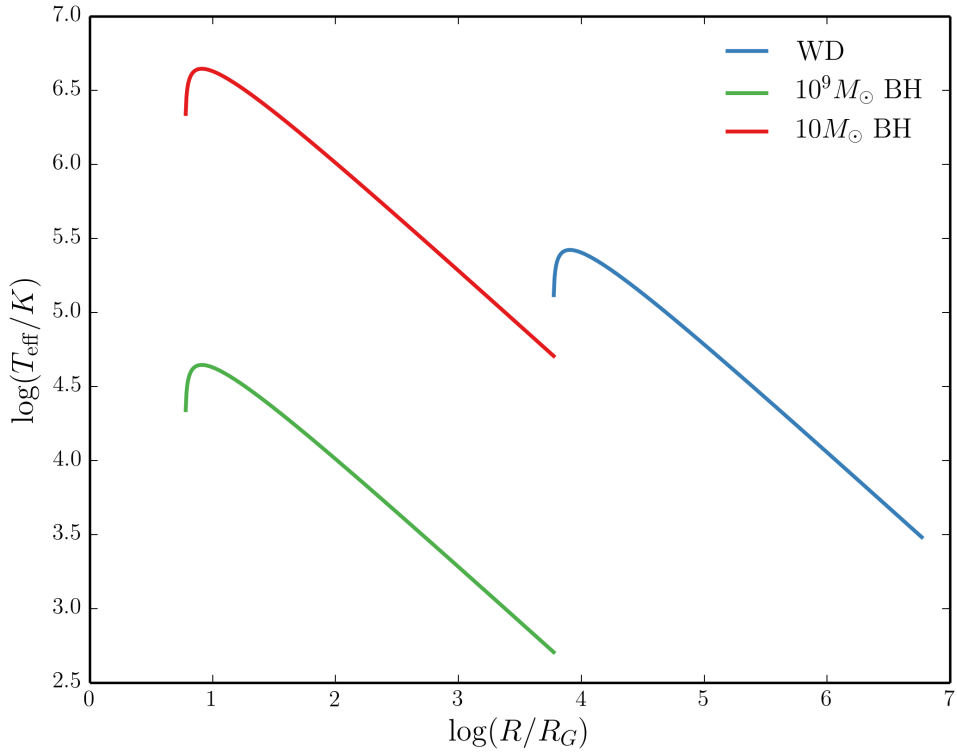


FIGURE 1.1: The temperature profile of an accretion disc for three different classes of compact object.

where $\Omega_K(R_*)$ is the Keplerian angular velocity at R_* , assuming the thickness of the BL is small. When $\Omega_K(R_*) \gg \Omega_*$, this reduces to $L_{BL} = 1/2 L_{acc} = L_{disc}$

In cataclysmic variables, BLs can be approximated with blackbodies and their temperatures estimated indirectly via the [Zanstra \(1929\)](#) method (e.g. [Hoare & Drew 1991, 1993](#)). However, they likely exhibit a variety of atomic features ([Suleimanov et al. 2014](#)). Extreme-UV (EUV) datasets have confirmed the existence of boundary layer emission in non-magnetic CVs ([Mauche 1996](#)), although these observations are limited in number.

Clearly, in BH systems a boundary layer cannot exist in the same way, due to the lack of a physical surface. Instead, the energy must either go into growing the BH, contributing to its angular momentum or being channeled into a jet or other radiative source (see section 1.5.2). The question of what happens at the inner disc edge is complicated further by the fact that the disc cannot extend to the event horizon of the BH. Instead, there is an ‘innermost stable circular orbit’ (ISCO) beyond which the accreting matter will simply fall into the BH along nearly radial paths. The radius of this orbit, R_{ISCO} , and the horizon radius, R_H , is shown for different values of the BH spin parameter, a_* , in

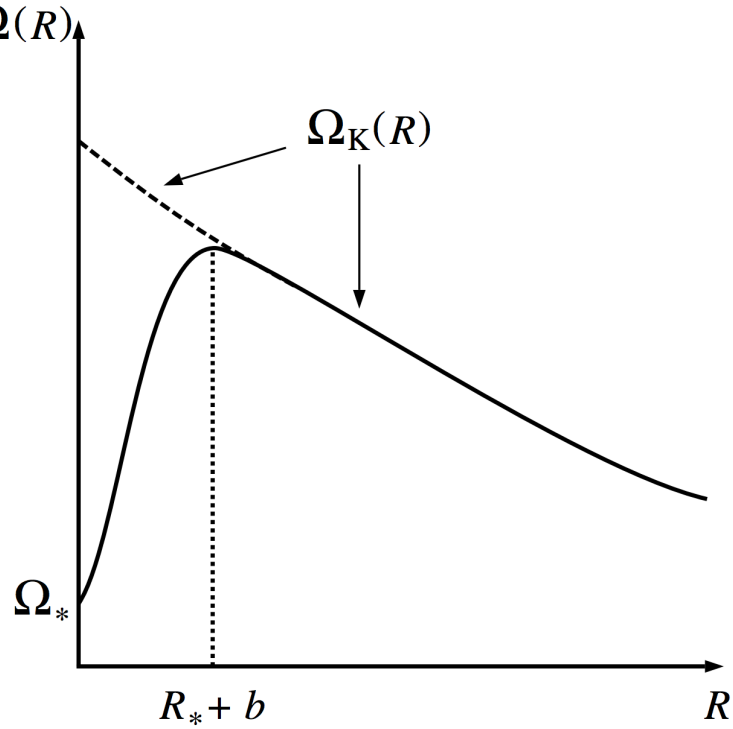


FIGURE 1.2: Credit: Frank et al. 2002. Angular velocity as a function of radius in an accretion disc around a rotating compact object with angular velocity Ω_* . Ω_K is the Keplerian angular velocity. This graph also helps explain why there is a turnover in the temperature-radius relation, as $D(R)$ is proportional to the square of the derivative of this quantity.

figure 1.3, showing how matter can orbit closer to a prograde spinning BH. In estimating the luminosity of a Keplerian disc around a BH, one should really set $R_* = R_{ISCO}$ in equation 1.5, giving us the interesting result that rapidly spinning (Kerr) BHs are more radiatively efficient than Schwarzschild BHs.

1.1.4 The emergent spectrum

It is important to recognise that the steady-state disc treatment *does not specify the exact shape of the disc SED*. What it does do is say where energy is originally released. The simplest assumption is that each annulus emits as a blackbody with temperature $T_{eff}(R)$, and the specific intensity through the emitting surface thus follows the Planck Law:

$$B_\nu(T) = \frac{2h\nu^3}{c^2} \frac{1}{\exp(h\nu/kT) - 1} \quad (1.21)$$

Under this assumption it is possible to show that at intermediate frequencies, where $kT(R_{max}) \ll h\nu \ll kT_*$, then the spectrum appears as a ‘stretched blackbody’ with the

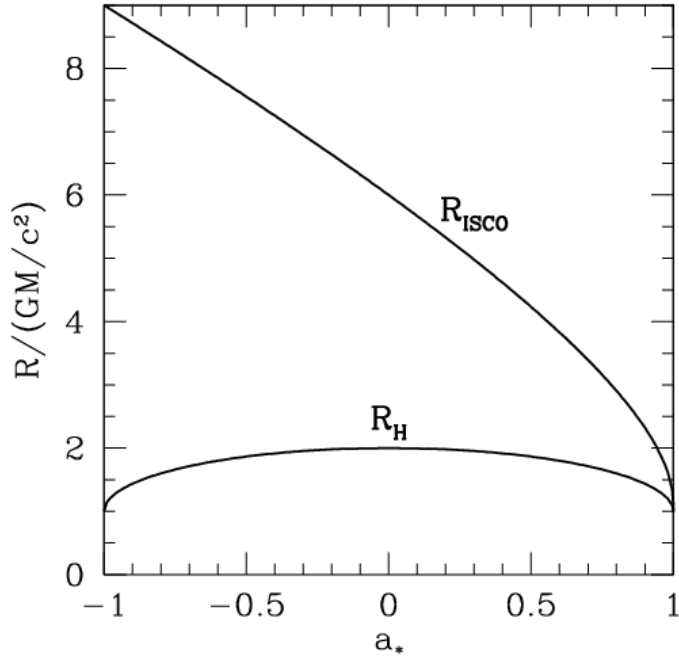


FIGURE 1.3: Credit: Narayan 2014. The radius of the ISCO, R_{ISCO} , and the horizon, R_H , is as a function of the BH spin parameter, a_* . $a_* = 0$ corresponds to a Schwarzschild BH, and $a_* = 1$ and $a_* = -1$ to prograde and retrograde Kerr BHs respectively. Note that this figure ignores the counteracting torque of photons swallowed by the BH, which actually limits a_* to a value of around 0.998 (Thorne 1974).

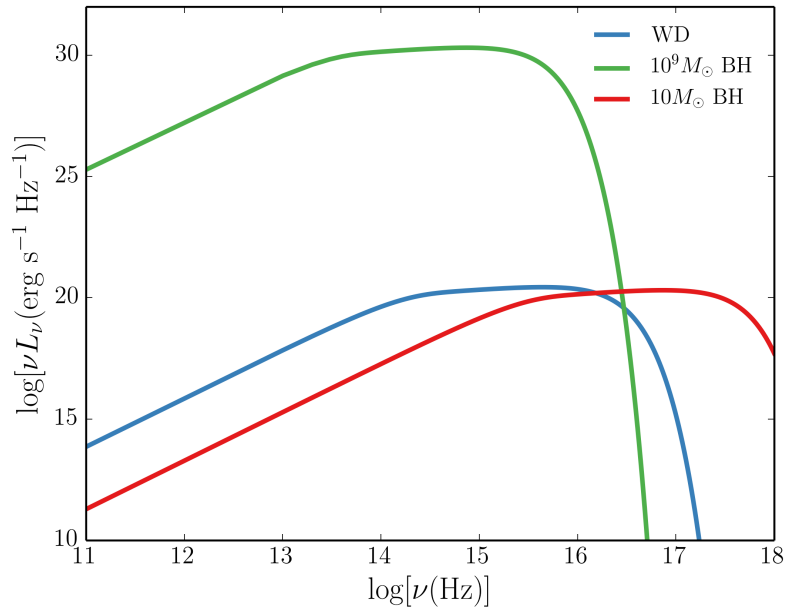


FIGURE 1.4: Accretion disc SEDs for three different compact objects, corresponding roughly to a quasar, an XRB and a CV. The SEDs are computed via an area-weighted sum of blackbodies with effective temperatures governed by equation 1.17, and the $\nu^{1/3}$ shape in the middle of the spectra can be seen.

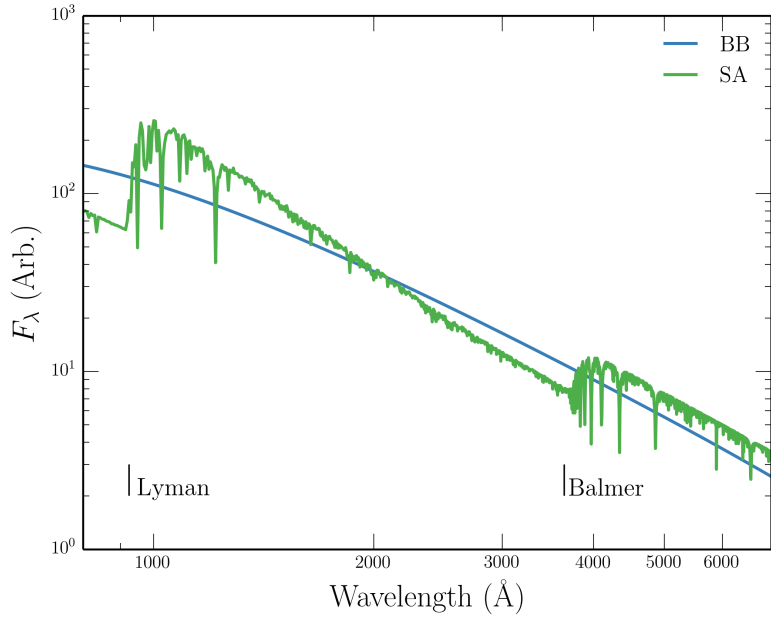


FIGURE 1.5: A comparison between a Planck curve and Kurucz (1991) stellar atmosphere model at $T_{eff} = 50,000\text{K}$ and surface gravity of $\log(g) = 5$. The major photoabsorption edges are marked. Flux is reprocessed into different wavelengths by bound-free opacities, and line blanketing also has a big effect on the spectrum. The Hydrogen and Helium lines also experience significant pressure broadening.

form

$$F_\nu \propto \nu^{1/3}. \quad (1.22)$$

Figure 1.4 shows the blackbody SEDs expected for the same objects as figure 1.1, in which the $\nu^{1/3}$ portion can be clearly seen. A disc atmosphere model with frequency-dependent opacity creates a somewhat different (and more realistic) spectrum. Figure 1.5 shows a comparison between a stellar atmosphere model and blackbody model for $T_{eff} = 50,000\text{K}$, showing how an annulus at that temperature can have a significantly different spectral shape when one includes frequency-dependent opacities in the atmosphere. It is of course possible that *neither* blackbody or disc atmosphere treatments are realistic. I shall therefore devote a little time to discussing the observational arguments for accretion discs and reviewing the different classes of accreting objects.

1.2 Accreting Compact Binaries

Accreting compact binaries form many different classes, but are all characterised by matter streaming from a donor onto a compact object. When the compact object is

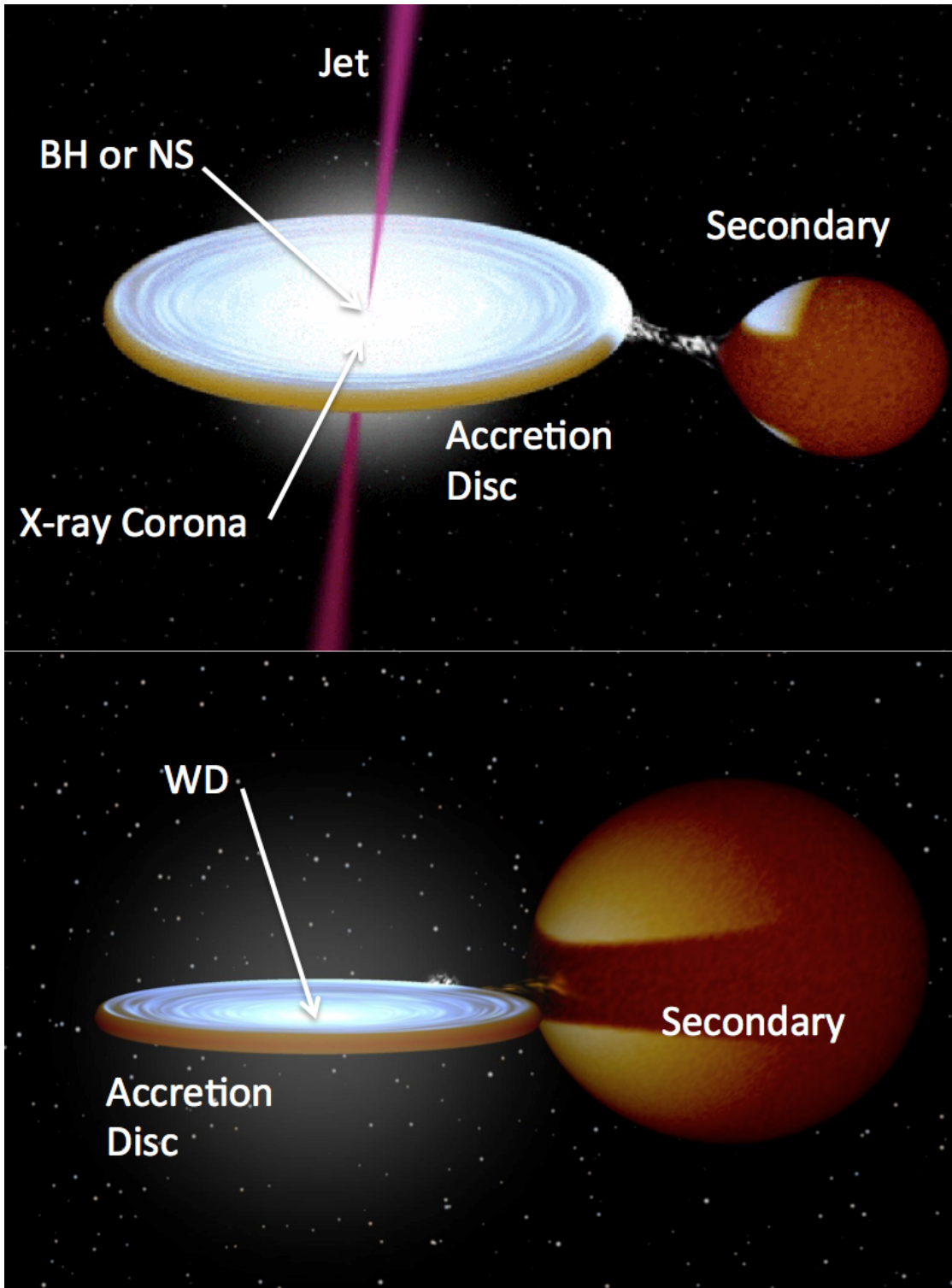


FIGURE 1.6: Credit: Rob Hynes. Artists impression of a low-mass X-ray binary (top) and cataclysmic variable (bottom). The key components are marked, and the clear similarity in overall structure is apparent.

more massive than the donor then it is designated as the ‘primary’, and the companion as the ‘secondary’. In high-mass X-ray binaries (HMXBs), the opposite is formally true. There are only two ways by which matter can transfer from the secondary to the compact object. One is by Roche Lobe-overflow (RLOF), whereby stellar evolution causes the donor star to fill its Roche Lobe, the surface of equipotential around the star. The alternative is that the donor may expel material via a disc or radiatively driven stellar wind, allowing some of it to flow onto the compact object. Although accretion from a wind or circumstellar disc is common in HMXBs ([Bartlett 2013](#)), here I will focus on RLOF as it is more common in the systems that possess high-state accretion discs and associated outflows. Two examples of these are shown in figure [1.6](#)

1.2.1 Roche Lobe-Overflow

Let us consider a binary system, with masses M_1 and M_2 , at positions \vec{r}_1 and \vec{r}_2 . The Roche potential, Φ_R , in this system is then

$$\Phi_R = -\frac{GM_1}{|\vec{r} - \vec{r}_1|} - \frac{GM_2}{|\vec{r} - \vec{r}_2|} - 1/2(\vec{\omega} \times \vec{r})^2, \quad (1.23)$$

where $\vec{\omega}$ is the angular velocity of the binary and is a vector normal to the orbital plane. This potential is plotted in figure [1.7](#) for a mass ratio, $q = M_2/M_1$ of 0.25.

In the context of semi-detached binary systems, the most important region of the potential is the dumbbell shaped region enclosing the masses. Each of these enclosed regions is known as the ‘Roche lobe’ of the object and can be expressed approximately in terms of the mass ratio and separation of the system. A good approximation for the size of the Roche lobe takes the form ([Eggleton 1983](#))

$$\frac{R_2}{a} = \frac{0.49q^{2/3}}{0.6q^{2/3} + \ln(1 + q^{1/3})}. \quad (1.24)$$

Here R_2 is the radius of a sphere with the same volume as the Roche lobe for the secondary star, which we can see depends only on q and the orbital separation, a . If this secondary expands enough to fill its Roche lobe, then matter will fall onto the other object. This process is known as Roche Lobe overflow (RLOF), and is vitally important in astrophysics. Although caused by stellar evolution, any accretion from RLOF will affect the mass ratio of the binary system and thus itself affects the evolution of binary

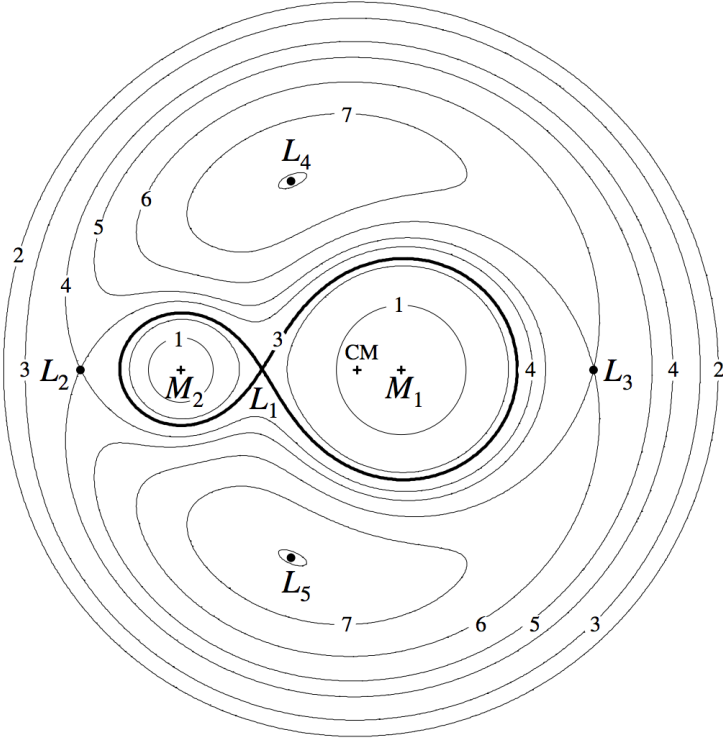


FIGURE 1.7: Credit: Frank et al. 2002. The Roche potential in a binary system for $q = M_2/M_1$ of 0.25. The Lagrangian points are marked, as are the locations of the individual and system centres of mass.

systems. This helps determine the orbital period distribution of binaries (e.g. Knigge et al. 2011) as well as affecting the delay time distribution of Type Ia Supernovae, for which CVs are one of the progenitor candidates (e.g. Wang & Han 2012). It is also worth noting that the existence of gravitational waves has been required in models to explain the orbital period evolution of CVs since the 1960s (Kraft et al. 1962).

1.2.2 Cataclysmic Variables

Cataclysmic variables (CVs) are systems in which a WD accretes matter from a donor star via Roche-lobe overflow (see the ‘CV bible’, Warner 2003). CVs are not always dominated by their accretion luminosity; classical novae and super soft sources (SSS) emit mostly due to nuclear burning or detonation on the WD surface. Accretion dominated CVs – the focus here – can be classified according to the magnetic field strength of the WD (B_{WD}) and photometric activity. Magnetic systems are classified as either ‘Polars’ ($B_{WD} \gtrsim 10^7$ G) or ‘Intermediate Polars’ ($10^6 \lesssim B_{WD} \gtrsim 10^7$ G); in these systems the accretion flow inside the some critical radius (related to the Alfvén radius)

is dominated by the WDs magnetic field (e.g. Patterson 1994). In polars, this radius is large enough, due to the strong magnetic field, that no disc forms at all (Liebert & Stockman 1985). When $B_{WD} \lesssim 10^6$ G then the accreting material can fall onto the WD via a disc, and the CV is classified as non-magnetic. There are two main types of non-magnetic CVs; dwarf novae and nova-like variables.

1.2.2.1 Dwarf Novae and the Disc-instability Model

Dwarf novae (DNe) are CVs that are characterised by repeated periods of quiescence and dramatic outburst. One of the most famous DNe is SS Cyg, whose light curve is shown in figure 1.8. The repeated outbursts can be clearly seen, and SS Cyg itself has been undergoing this behaviour for the full century for which it has been observed. A spectrum over the course of a typical outburst is shown in figure 1.9, and is characterised by the appearance of an optically thick accretion disc continuum – note the similarity to the stellar atmosphere disc spectrum computed in section 1.1.2.1, and to the intermediate inclination nova-like variables discussed in the next section.

The leading scenario for explaining DN outbursts, and in fact also the outbursts in low mass X-ray binaries or ‘soft X-ray transients’, is the disc-instability model (DIM; Osaki 1974; Lasota 2001). In this model, a gradual increase in supply rate from the donor star (and hence surface density in the disc) causes the disc to heat up. Eventually, the disc hits a critical temperature, around 7000 K, and becomes ionized. Now the surface density in the disc can increase significantly, and the disc becomes geometrically thin and optically thick. Most importantly, it can undergo efficient radiative cooling, and a significant increase in brightness is observed.

1.2.2.2 Nova-like Variables

Nova-like variables (NLs) are similar to DNe, except that the disc is always in a relatively high-accretion-rate state ($\dot{M} \sim 10^{-8} M_\odot \text{ yr}^{-1}$). NLs are therefore one of the best ‘laboratories’ for testing the steady-state accretion disc theory described in section 1.1.2.1. In the optical, NLs generally exhibit a series of H and He emission lines superposed on a blue continuum. In many cases, and particularly in the SW Sex subclass of NLs (Honeycutt et al. 1986; Dhillon & Rutten 1995), these lines are single-peaked. This is contrary

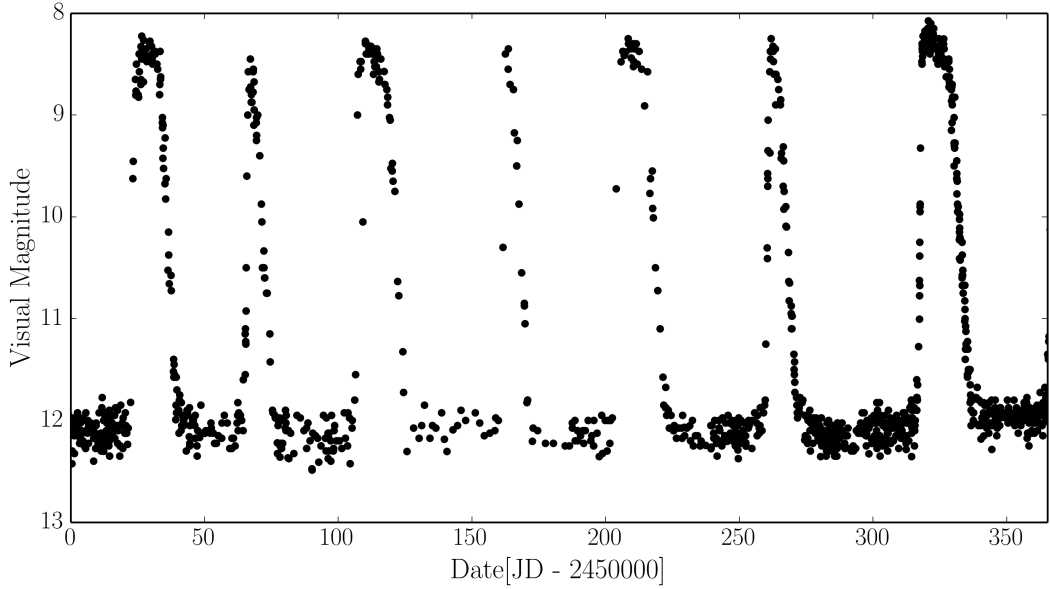


FIGURE 1.8: *Data: AAVSO.* A year in the life of SS Cyg, showing the characteristic repeated outbursts and periods of quiescence typical of a DN. SS Cyg has been undergoing this activity since it was first observed in 1896.

to theoretical expectations for lines formed in accretion discs, which are predicted to be double-peaked (Smak 1981; Horne & Marsh 1986). *Low-state* CVs (dwarf novae in quiescence) do, in fact, exhibit such double-peaked lines (Marsh & Horne 1990).

The UV spectra of NLs also show strong emission lines, and at low to intermediate inclinations dramatic blue-shifted absorption lines can be seen in some objects. The emission line equivalent widths in both the optical and the UV show clear correlations with inclination (Hessman et al. 1984; Echevarria 1988; Noebauer et al. 2010). This can be seen clearly in figure 1.11, and is connected to the correlation between line strength and absolute magnitude found by Patterson (1984); that is, the decrease in equivalent width at low inclination is caused by an *increase* in continuum flux. This is discussed further in chapters 4 and 6, but also has relevance to AGN and quasar unification schemes mentioned later in this introduction. The optical and UV spectra of NL CVs are discussed further in the context of winds in chapter 2.

1.2.3 Low Mass X-ray Binaries

Low-mass X-ray binaries (LMXBs) are similar to CVs in structure (see figure 1.6), but the compact object is either a neutron star (NS) or black hole (BH). The accretion disc emits in the soft X-ray regime, and an additional hard X-ray power law is also seen in

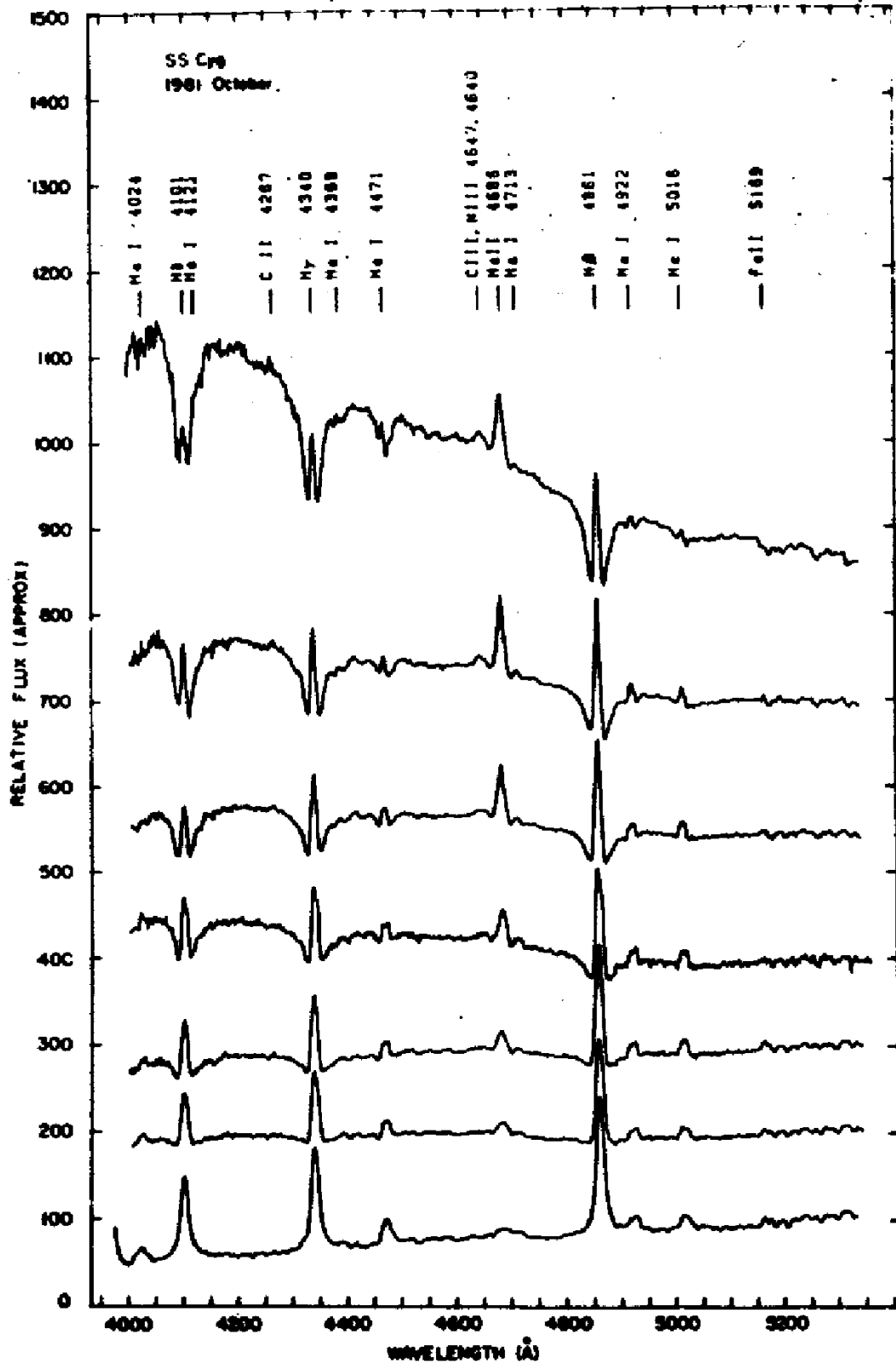


FIGURE 1.9: Credit: Hessman et al. 1984 / Dhillon et al. 1996. Spectra of SS Cyg during an outburst cycle, showing the evolution from minimum to maximum light. The rise is characterised by the appearance of an optically thick accretion disc spectrum. The flux scale is approximate.

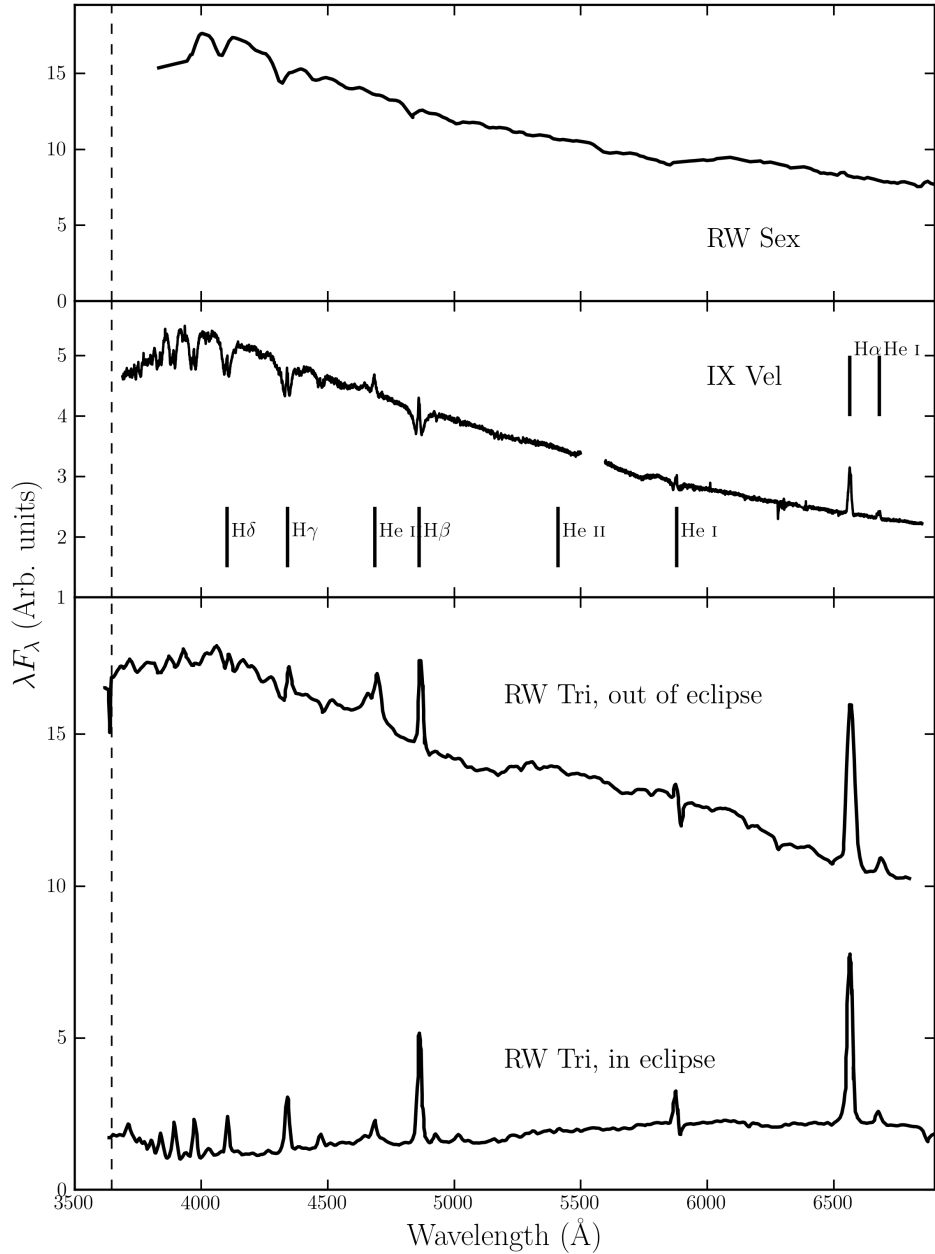


FIGURE 1.10: Optical spectra of three nova-like variables: RW Sex (top; Beuermann et al. 1992), IX Vel (top middle; A. F. Pala & B. T. Gaensicke, private communication) and RW Tri in and out of eclipse (bottom two panels; Groot et al. 2004). The data for RW Sex and RW Tri were digitized from the respective publications, and the IX Vel spectrum was obtained using the XSHOOTER spectrograph on the Very Large Telescope on 2014 October 10. These systems have approximate inclinations of 30° , 60° and 80° respectively. The trend of increasing Balmer line emission with inclination can be seen. In RW Tri strong single-peaked emission in the Balmer lines is seen even in eclipse, indicating that the lines may be formed in a spatially extensive disc wind, and there is even a suggestion of a (potentially wind-formed) recombination continuum in the eclipsed spectrum. I have attempted to show each spectrum over a similar dynamic range.

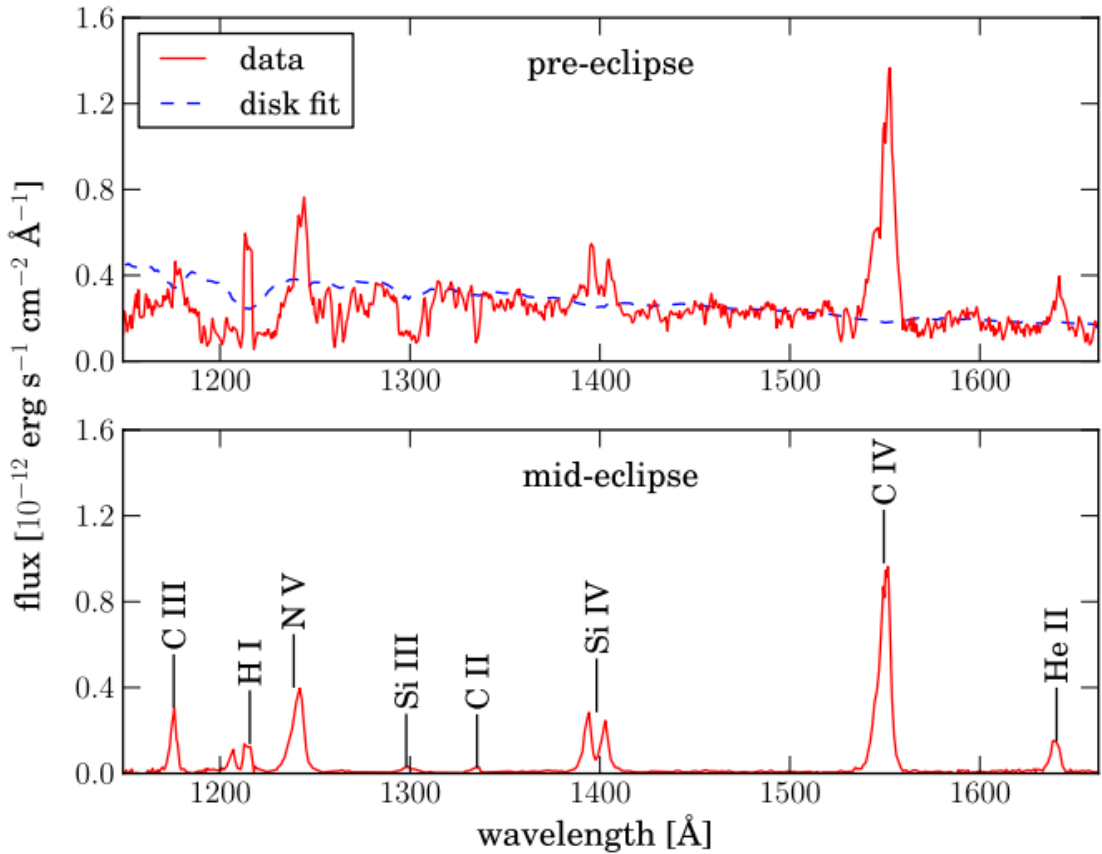


FIGURE 1.11: Credit: Noebauer et al. 2010. UV spectrum of RW Tri in and out of eclipse, showing strong lines in C IV λ 1550 and Ly α , among others.

the spectrum. This hard component is normally attributed to Compton up-scattering of seed disc photons by some kind of ‘corona’ of hot electrons close to the BH (e.g. White et al. 1988; Mitsuda et al. 1989; Uttley et al. 2014). Although I do not study LMXBs directly in this thesis, it is instructive to briefly discuss of their observational appearance as it is relevant to the links between accretion and outflow. The discovery that XRBs and CVs follow similar tracks on a hardness-intensity diagram (HID; Körding et al. 2008) is particularly interesting in this regard, especially since Ponti et al. (2012) showed that broad Fe absorption lines are only seen in the soft-state high-inclination systems (see section 2.1.2). This implies that equatorial outflows are intrinsic to the accretion process. Although the driving mechanism is probably different to CVs (e.g. Díaz Trigo & Boirin 2015), the similarity in general structure to models for CVs and quasars is striking.

1.3 Quasars and Active Galactic Nuclei

Spectra of AGN have now been studied for over 100 years, and we have known that they exhibit strong, broad emission lines since the first spectrum was taken by [Fath \(1909\)](#). However, it wasn't until the work of [Seyfert \(1943\)](#) that the systematic classification of AGN really began, leading to the phrase ‘Seyfert galaxy’. This label was applied to galaxies possessing a bright nucleus, spectroscopically characterised by a blue continuum and a series of strong emission lines. The first real physical insight into the extraordinary nature of AGN was provided by [Woltjer \(1959\)](#), who noted that (i) the nuclei must have sizes < 100 pc, based on the fact that they were unresolved, and (ii) the mass of the nucleus must be very high, based on virial estimates. While both of these observations were based on simple arguments, the fact that these ultra-luminous celestial objects are both *compact* and *supermassive* is perhaps the defining insight into the nature of AGN.

Although the study of AGN was established in the optical waveband, radio astronomy also significantly furthered our understanding of AGN in the mid-20th century. A number of surveys, such as the Cambridge ([Edge et al. 1959](#)), Parkes ([Ekers 1969](#)) and Ohio ([Ehman et al. 1970](#)) surveys discovered a great many bright radio point sources distributed isotropically across the sky. These sources eventually became known as ‘quasi-stellar radio sources’, or *quasars*, and were soon found to be coincident with bright optical sources or ‘quasi-stellar objects’ (QSOs) at high redshifts ([Schmidt 1963, 1965a,b](#)). Nowadays, the term quasar normally has very little to do with radio emission and is often used interchangeably with QSO. Indeed, throughout this thesis I shall refer to a quasar as simply a bright, massive AGN; one with sufficiently high luminosity that it dominates the emission from its host galaxy.

One of the main classification schemes for AGN is a spectroscopic one, based on whether an object possesses broad emission lines in its spectrum, such as C IV broad H β and Ly α , in addition to the narrow lines that are always present. If these broad lines are seen, then the AGN is classed as type I; if not, it is classed as type II (figure 1.12). These designations were originally applied to Seyfert galaxies ([Seyfert 1943](#)), but can also be used to classify the more luminous quasar class, despite the apparent difficulty in finding the expected number of type II sources ([Zakamska et al. 2003](#)). This classification scheme is complicated somewhat by the existence of two unusual types of AGN: narrow line Seyfert Is (NLSIs), which may be explained by super-Eddington accretion ([Done](#)

& Jin 2015) or perhaps simply an orientation effect (Baldi et al. 2016), and so-called ‘true type II’ AGN, in which the broad line region is absent (Tran 2001; Shi et al. 2010) rather than obscured (see next section). Despite this muddying of the waters, what was originally a clear dichotomy in spectral type provided a profound motivation for attempting to *unify* AGN via geometric arguments.

1.3.1 AGN Unification and the dusty Torus

Although Seyfert had identified type 1 and 2 AGN, a physical explanation for this dichotomy was not forthcoming until a study by Antonucci & Miller (1985, AM85). They showed unambiguously that the nearby Seyfert 2 NGC 1068 is simply an obscured type 1 AGN, by finding that broad emission lines appeared in the spectrum of *polarised* flux. This provided the basis for the first successful attempt to unify AGN behaviour, as it elegantly explained the apparent disconnect between the two types of AGN as simply a viewing angle effect; at one angle, an observer could look directly into the broad line region (BLR) near the nucleus, but at Type 2 angles this region was hidden from view. The obscuring structure became known as the ‘torus’ (Krolik & Begelman 1986), due to its proposed geometry, and it was soon realised that this structure may be made of dust, in which case it could also be responsible for the infra-red (IR) bump in AGN (Neugebauer et al. 1979).

Urry & Padovani (1995, UP95) went further than the original unification model proposed by AM85, as they also tried to account for the dichotomy in AGN radio properties (radio-loud/radio-quiet). The picture they proposed is shown in figure 1.13. This model attempts to explain all of the types of AGN merely as a function of viewing angle and presence, or absence, of a radio jet. Models such as this also describe the series of ‘bumps’ observed in AGN – the portions of the spectrum that dominate the luminosity, shown in figure 1.14. In most models, the ‘Big Blue Bump (BBB)’ is ascribed to thermal emission from an accretion disc, and the ‘Small Blue Bump’ to optically thin Balmer continuum and Fe II emission from the BLR. The latter can just be seen between $\sim 2000\text{\AA}$ and $\sim 4000\text{\AA}$ in the Seyfert 1 and quasar templates in figure 1.12. Our understanding of the BBB is still unsatisfactory (see section 1.4).

Since the seminal works by AM85 and UP95, the picture has become somewhat more complicated. Variable X-ray absorption has been detected in so-called ‘changing look’

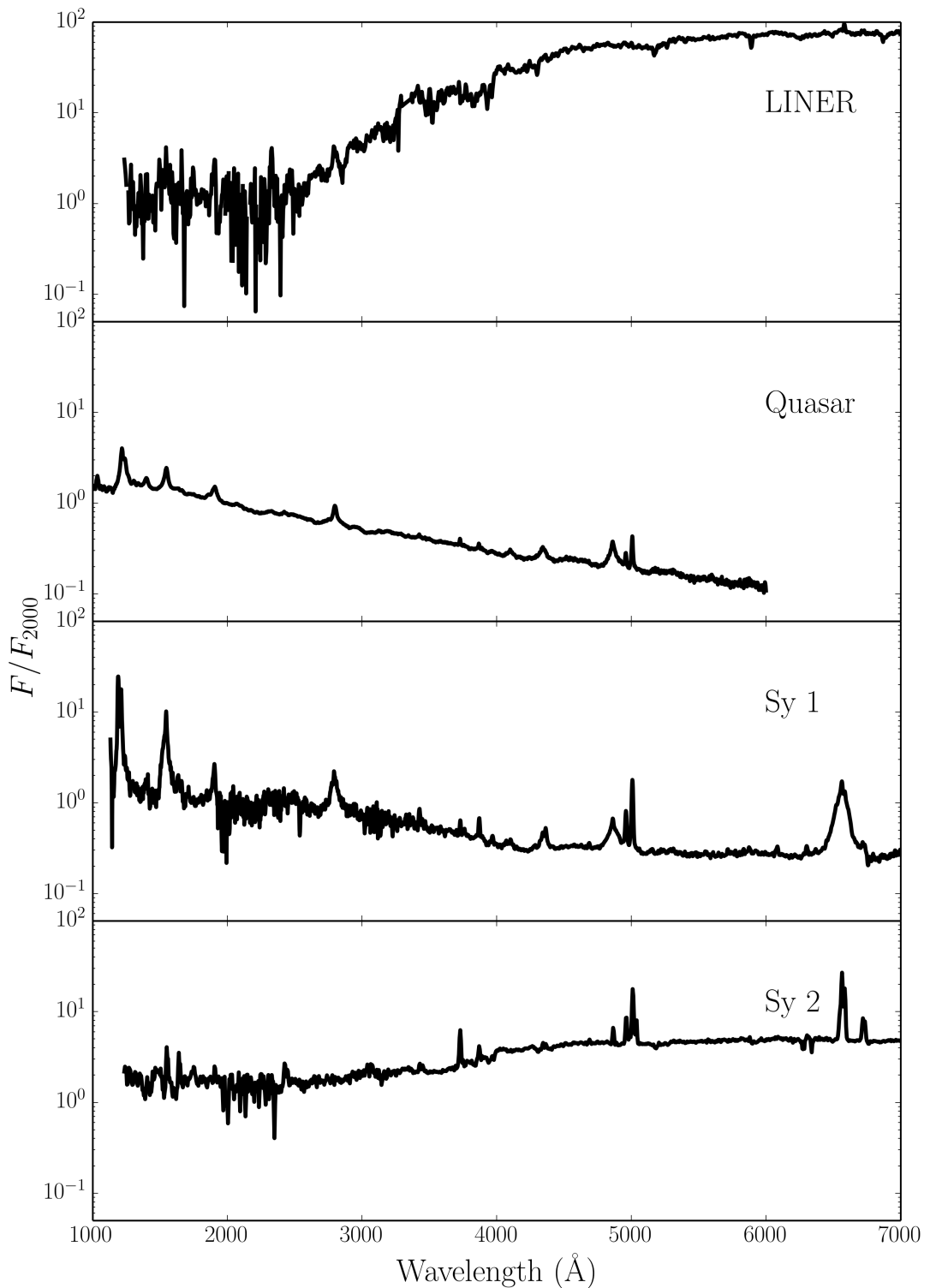


FIGURE 1.12: Template spectra, from the AGN atlas, for four common types of AGN.
Obtained from http://www.stsci.edu/hst/observatory/crds/cdbs_agn.html.

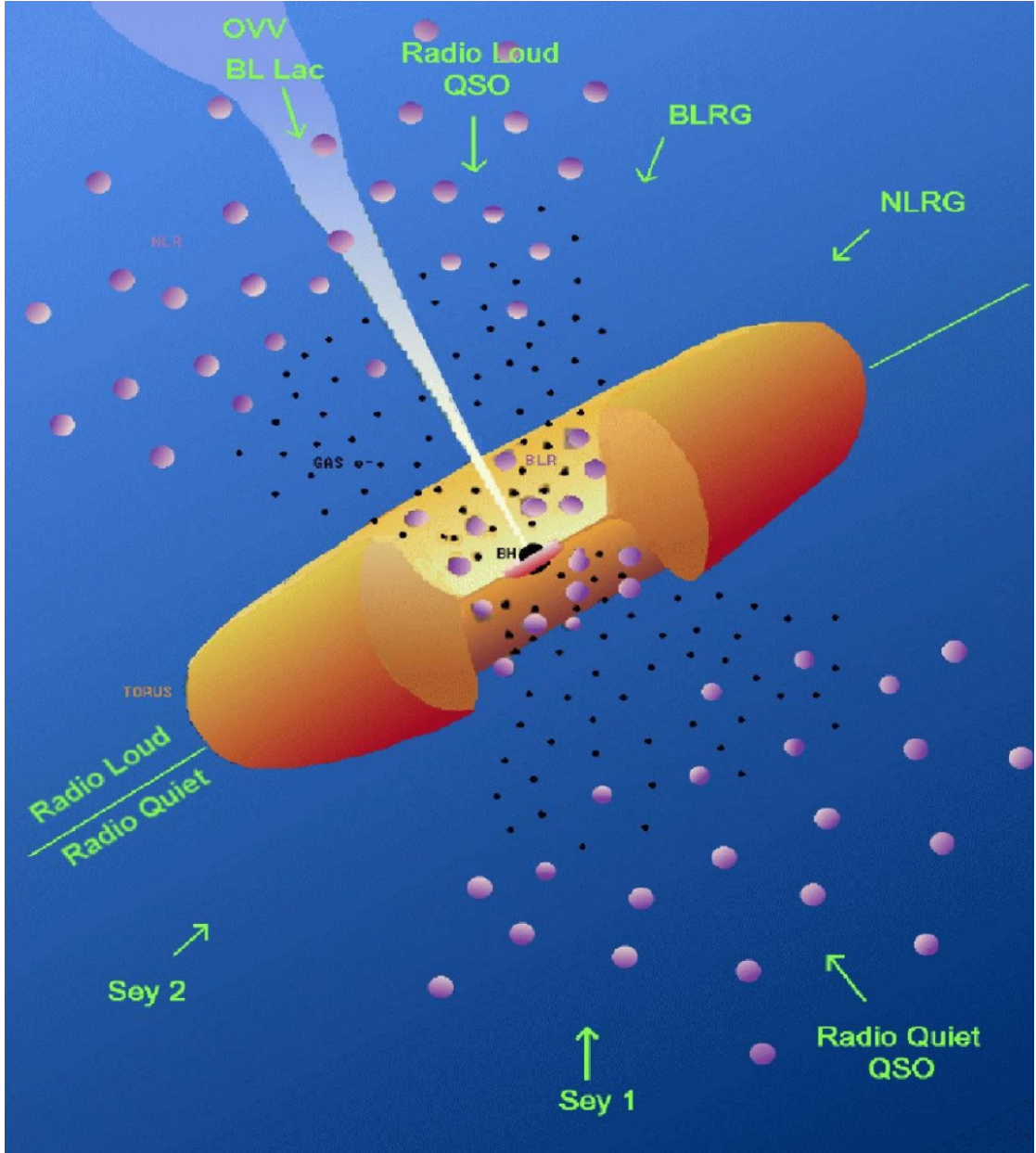


FIGURE 1.13: A unified scheme for AGN.

AGN (Matt et al. 2003; Puccetti et al. 2007), including even NGC 1068 itself (Marinucci et al. 2016). Changes in type have also been seen in the optical lines; the broad H β component in some AGN can dramatically disappear or reappear (e.g. Tohline & Osterbrock 1976; Cohen et al. 1986; Denney et al. 2014). The explanation for this could be variable absorption (Elitzur 2012) or a change in the accretion state of the disc. In the latter case, it has even been suggested that a disc wind could be directly responsible for this switch (Elitzur et al. 2014). Furthermore, dusty *polar* outflows have been found to be important IR emitters (Hönig et al. 2013), implying that, even when it comes to dust, the torus is not the whole picture. Despite these complications, the AGN torus

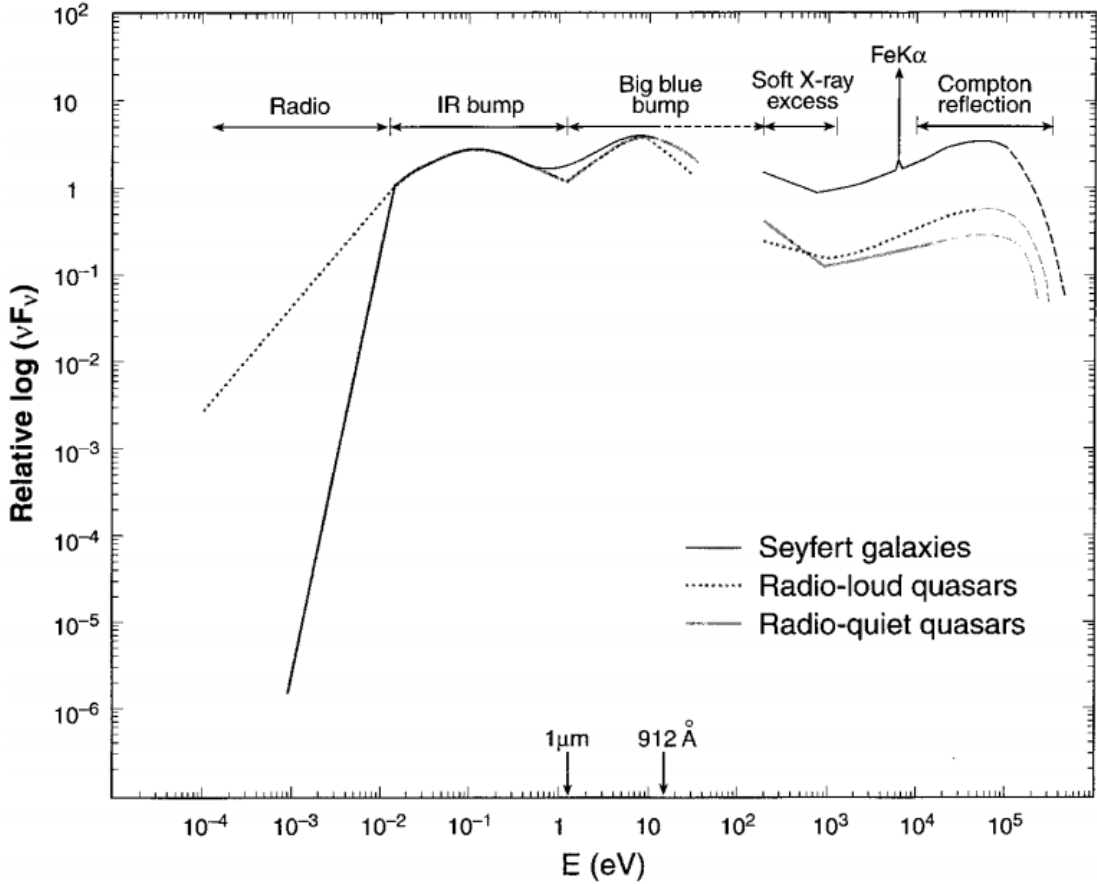


FIGURE 1.14: Credit: Koratkar & Blaes 1999 Approximate average broadband SEDs for a few types of AGN. The series of characteristic bumps can be clearly seen. The Soft-X-ray excess is also visible (see section 1.3.2.1).

unification picture still explains a lot of AGN phenomenology, and represents a useful framework that can be tested with observations.

1.3.2 X-ray Properties of AGN

Approximately 10% of the bolometric luminosity of AGN comes out in the X-ray band, between ~ 0.1 and ~ 100 keV. Thus, AGN dominate the cosmic X-ray background (Madau et al. 1994). The hard X-ray emission typically follows a power law shape with spectral index -0.9 (e.g. Koratkar & Blaes 1999), widely considered, as in LMXBs, to come from a hot ‘corona’ of electrons close to the BH that upscatters disc seed photons (e.g. Haardt & Maraschi 1991). The compactness of this X-ray corona has been confirmed by microlensing (Chartas et al. 2009; Dai et al. 2010) and variability studies (Green et al. 1993; Crenshaw et al. 1996; Risaliti et al. 2007; Emmanoulopoulos et al. 2014). Indeed, X-rays in AGN can be highly variable, both in terms of their intrinsic

X-ray emission, but also due to changes in the absorption characteristics (Risaliti et al. 2002; Miller et al. 2008; Connolly et al. 2014). I discuss X-ray absorption in more detail, particularly with respect to disc winds, in chapter 2.

The hard X-ray spectra AGN also tend to exhibit a number of reflection features. Typically, these consist of a strong Fe K α emission line and a ‘Compton hump’ at high energies. The latter is produced by Compton down-scattering of high energy photons (Pounds et al. 1989; Nandra & Pounds 1994). It is still unclear exactly where these features originate, but a common interpretation is that they are caused by reflection off the inner parts of the accretion disc (Fabian et al. 1995; Iwasawa et al. 1996a; Reynolds 1999). If this is the case, and the broadening of the iron line is relativistic, this would allow for measurements of the BH spin (Laor 1991; Iwasawa et al. 1996b; Dabrowski et al. 1997). This hypothesis is somewhat controversial. Multiple authors have found that many of the relativistic features supposedly imprinted by BH spin can in fact be explained by Comptonisation or absorption (e.g. Misra & Kembhavi 1998; Miller & Turner 2013), and radiative transfer modelling has shown that an outflow can naturally produce the characteristic broad red Fe K α wing (Sim et al. 2010a).

In Compton-thick AGN, the intrinsic continuum is heavily absorbed with columns of $N_H \sim 10^{24}$ cm $^{-2}$ – this absorption is normally attributed to the dusty torus, but disc winds could also contribute. Compton-thick AGN are required in large numbers in order to explain the cosmic X-ray background (Setti & Woltjer 1989). In these sources, reflection features can actually dominate the X-ray spectrum (Alexander et al. 2011; Gandhi et al. 2013), but the Fe line is formed from low ionization stages of Fe on ~ 0.1 pc scales (Gandhi et al. 2015).

1.3.2.1 The Soft X-ray Excess

If one interpolates between the $\nu^{1/3}$ law from the BBB in the UV, and the power law in the hard X-rays, a curious excess of flux is often found in type 1 AGN (see figure 1.14, and Koratkar & Blaes 1999). This is known as the soft X-ray excess (SXES), which is too hot to be explained by thermal disc emission, as a thin disc around an AGN should never approach the temperatures required. Many models have been proposed to explain this excess, including relativistically smeared photoabsorption (Gierliński & Done 2004, 2006), relativistically smeared line and free-free emission (Ross & Fabian 2005; Crummy

(et al. 2006) and a variety of cool Comptonised component geometries such as an inner accretion flow (Magdziarz et al. 1998; Done et al. 2012) and thin layer on top of the disc (Janiuk et al. 2001). While the SXSS poses a challenge to the simplest pictures of AGN, it may also solve some of the issues, as some of the geometries proposed may help to explain the accretion disc size problem discussed in section 1.4 (Gardner & Done 2016).

1.3.3 The Broad Line Region: Connection to winds and unification

In the UP95 unification model, the broad emission lines come from a series of virialised clouds close to the disc plane. As noted by Murray et al. (1995, hereafter MCGV95), there are a number of problems with the BLR ‘cloud’ model, perhaps most notably that there is no obvious physical origin for such virialised clouds. Testing alternative models for the BLR is therefore important. Indeed, MCGV95 proposed a disc wind model in order to explain both BALs and BELs in quasars. A disc wind model was also discussed by Elvis (2000), who proposed a structure for quasars that attempted to explain much of the behaviour of luminous AGN merely as a function of viewing angle. It is worth noting that there is observational support for the unification paradigm; for example, it has been suggested that orientation is a key driver of the so-called ‘Eigenvector 1’ relationship in quasars (Boroson & Green 1992; Sulentic et al. 2000; Marziani et al. 2001; Shen & Ho 2014). Disc wind unification models are discussed further in section 2. The philosophy of these models is that, before invoking additional degrees of freedom in a model, we should first test if known quasar phenomenology (disc winds) can explain other aspects of their observational appearance. I have illustrated this general principle with the ‘Occam’s quasar’ cartoon shown in figure 1.15. This is the picture that I will quantitatively test in the latter, quasar-focused sections of this thesis. The same general principle can also be applied to cataclysmic variables and other accreting objects.

1.4 The Current Understanding of the Disc Continuum

The SS73 model is still the most common way to fit accretion disc spectra and infer information about the underlying physics. However, a number of issues have been raised with the thin-disc model and its applicability to accreting systems.

OCCAM'S QUASAR: THE PRINCIPLE THAT IN EXPLAINING A QUASAR NO MORE ASSUMPTIONS SHOULD BE MADE THAN ARE NECESSARY.

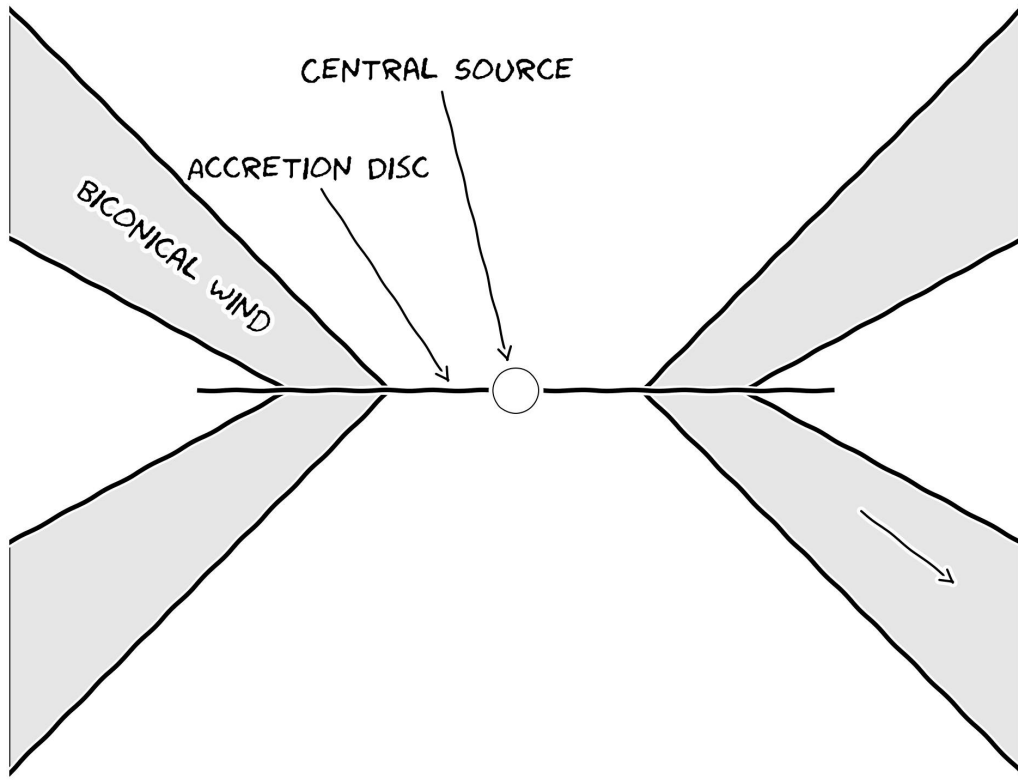


FIGURE 1.15: Occam's quasar. How far can this general picture take us when trying to explain the behaviour of quasars and other accreting compact objects?

1.4.1 The Spectral shape of CV discs

Attempts to fit the observed SEDs of high-state CVs with simple disc models have met with mixed success. In particular, the SEDs predicted by most stellar/disc atmosphere models are too blue in the UV (Wade 1988; Long et al. 1991, 1994; Knigge et al. 1998a) and exhibit stronger-than-observed Balmer jumps in absorption (Wade 1984; Haug 1987; La Dous 1989; Knigge et al. 1998a). One possible explanation for these problems is that these models fail to capture all of the relevant physics. Indeed, it has been argued that a self-consistent treatment can produce better agreement with observational data (e.g. Shaviv et al. 1991; but see also Idan et al. 2010). However, an alternative explanation, suggested by Knigge et al. (1998b; see also Hassall et al. 1985), is that recombination continuum emission from the base of the disc wind might fill in the disc's Balmer absorption edge and flatten the UV spectrum.

Alternatively, it may just be that CV disks are never really in a steady state, and so we should only expect the $R^{-3/4}$ temperature profile to hold in a limited portion of the disc. From eclipse mapping, it has been shown that the inferred accretion rate increases with radius in NLs (Rutten et al. 1992; Horne 1993). These results suggest that a non-radiative form of energy loss is present in the inner regions of the disc, of which potential forms would be advection or mass loss. This is yet another piece of evidence that the understanding of accretion and outflow are intertwined, although hopefully not inextricably.

1.4.2 The Big Blue Bump in AGN

Does the SS73 model apply well to AGN spectra? There are contrasting views on the matter. On the one hand, Antonucci (2013) claims that “most of the AGN community is mesmerized by unphysical models that have no predictive power”. Yet a recent spectral fitting study by Capellupo et al. (2015) concludes that “altogether, these results indicate that thin ADs are indeed the main power houses of AGN”. So, what are the current problems when confronting thin disc models with observation?

1.4.2.1 The Accretion Disc Size Problem

One of the most interesting results of recent years relating to AGN and accretion discs is the discovery that the continuum emission region size appears to be a factor ~ 3 larger than predicted by standard thin disc theory. This result has been found independently in both microlensing (Morgan et al. 2010; Dai et al. 2010) and reverberation (Edelson et al. 2015) studies, and poses a challenge to the current best-fit model for the big blue bump in AGN. One proposed solution is that the discs in AGN are inhomogeneous, consisting of individual clumps with independently varying temperatures (Dexter & Agol 2011), but this is very much still an active area of research. It is worth noting that the impact of winds on these results has not yet been properly quantified, something our team is currently trying to address (Mangham et al. 2016).

1.4.2.2 Fitting AGN Spectra and the 1000Å Break

One of the *successes* of the thin disc model, when applied to AGN, is that we do observe a slope in the UV of $\alpha_{UV} = 0.32$, confirming the theoretical prediction of $\nu^{1/3}$. However, AGN spectra do not exhibit the *overall* spectral shape (e.g. [Davis et al. 2007](#); [Shankar et al. 2016](#)) or colour-mass scalings ([Bonning et al. 2007](#)) expected from theoretical predictions. This can be seen clearly in figure 1.12, where both the quasar and Seyfert spectra tend to peak in the UV, rather than the EUV. Furthermore, there is a characteristic break in AGN spectra at around 1000 Å ([Lusso et al. 2015](#)), which does not scale with BH mass or luminosity, as one might expect for a break associated with an accretion disc. There is also no evidence in AGN of the expected polarisation signatures from an optically thick disc atmosphere ([Stockman et al. 1979](#); [Antonucci 1988](#); [Antonucci et al. 1996](#)).

Despite these problems, recent work suggests that the thin disc model still has some potential. [Capellupo et al. \(2015\)](#) were able to fit a number of AGN spectra in the UV and optical with thin disc models, although successful fits were only found once they included effects such as Comptonisation and mass-loss, as well as correcting for extinction. BH spin also had a reasonable effect on the spectral fits, although it is somewhat difficult to constrain from spectral fitting alone. The 1000 Å break has also been explained with a mass-losing disc ([Laor & Davis 2014](#)), and [Lusso et al. \(2015\)](#) suggested that incorrect IGM corrections may be exacerbating the effect. So, while many problems exist, it may not quite be time to abandon the Shakura-Sunyaev ship just yet.

1.5 The Universality of Accretion

Accretion appears to be an important physical processes across ~ 10 orders of magnitude in mass. But is this process the same on all scales? Does any behaviour manifest in all accreting systems?

1.5.1 The RMS-flux relation

Broad-band variability is common in all types of accretion disc. It has been known for some time that there exists a linear relationship between the flux and absolute root-mean-square (rms) amplitude of this variability. This was discovered first in XRBs and AGN (Uttley & McHardy 2001; Uttley et al. 2005; Heil et al. 2012), but it has been shown more recently that the relationship extends to CVs and even YSOs (Scaringi et al. 2012, 2015). The relationship is also not limited to just one type of CV but is present in both NLs and DNe (Van de Sande et al. 2015).

The model that best reproduces this behaviour is the so-called ‘fluctuating accretion disc’ model (Lyubarskii 1997; Kotov et al. 2001; Arévalo & Uttley 2006; Hogg & Reynolds 2015). More generally, additive processes cannot reproduce this behaviour, and a multiplicative mechanism is required (Uttley et al. 2005). Regardless of the mechanism, the rms-flux relation is one of the most clear-cut examples of a universal accretion phenomenon. It tells us that at least some of the behaviour in CV discs is also present in AGN and XRBs, strengthening the argument that CVs can be used as ‘accretion laboratories’.

1.5.2 Accretion states and disc-jet coupling

Variable and transient sources are common in astrophysics, particularly when the sources are accreting. I have already mentioned the DIM and its applicability to LMXBs and CVs; it turns out that when one plots the colour and luminosity evolution over the course of an outburst cycle then they follow very similar tracks (see figure 1.16, Körding et al. 2008). The detection of radio jets is also intrinsically linked to the accretion state of the system (disc-jet coupling), as jets only appear in the ‘hard’ accretion state, to the right of the so-called ‘jet line’ (Fender 2001; Fender et al. 2004). Körding et al. (2008) showed that this behaviour also occurs in CVs, as radio emission in the DN SS Cyg is also detected in the same region of colour-luminosity space. There is also a well-known correlation between radio and X-ray luminosities in low-hard states (Gallo et al. 2003).

Clear correlations between disc state and radio loudness have also been found in AGN. Perhaps the most obvious piece of evidence that disc-jet coupling is scale invariant is the so-called ‘fundamental plane of BH activity’ (Merloni et al. 2003), which extends

from LMXBs right up to quasars. AGN have also been shown to occupy similar regions of colour-luminosity space to the LMXBs (Körding et al. 2006), and simulations involving scaled-up LMXB discs have been successful in reproducing AGN accretion states (Sobolewska et al. 2011). Correlations in X-ray photon index are also found in present AGN and LMXBs; ‘softer when brighter’ behaviour is found at relatively high Eddington ratios (McHardy et al. 1999; Gu & Cao 2009), while ‘harder when brighter’ is observed in low states (Gu & Cao 2009; Emmanoulopoulos et al. 2012; Connolly et al. 2016).

Despite this apparently universal behaviour, the jet production mechanism in BHs is not well known. Theoretical work suggests that radio jets should be correlated with BH spin (Penrose & Floyd 1971; Blandford & Znajek 1977), but whether such a correlation exists in LMXBs is controversial (Fender et al. 2010; Narayan & McClintock 2012). This has significant implications for AGN; if powerful radio jets are associated exclusively with rotating BHs then the number of radio-loud AGN would imply a large fraction of them must be rapidly spinning, with high radiative efficiencies. Further evidence that radio jets are not simply produced by RIAFs onto spinning BHs is found when one considers that NLs show evidence of synchrotron radio emission (Coppejans et al. 2015). This important result suggests that our understanding of jets is incomplete, and that the links between accretion state and jet production are fundamental, but unsolved. Disc winds may complicate, or simplify, matters, depending on one’s outlook (see chapter 2).

1.5.3 A Global Picture

Clearly, accretion physics is relevant to a plethora of astrophysical phenomena, and at least some of the physics of accretion is applicable to *all* classes of accreting object. It would also appear that the outflowing material observed in accreting systems has a profound effect on the accretion process itself, and possibly significantly affects the observational appearance of disc-accreting systems (c.f. Elvis unification model). Hence, in the next chapter, I will review the evidence for winds and discuss some of the relevant background theory.

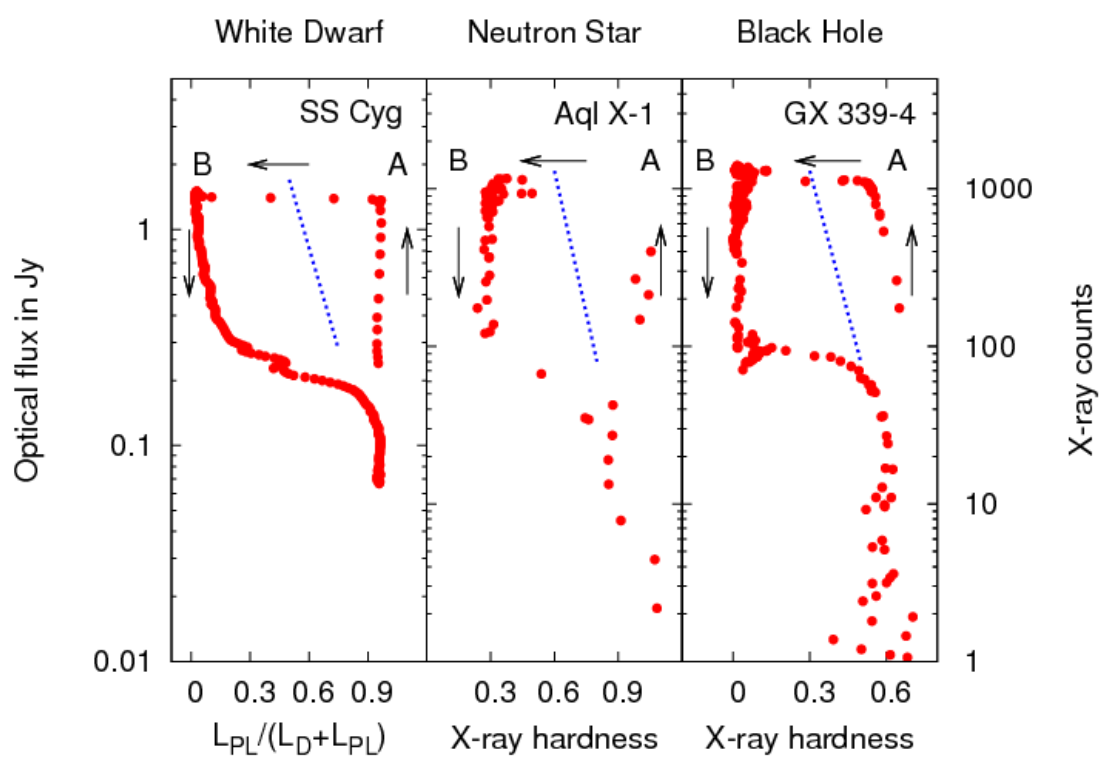


FIGURE 1.16: Credit: Kording et al. 2008. Caption.

Chapter 2

Accretion Disc Winds

“A view of space, with an elephant
obstructing it”

Mike Vennart, Silent/Transparent

2.1 Observational Evidence

Observational evidence for mass-loaded outflows or winds is widespread across the entire astrophysical mass range and most of the electromagnetic spectrum. Before exploring this evidence, it is pertinent to briefly discuss the ‘smoking gun’ used to unambiguously detect winds – the presence of blue-shifted BALs or ‘P-Cygni’ profiles in an object’s spectrum.

Fig. 2.1 shows how a spherical outflow presenting significant line opacity will cause these characteristic profile shapes to form, as scattering out of the line of sight causes a dip in the blue wing of the line, while scattering into the line of sight from other portions of the outflow causes an increase in flux in the red wing of the line. The situation is much more complex in most astrophysical situations; for example, the geometry is rarely spherically symmetric, and the line is rarely a pure scattering case. Indeed, the potential for complicated radiative transfer effects and the variety in line formation mechanisms (e.g. recombination, collisionally excitation) is one of the reasons why 3D Monte Carlo radiative transfer simulations are necessary to effectively model disc winds (see chapter 3).

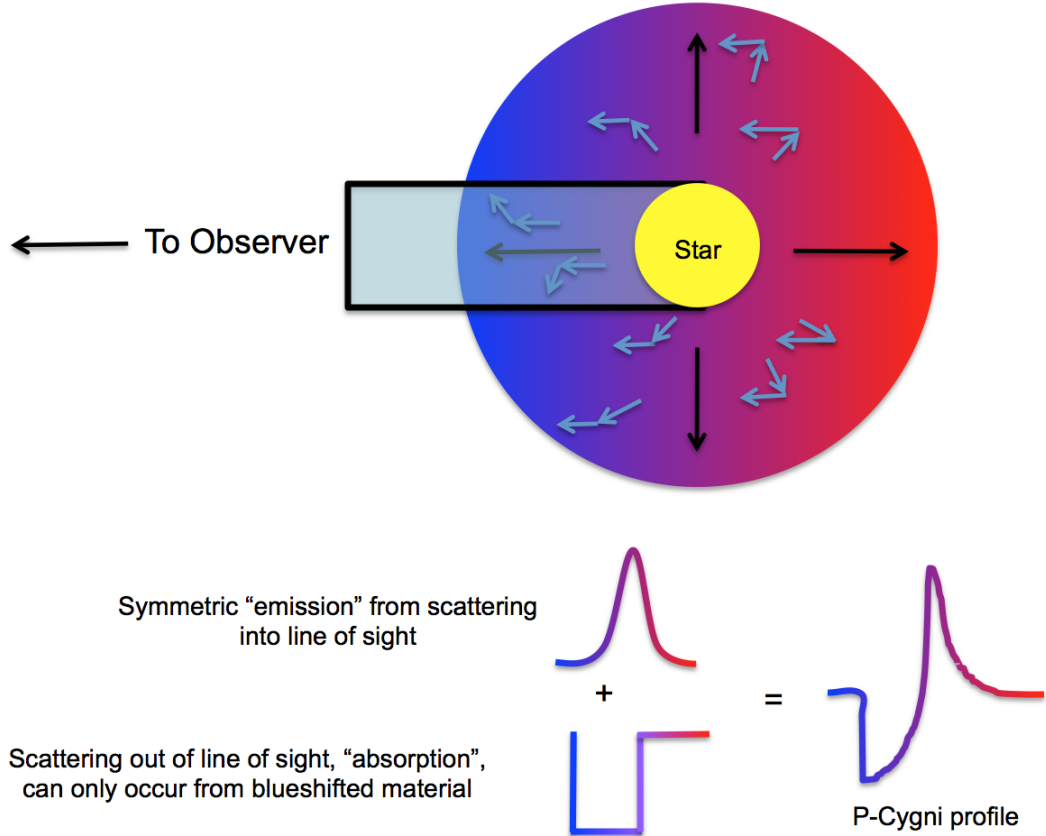


FIGURE 2.1: Diagram showing how an expanding envelope or wind with significant line opacity around a continuum source leads to the formation of P-Cygni profiles. The black arrows denote the outflow direction and the blue arrows typical scattering interactions.

2.1.1 Cataclysmic Variables

It has been known for a long time that winds emanating from accretion discs are important in shaping the ultraviolet (UV) spectra of high-state CVs (Heap et al. 1978; Greenstein & Oke 1982). The most spectacular evidence for such outflows are the P-Cygni-like profiles seen in UV resonance lines such as C IV $\lambda 1550$ (e.g. Cordova & Mason 1982, see Fig. 2.2). Considerable effort has been spent over the years on understanding and modelling these UV features (e.g. Drew & Verbunt 1985; Mauche & Raymond 1987; Shlosman & Vitello 1993; Knigge et al. 1995; Knigge & Drew 1997; Knigge et al. 1997; Long & Knigge 2002; Noebauer et al. 2010; Puebla et al. 2011). The basic picture emerging from these efforts is of a slowly accelerating, moderately collimated bipolar outflow that carries away $\simeq 1\% - 10\%$ of the accreting material. State-of-the-art simulations of line formation in this type of disc wind can produce UV line profiles that are remarkably similar to observations, as shown in Fig. 2.3.

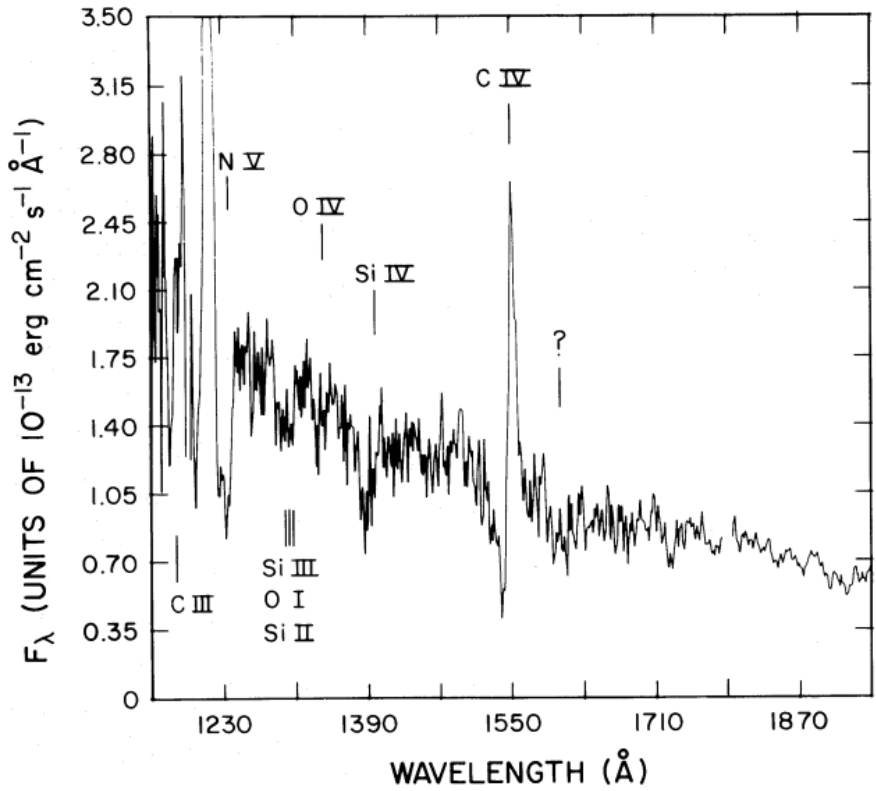


FIGURE 2.2: Credit: Cordova & Mason 1982. UV spectrum of the DN TW Vir during outburst. The P-Cygni profiles can be seen clearly, demonstrating that a strong, fast outflow is present in the system.

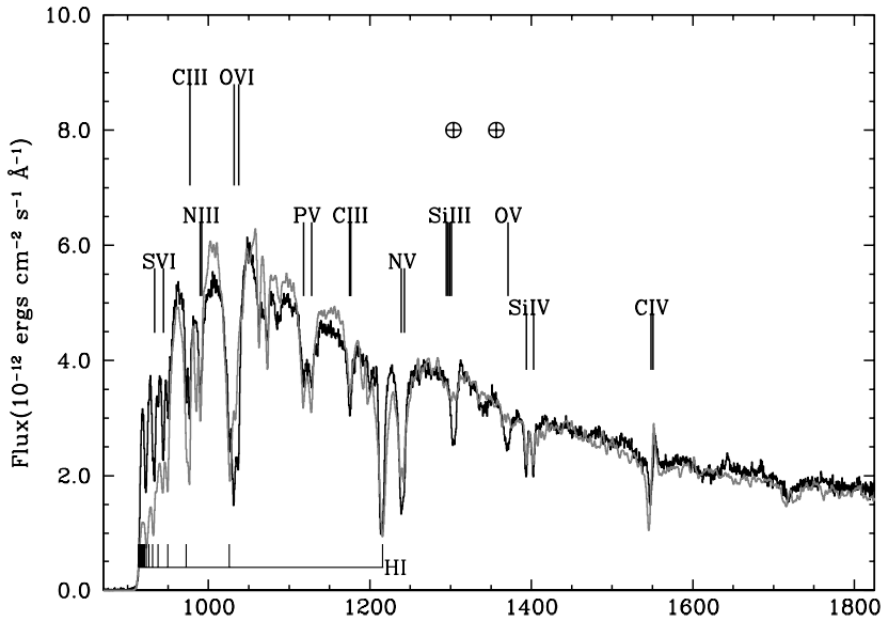


FIGURE 2.3: Credit: Long & Knigge 2002. UV spectrum of Z Cam, compared to a synthetic spectrum from MCRT simulations.

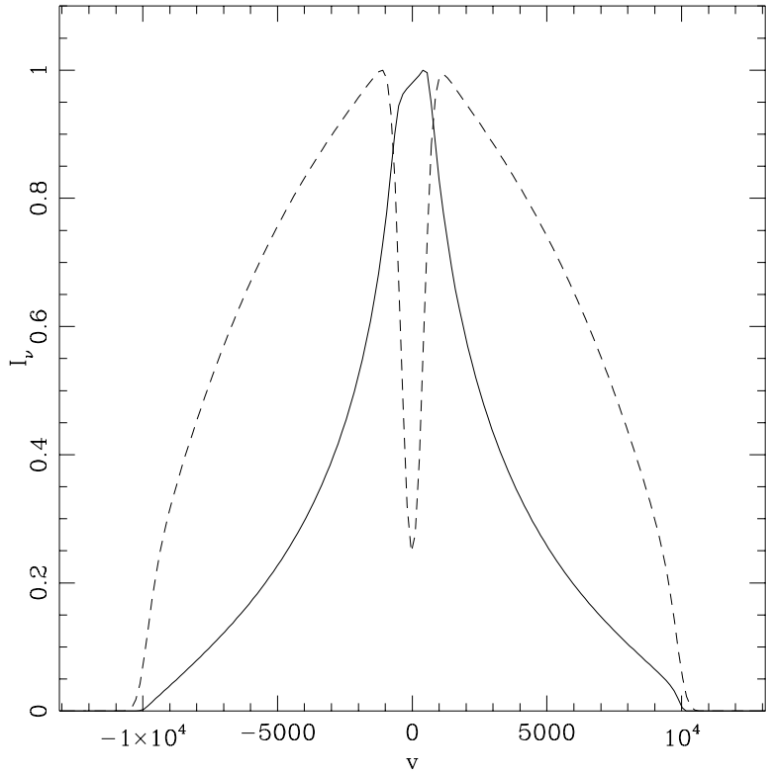


FIGURE 2.4: Credit: Murray & Chiang (1997). A comparison between a line profile, normalised to have peak intensity of 1, produced from a Keplerian disk (solid line) and the same model with an additional disc wind (dashed line). The radial velocity component of the disc wind modifies the escape probabilities across the disc, causing a single-peaked line to form.

Much less is known about the effect of these outflows on the optical spectra of high-state CVs. Direct evidence of wind-formed lines comes from isolated observations of P-Cygni-like line profiles in H α and He I λ 5876, ([Patterson et al. 1996](#); [Ringwald & Naylor 1998](#); [Kafka & Honeycutt 2004](#)). However, the effect on the *emission* aspects of the optical spectrum is not well known. [Murray & Chiang \(1996, 1997\)](#) have shown that the presence of disc winds may offer a natural explanation for the single-peaked optical emission lines in high-state CVs, since they can strongly affect the radiative transfer of line photons (Fig. 2.4; also see [Flohic et al. 2012](#)). Stronger support for a significant wind contribution to the optical emission lines comes from observations of eclipsing systems. There, the single-peaked lines are often only weakly eclipsed, and a significant fraction of the line flux remains visible even near mid-eclipse (e.g. [Baptista et al. 2000](#); [Groot et al. 2004](#)). This points to line formation in a spatially extended region, such as a disc wind. It is also possible that a wind may affect the continuum emission of CVs, as described. The effect of an accretion disc wind on the optical line and continuum emission of CVs is addressed directly in chapter 4.

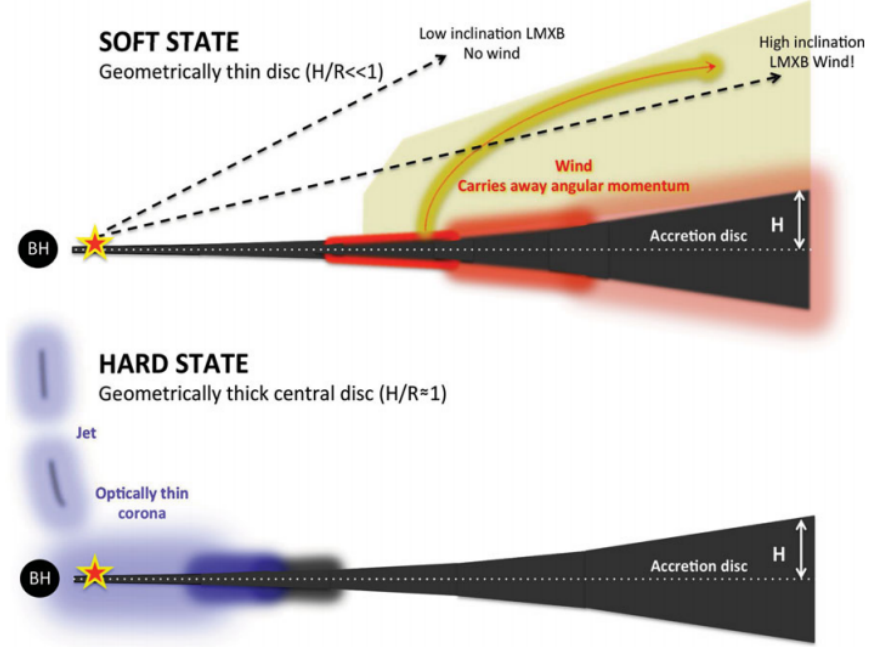


FIGURE 2.5: Credit: Ponti et al. 2012. A cartoon illustrating the expected geometry of soft-state LMXB winds.

2.1.2 X-ray Binaries

As in CVs, evidence for fast outflows in LMXBs is not constrained to a single waveband. UV absorption in outflows was detected when [Ioannou et al. \(2003\)](#) observed C IV $\lambda 1550$ P-Cygni profiles with blueshifts of $\sim 1500 \text{ km s}^{-1}$. A series of papers also found X-ray absorption features in similar objects ([Ueda et al. 1998](#); [Kotani et al. 2000](#); [Parmar et al. 2002](#)). These absorption features appeared to be preferentially detected in high-inclination, ‘dipping’ LMXBs. This was confirmed by [Ponti et al. \(2012\)](#), who proposed an equatorial outflow geometry based on this association (see Fig. 2.5). The same study demonstrated that the winds only appeared in the soft, disc dominated accretion state, on the opposite side of the HID to the region where jets are common (Fig. 2.6). This exciting result illustrates how important winds are to our understanding of accretion, and requires that we expand the discussion of accretion states from ‘disc-jet’ coupling to also include winds.

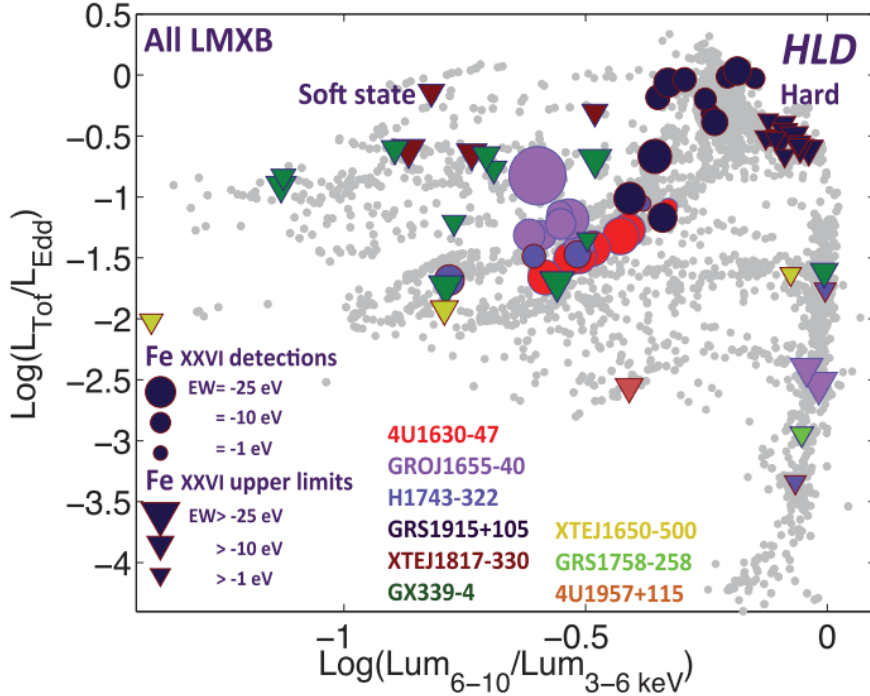


FIGURE 2.6: Credit: Ponti et al. 2012. Hardness-intensity diagram for four dipping LMXBs, demonstrating that winds appear only in the soft state.

2.1.3 AGN and Quasars

2.1.3.1 Broad Absorption Line Quasars

Perhaps the clearest evidence of outflows in AGN is provided by the blueshifted ($\sim 0.1 c$) ultraviolet BALs seen in approximately 20% of quasars (Weymann et al. 1991; Knigge et al. 2008; Dai et al. 2008; Allen et al. 2011). Five example spectra of BAL quasars from the HST and SDSS archives are shown in Fig. 2.7. In addition to the more common high-ionization BAL quasars (HiBALs), approximately 10% of BALQSOs show absorption in lower ionization species such as Mg II and Al III (LoBALs; Voit et al. 1993; Gibson et al. 2009) and an even smaller subset also show absorption in Fe II and III (FeLoBALs; Becker et al. 2000; Hall et al. 2002).

The simplest explanation for the incidence of BAL quasars (BALQSOs) is in terms of an accretion disc wind viewed from different angles. This principle of geometric unification is very similar to the idea behind the UP95 and AM95 models discussed in Chapter 1. According to this paradigm, a biconical wind rises from the accretion disc so that the BALQSO fraction is associated with the covering factor of the outflow. This fraction has been estimated by various authors using different selection criteria, with values

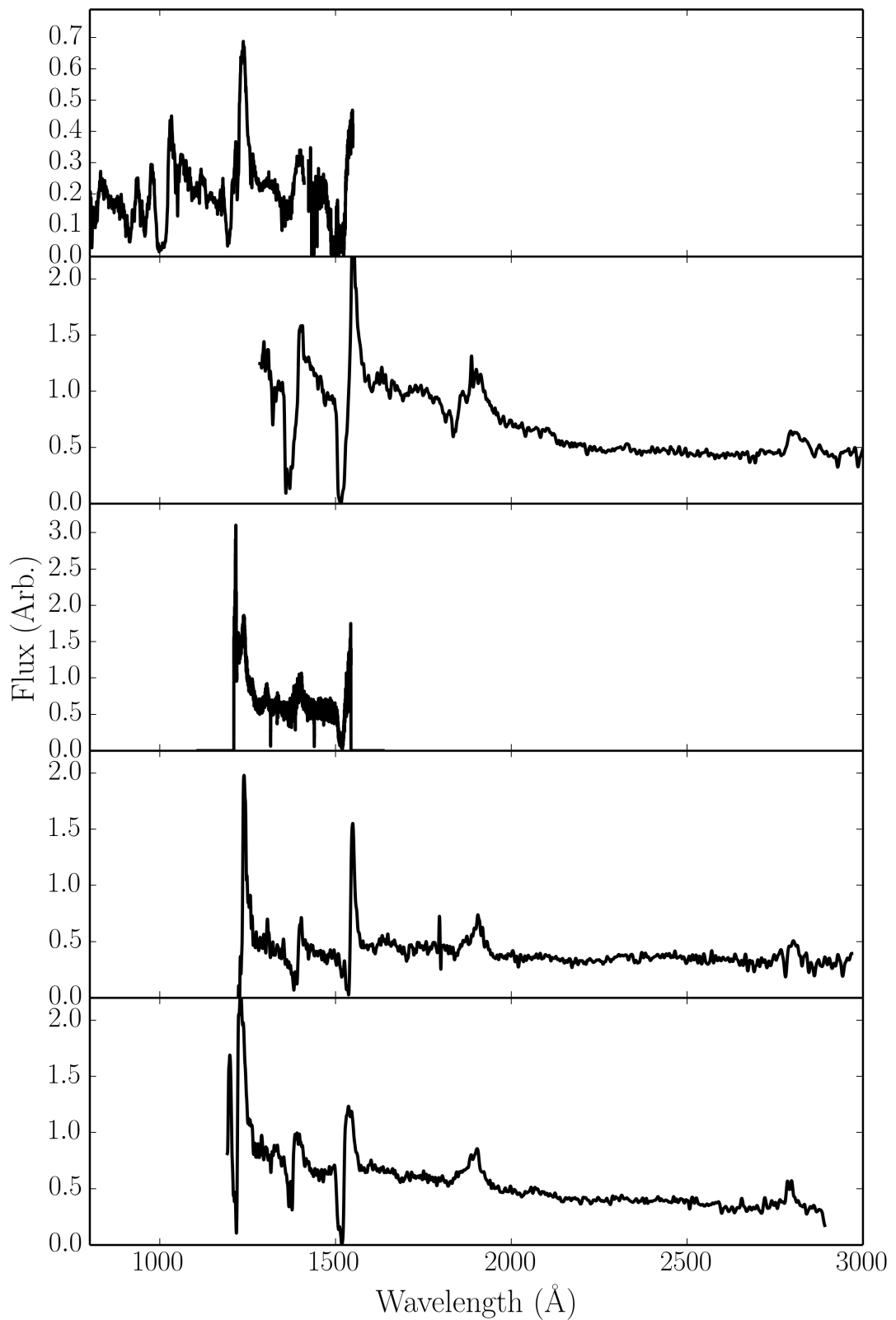


FIGURE 2.7: Five examples of BAL quasar spectra, from HST and SDSS.

ranging between 10% and 40% depending on the treatment of selection effects and the classification scheme used (Weymann et al. 1991; Trump et al. 2006; Knigge et al. 2008; Dai et al. 2008; Allen et al. 2011)

BAL quasars can also be interpreted in an *evolutionary* context, in which quasars spend a certain proportion of their life in the ‘BAL phase’. Models generally put this phase near the start of the quasar lifetime (Hazard et al. 1984; Surdej & Hutsemekers 1987; Boroson & Meyers 1992; Zubovas & King 2013), after a dust-enshrouded phase, but before the main quasar period. It is perhaps more likely that *both* evolutionary and geometric effects are at work (Borguet & Hutsemékers 2010; Dai et al. 2012). One of the main problems with testing these two paradigms is that many of the properties of BAL quasars fit naturally into either picture, and so disentangling their true nature is challenging. The latter chapters of this thesis attempt to address this issue by testing the geometric unification model and seeing how close this simple picture can get to explaining the BAL phenomenon.

While the BAL fraction, f_{BAL} , is a very useful number and must be at least related to the covering factor of the outflow, continuum selection effects (Goodrich 1997; Krolik & Voit 1998), as well as reddening (Allen et al. 2011), could significantly alter its true value. The degree of collimation of the BAL wind is also not well known. Polarisation studies suggest that the wind is roughly equatorial (Goodrich & Miller 1995; Cohen et al. 1995), as also found from hydrodynamical and radiative transfer simulations (Proga et al. 2000; Proga & Kallman 2004; Higginbottom et al. 2013), but there is also evidence for polar BAL outflows in radio-loud (RL) sources (Zhou et al. 2006; Ghosh & Punsly 2007). In addition to these uncertainties, the physical scale of the BAL phenomenon is also disputed and may vary from object to object. If one assumes that the BAL region is roughly co-spatial with the BLR, then the radius of the absorbing material can be estimated as $\sim 100r_G - 1000r_G$ from reverberation mapping and microlensing (e.g., for BLRs in BALQSOs, Sluse et al. 2015; O’Dowd et al. 2015). However, distances of ~ 0.1 pc ($\sim 10^4r_G$) have been estimated in at least some objects from atomic physics arguments and ionization models (Borguet et al. 2013; Chamberlain et al. 2015).

BAL quasars display a wide variety of different trough shapes, as shown in Fig. 2.7. The line profiles themselves often show complex structure (Foltz et al. 1987; Ganguly et al. 2006; Simon & Hamann 2010) and can be time variable (Hall et al. 2011; Capellupo

et al. 2011, 2012, 2014; Filiz Ak et al. 2012). Furthermore, there are a set of quasar absorption systems that show BAL-like absorption troughs with much smaller velocity widths. Depending on their width, these are known as narrow absorption lines (NALs) or ‘mini-BALs’ (Misawa et al. 2007, 2008; Nestor et al. 2008). While some of this behaviour can be explained once again as a viewing angle effect (e.g. Ganguly et al. 2001), the range of BAL profile shapes suggests that they are far from a homogenous population, and may also possess multi-scale substructures (clumps) in their flows. Clumping is discussed in more detail in sections 2.1.4 and 2.2.2, as well as in chapter 5.

The X-ray properties of BAL quasars are particularly important due to the strong ionizing potential of the X-ray radiation. BALQSOs are X-ray weak when compared to non-BAL quasars (Gibson et al. 2009). The X-ray weakness of BALQSOs is often attributed to X-ray absorption with column densities of $N_H \sim 10^{22-24} \text{ cm}^{-2}$ (Gallagher et al. 1999, 2002; Green et al. 2001; Grupe et al. 2003a; Stalin et al. 2011), although there is also evidence that BALQSOs are *intrinsically* X-ray weak (Sabra & Hamann 2001; Clavel et al. 2006; Morabito et al. 2013). The X-ray properties of BAL quasars are fundamentally coupled to the properties of the wind – the X-ray absorption may be caused by the outflow, which in turn has its ionization state determined by the X-ray radiation. Furthermore, the true X-ray luminosities cannot be reliably inferred until the inclinations of BALQSOs are constrained, as gravitational lensing can significantly alter the emergent angular distribution of X-ray emission even for an intrinsically isotropic source (Chen et al. 2013a,b).

Although the X-rays in BALQSOs are weaker than in similar mass quasars, they still possess strong ionizing power. This leads to what has become known as the ‘over-ionization problem’ in BALQSOs: how is the moderate ionization state of the BAL gas maintained in the presence of ionizing X-rays? A number of potential solutions have been proposed, which can be broadly separated into ‘shielding’ models (Murray et al. 1995; Proga & Kallman 2004) and ‘clumpy’ models (de Kool & Begelman 1995; Hamann et al. 2013). Some of these models are discussed further in section 2.3 and chapter 5.

2.1.3.2 Warm Absorbers

Warm absorbers (WAs) are regions of photoionized plasma responsible for some of the characteristic absorption features seen in the X-ray spectra of AGN (Reynolds & Fabian

1995). In particular, they produce photoelectric continuum absorption (e.g. Halpern 1984; Cappi et al. 1996; Kriss et al. 1996) and a series of narrow absorption lines in H-like and He-like ions of C, N, O, Si, Ne, and Fe (Kaastra et al. 2000), that appear in the soft X-rays. A wind origin is a common hypothesis for WAs (e.g. Krolik & Kriss 2001). Clear evidence for this comes from the measured blueshifts of the lines, typically on the order of $\sim 100 \text{ km s}^{-1}$. X-ray absorption and WAs are often variable (Fabian et al. 1994; Otani et al. 1996), which may be interpreted in terms of changing kinematics of an accretion disc wind (Connolly et al. 2014). There is also evidence of contemporary UV and X-ray absorption in NGC 5548 (Kaastra et al. 2014) and mini-BALS (Giustini et al. 2011), and as mentioned above BALQSOs are often absorbed in the X-rays. This suggests that the outflow phenomenon across a large range of ionization states and line energies is linked.

Some WAs be modelled well with single component models (Kaastra et al. 2000), but most require multiple absorbers with different ionization states (e.g. Kriss et al. 1996; Orr et al. 1997; Krolik & Kriss 2001; Connolly et al. 2014). If this is the case, then self-consistent ionization and radiative transfer models should really be used to model the spectrum (see e.g. chapter 3), as optically thin ionization parameter estimates will not capture the ionization and radiation physics. The collated observations point towards some kind of outflow with a stratified ionization structure, with $\log \xi \sim 0 - 2$, and densities on the order of 10^8 cm^{-3} . These physical conditions or scales are not well constrained, and the connection to other outflows is unknown. Timing observations may help to shed light on the properties of the mysterious, but ubiquitous, AGN WAs (Silva et al. 2015).

2.1.3.3 Ultra-fast Outflows

As well as acting as WAs, winds can also imprint clear absorption features in highly ionized Fe K α lines in AGN such as PDS 456 (Reeves et al. 2003; Gofford et al. 2014; Matzeu et al. 2016), MCG-5-23-16 (Braito et al. 2007) and PG 1211+143 (Pounds & Reeves 2009; Fukumura et al. 2015). These outflow signatures are fairly common in Seyfert galaxies (Tombesi et al. 2010; Gofford et al. 2013). One example of such a feature is shown in Fig. 2.8 along with a simple spherical outflow model fit (Nardini

et al. 2015). The high velocities ($\sim 0.1c$) inferred from the line blueshifts have lead to these winds becoming known as ultra-fast outflows, or UFOs.

UFOs are characterised by ionization parameters in the range $\log \xi \sim 3 - 4$ and column densities $N_H > 10^{22} \text{ cm}^{-2}$. Their high mass-loss rates and large energy budgets mean that they are natural candidates for AGN feedback (see section 2.5). Measurements of their kinetic luminosities suggest that UFOs have sufficient energy to affect their host galaxy (Gofford et al. 2015). In fact, a large-scale molecular outflow has recently been detected in one UFO host, possibly driven by the UFO itself (Tombesi et al. 2015). As with WAs, many of the models used to constrain physical parameters are simplistic, and assume single ionization parameters, large covering factors and thin expanding shells of outflow. Under these assumptions, the mass loss rate can be estimated using

$$\dot{M} \sim \Omega N_H m_p v_{out} R_{in} \quad (2.1)$$

In reality, the absorber is probably much more complex, and full RT and photoionization simulations are required to accurately model the expected spectrum. In a series of papers, Sim et al. (2008, 2010b,b) carried out such calculations and found that reasonable verisimilitude with Fe line profiles could be achieved. However, as with many models of AGN, a holistic, broad wavelength range fit is still required.

2.1.4 Stellar Winds

Although stellar winds are clearly not accretion disc winds, they provide a useful, and better understood, testing ground for much of the physics of radiatively-driven outflows. Wolf-Rayet (WR) stars and O-stars possess strong outflows with mass-loss rates of up to $10^{-5} M_\odot \text{ yr}^{-1}$, thought to be driven by radiation pressure mediated by spectral lines (see section 2.2.3). Over the typical lifetime of a massive star ($\sim 10^6 \text{ yr}$), this can have a significant impact on the overall stellar mass, causing losses of around $10 M_\odot$ of material.

As with the systems described previously, the P-Cygni profiles in spectra from hot, massive stars are the main pieces of evidence that a strong wind is present (see Fig. 2.9). Mass-loaded winds are also thought to be responsible for the emission lines seen in hot star spectra (e.g. Pauldrach et al. 1994). Indeed, emission line diagnostics have been

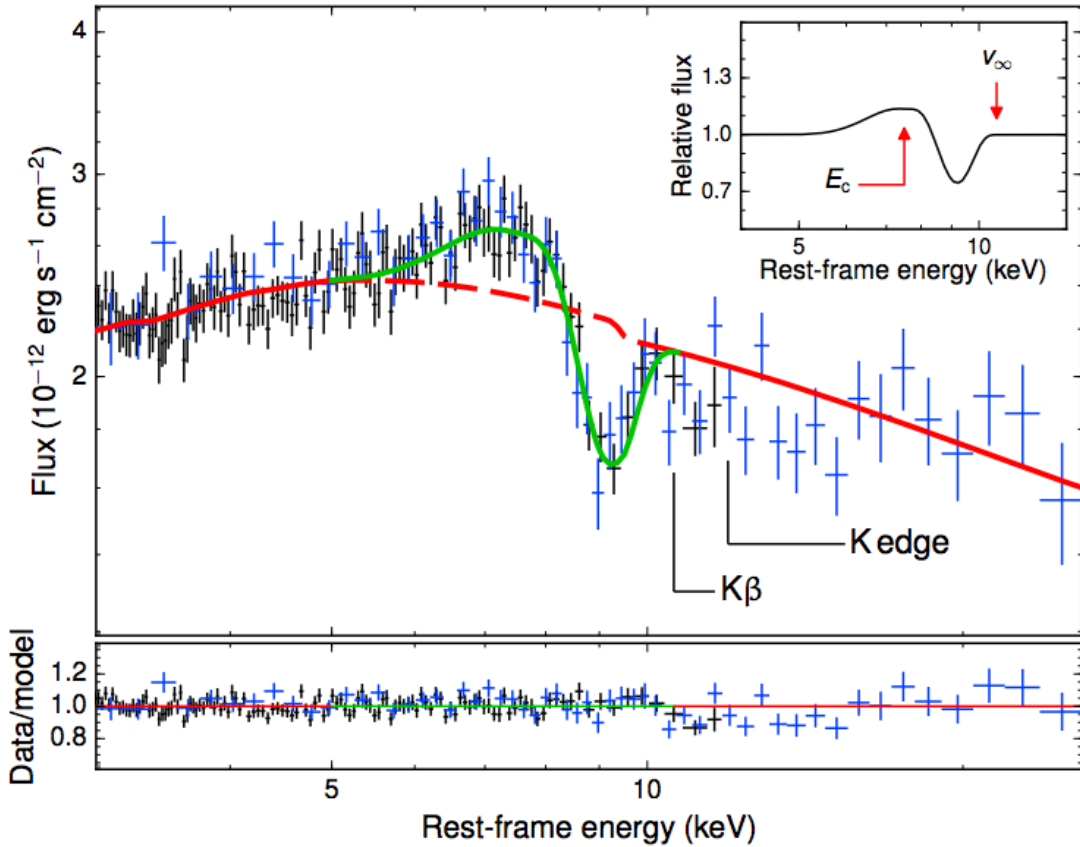


FIGURE 2.8: Credit: Nardini et al. 2015. X-ray spectrum of PDS 456 fitted with a P-Cygni profile from a spherical outflow model. XMM-Newton data is shown in black with two combined NuStar observations in blue.

particularly important in determining the mass-loss rates of stellar winds and have also been used to demonstrate that line-driven stellar winds are clumpy.

2.1.4.1 Clumping in Stellar Winds

Evidence for clumping in hot star winds comes from a range of sources. Perhaps the most conclusive is from electron scattering wings in emission lines; homogenous models overestimate the strength of these wings, whereas clumpy models produce good agreement with data (Hillier 1984, 1991; Hamann et al. 1992, 1994; Schmutz 1997). Further evidence for clumping comes from line variability (Prinja & Smith 1992) and polarisation (Brown et al. 1995). Clumping is theoretically expected in line-driven winds (see section 2.2.3 and the review by Owocki 2014), and is directly dealt with in this thesis. In chapter 5, I describe the treatment of clumping I have implemented in our radiative transfer code, before presenting results from a clumpy AGN wind model.

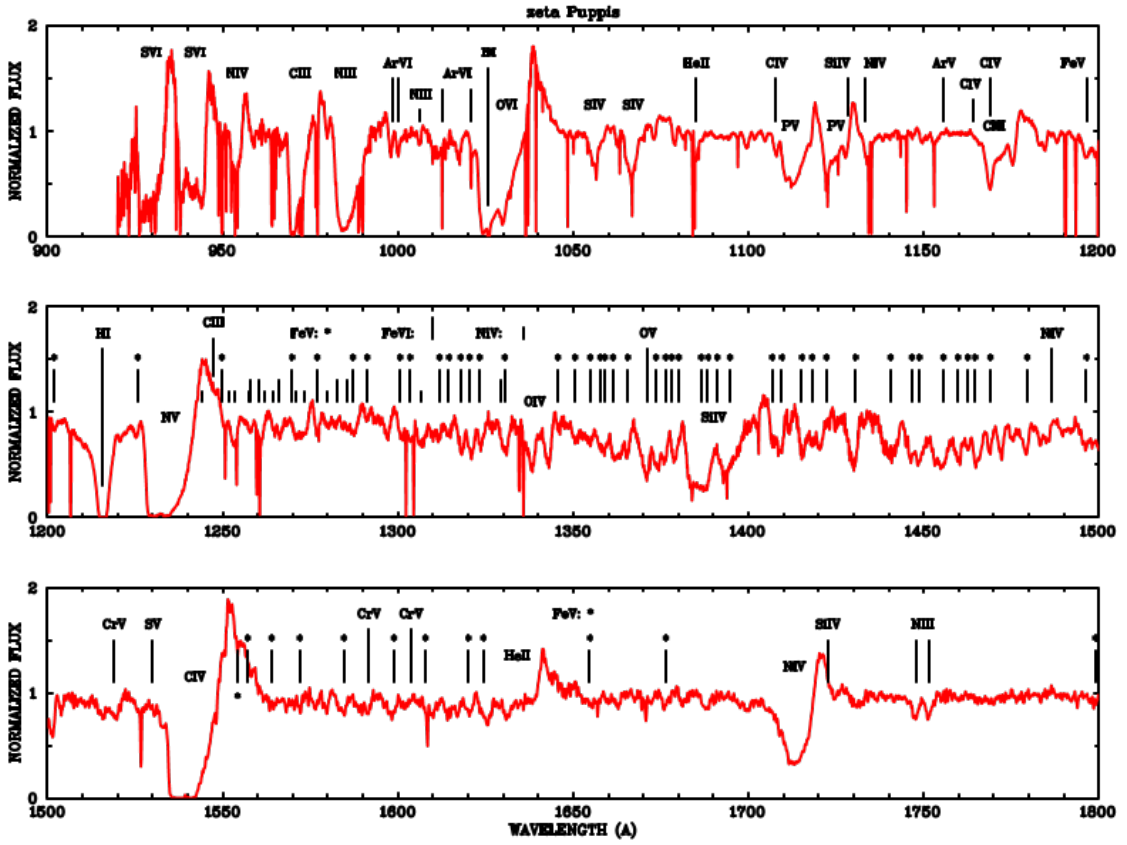


FIGURE 2.9: Credit: Pauldrach et al. 1994. UV spectrum of one of the brightest massive O stars, the O4 supergiant ζ Puppis. The spectrum is merged from Copernicus and IUE UV observations, and the prominent lines are marked.

2.1.5 Outflow Physics

The spectra in figures 2.2, 2.7 and 2.9 show striking similarities – characteristic broad, P-Cygni-like absorption features in UV resonance lines extending to high blueward velocities – despite vast differences in mass. Furthermore, some of the phenomena observed in e.g. stellar winds may naturally solve some of the unanswered questions in other systems. For example, clumping may prevent over-ionization in AGN outflows. It would seem that at least some of the physics of outflows, like accretion physics, is universal, and that lessons learned from smaller scale systems may be scaleable to AGN and quasars. In order to understand if the similarity extends beyond a cosmetic one, I will discuss some of the underlying physical mechanisms that may be responsible for accelerating these outflows.

2.2 Driving Mechanisms

Let us consider a parcel of ideal gas. By imposing nothing more than conservation of mass, energy and momentum on that parcel we can write down three equations of hydrodynamics:

$$\frac{D\rho}{Dt} + \rho \nabla \cdot \vec{v} = 0, \quad (2.2)$$

$$\rho \frac{D\vec{v}}{Dt} = -\nabla P + \frac{1}{4\pi}(\nabla \times \vec{B}) \times \vec{B} + \rho \vec{g}_{rad} + \rho \vec{g}, \quad (2.3)$$

$$\rho \frac{D}{Dt} \left(\frac{e}{\rho} \right) = P \nabla \cdot \vec{v} + \rho \mathcal{L}. \quad (2.4)$$

Here D denotes a derivative within the comoving frame of the gas parcel, \vec{v} is the velocity, ρ is the gas density, \vec{B} is the local magnetic field, \vec{F}_{rad} is the radiation force per unit mass and \vec{g} denotes the gravitational acceleration vector. Equation 2.2 is the *continuity equation* and describes conservation of mass. Equation 2.3 is the *equation of motion* and describes conservation of momentum. Equation 2.4 is the *equation of energy conservation*. Equation 2.3 can be used to neatly demonstrate how an outflow can be driven. I have deliberately written the equation so that all the force terms lie on the RHS. For an outflow to be driven from an accreting object, one of the terms on the RHS must dominate over gravity, $\rho \vec{g}$. These terms thus signify three potential driving mechanisms.

- Magnetic / Lorentz Forces, $\frac{1}{4\pi}(\nabla \times \vec{B}) \times \vec{B}$.
- Radiative Forces, $\rho \vec{g}_{rad}$.
- Thermal Pressure, $-\nabla P$.

We can now examine under what physical conditions (and in which corresponding astrophysical objects) we might expect these forces to overcome gravity and cause a parcel of mass to escape to infinity. In other words: *what might drive a wind?*

2.2.1 Thermal Winds

In a disc in hydrostatic equilibrium (HSE), thermal pressure balances gravity in the vertical direction. The equation of motion in this z direction can then be written as

$$\rho \frac{Dv_z}{Dt} = -\frac{\partial P}{\partial z} + \rho g_z = 0 \quad (2.5)$$

Clearly, if the thermal pressure is significantly increased, this equilibrium condition no longer holds. This can occur in accretion discs at temperatures in excess of $\sim 10^7$ K – where other forces are negligible compared to thermal pressure – and where the escape velocities are relatively low (i.e. far out in the disc). Due to the temperature and gravity scalings, this means that XRBs are natural candidates for showing evidence of thermally driven winds. The outer disc can be heated to the Compton temperature by the central X-ray source, potentially driving relatively high mass-loss rate outflows ([Begelman et al. 1983](#); [Woods et al. 1996](#)). This driving mechanism has been proposed as a natural explanation for the ever-present equatorial outflows in soft state XRBs ([Ponti et al. 2012](#)). However, they are much less likely candidates in CVs and AGN, because the escape velocity tends to greatly exceed the thermal velocity.

2.2.2 Radiatively Driven Winds

Under spherical symmetry, one simply obtains the Eddington limit discussed in section 1.1.1 when $\rho \vec{F}_{rad} = \rho \vec{g}$. Hence, sources must be fairly close to the Eddington luminosity in order to drive an outflow purely from radiation pressure on electrons. There are a number of accreting systems that may drive super-Eddington (or close to Eddington) outflows, such as AGN with UFOs (e.g. [Reeves et al. 2002](#); [Pounds et al. 2016](#)), NLSIs ([Done & Jin 2015](#)) and ultra-luminous X-ray sources (ULXs; [Walton et al. 2013](#)). However, high-state CVs are significantly below the Eddington limit ([Warner 2003](#)), and at least some BALQSOs have low Eddington fractions ([Grupe & Nousek 2015](#)). Despite this, line opacity may mean that radiation is still responsible for the powerful outflows in these systems even at $L/L_{Edd} \sim 10^{-3}$.

2.2.3 Line-driven Winds

Under the right ionization conditions, radiation pressure mediated by spectral lines can be a significant acceleration term in a partially ionized plasma (Castor et al. 1975, hereafter CAK). The most common way to parameterise the cumulative effect of lines on the radiation force is via the *CAK force multiplier*, $\mathcal{M}(t)$, which modifies the equation for the acceleration due to radiation to give (Castor 1974, CAK)

$$\vec{g}_{rad} = \frac{\sigma_T F}{\mu c m_p} \mathcal{M}(t), \quad (2.6)$$

where F is the flux, and μ is the mean atomic weight. $\mathcal{M}(t)$ can be approximated by

$$\mathcal{M}(t) = t^{-\alpha} \left(\frac{n_e}{10^{11} \text{ cm}^{-3}} \right)^\delta W^{-\delta}, \quad (2.7)$$

where t is the dimensionless optical depth, given by

$$t = \frac{\sigma_T \rho v_{th}}{m_p |d(v_i)/ds|} \quad (2.8)$$

Here W is the dilution factor, and k , α and δ are constants with values of 0.28, 0.56 and 0.99 respectively in O-star winds (Abbott 1982). v_i is the component of the velocity field in the direction being considered, normally a line between the source of radiation and the wind. It is possible to show (CAK, Owocki et al. 1988) that the maximum force multiplier is around 2000 – 4000. This is already an interesting result, as it tells us that line-driven outflows can be accelerated when accretion rates / luminosities are much lower than the Eddington limit. Indeed, using equation 2.6 we can see that a radiatively driven wind can be accelerated when $L_{UV} > L_{Edd}/M_{UV}(t)$, where the UV subscript pertains to the UV region of the spectrum and $M_{UV}(t)$ will thus depend on the lines in this region and their relative ionization and excitation fractions. Line-driven winds are present in O-stars and Wolf-Rayet stars and the theory produces good matches with observations (e.g. Friend & Abbott 1986; Pauldrach et al. 1986, 1994; Hamann et al. 2008). It is also a strong candidate for driving the winds seen in high-state CVs when the accretion disc is UV bright (Pereyra et al. 1997; Proga et al. 1998; Proga 2005, see also section 2.3.4).

Line driving is also a promising mechanism to explain BAL outflows, as the strong UV resonance lines seen in absorption in O stars are also present in BALQSOs. The

presence of ‘line-locked’ features (Bowler et al. 2014) and the ‘ghost of Ly α ’ (Arav et al. 1995; Arav 1996; North et al. 2006) in the spectra of some BALQSOs also suggests that line-driving is at least contributing to the acceleration of the wind (but see also Cottis et al. 2010). However, the presence of an X-ray source complicates matters. I have already briefly touched on the ‘over-ionization’ problem in AGN outflows, but it now has another consequence. Not only will strong X-rays prevent the right features forming in the spectrum, but, if the outflow is line-driven, they will prevent the wind existing in the first place. Despite these problems, hydrodynamic simulations have been successful in producing high mass-loss rates (see section 2.3.4).

Line-driving is subject to a strong instability known as the line deshadowing instability (LDI; Lucy & Solomon 1970; MacGregor et al. 1979; Owocki & Rybicki 1984, 1985). The basic idea is that any velocity perturbation in a line-driven flow can cause a ‘deshadowing’ effect, as the fluid element will now be in resonance with a region of the spectrum that is less absorbed. Thus, an increase in the line force will occur in proportion with this velocity perturbation, and the instability can grow. Time-dependent numerical modelling of the LDI has shown that it can produce a clumpy flow (Owocki et al. 1988; Feldmeier 1995; Šurlan et al. 2012; Owocki 2014) that may explain the observational characteristics of clumping in stellar winds (see section 2.1.4.1). The LDI is also of interest in CV and AGN winds, as it may affect the ionization state of the flow and possibly the inferred mass-loss rates.

2.2.4 Magnetic Winds

There is still great uncertainty over the magnetic fields in accretion discs and the physics of these magnetic processes, but, in many senses, they are attractive mechanisms as magnetic processes are already expected to be important in accretion disc winds due to the MRI. There are two main ways in which magnetic forces can drive an accretion disc wind, which are best explained by writing down an alternative form for the Lorentz force,

$$\vec{F}_m = \frac{1}{4\pi} \vec{B} \cdot \nabla \vec{B} - \nabla \frac{B^2}{8\pi}. \quad (2.9)$$

The first term can be thought of as a magnetic *tension* associated with the field lines and the second as an isotropic magnetic *pressure*.

Historically, the most popular magnetic wind model has been the ‘bead on a wire’ mechanism proposed by [Blandford & Payne \(1982\)](#) and [Pelletier & Pudritz \(1992\)](#). In these models, the poloidal magnetic field is dominant and is anchored in the accretion disc. A wind can then be driven by magnetic tension, as the first term in the above equation operates on fluid elements (‘beads’) on the surface of the accretion disc. This can accelerate a wind when the poloidal component of the field makes an angle of $> 30^\circ$ with the normal to the disc surface. These models are known as magnetocentrifugal winds as it is the interaction between a centrifugal force and a strong, large-scale, ordered magnetic field threading the disc that drives the wind. Magnetocentrifugal winds have been proposed in both AGN and YSOs ([Pelletier & Pudritz 1992](#); [Konigl & Kartje 1994](#); [Kudoh & Shibata 1997](#)), and numerical simulations have demonstrated that this mechanism can produce jets and outflows ([Romanova et al. 1997](#); [Ouyed & Pudritz 1997](#); [Ustyugova et al. 1999](#)).

In an alternative magnetohydrodynamic (MHD) model the isotropic magnetic pressure is responsible for driving the outflow ([Proga 2003](#)). In this case the toroidal component dominates over the poloidal component and drives a slow, dense outflow which behaves more like a thermally-driven wind (i.e. it conserves specific angular momentum rather than angular velocity).

2.3 Accretion Disc Wind Models

A number of different wind models have appeared in the literature over the years, each attempting to explain the different observational characteristics of quasars with a mixture of conceptual frameworks and underlying physics. Typically, the models attempt to explain the origins of BLR and BAL gas, although some extend their remit into the infra-red, radio and X-ray regimes. I will briefly discuss a few examples that have gained traction over the years, before outlining the kinematic prescription I have used in the modelling that forms part of this thesis.

2.3.1 MCGV95: A Line-driven Wind Model for AGN

MCGV95 proposed a model in which a smooth wind rises from an accretion disc with a launch radius of around 10^{16} cm. The wind is equatorial, with an opening angle of

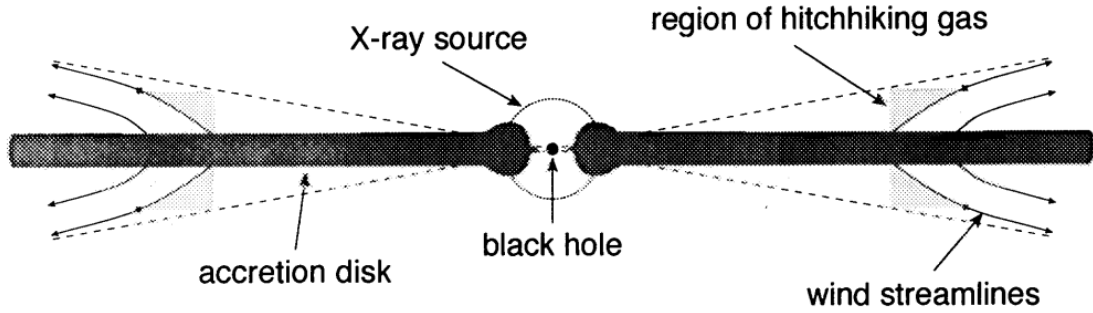


FIGURE 2.10: Credit: Murray et al. 1995. Cartoon showing the geometry of the MCGV95 model.

5° , and is accelerated by line forces up to a terminal velocity of $0.1c$. A sketch of the geometry is shown in Fig. 2.10. One of the key features of the model is the presence of a ‘shield’ of hitchhiking gas, which protects the outflow from X-ray over-ionization and allows radiation pressure on UV resonance lines to efficiently accelerate the flow.

MCGV95 found that BAL profiles were seen for an observer looking into the wind cone, and significant collisionally excited line *emission* emerged at low inclinations. This line emission came from a relatively small BLR ($r_{BLR} \sim 10^{16}$ cm) at the base of the wind, where densities were high ($n_e \approx 10^{10}$ cm $^{-3}$). The MCGV95 model was one of the first successful disc-wind unification models. It is especially impressive as it includes photoionization calculations and quantitative estimates of the resultant line EWs. However, the effects of multiple scattering and complex radiative transfer effects could not be included in the calculations (see chapter 5).

2.3.2 De Kool & Begelman: A Radiatively Driven, Magnetically Confined Wind

It is, of course, possible that radiation and magnetic fields are both important in determining the outflow characteristics. In the [de Kool & Begelman \(1995\)](#) model, radiation pressure drives an outflow from an accretion disc and also compresses the magnetic field lines that are dragged along with the flow. This causes the magnetic field strength in certain regions to be comparable to the gas pressure, meaning that clouds can be magnetically confined in the flow. A diagram is shown in Fig. 2.11. The authors find that such a model would naturally emerge at a fairly equatorial angle with a covering factor

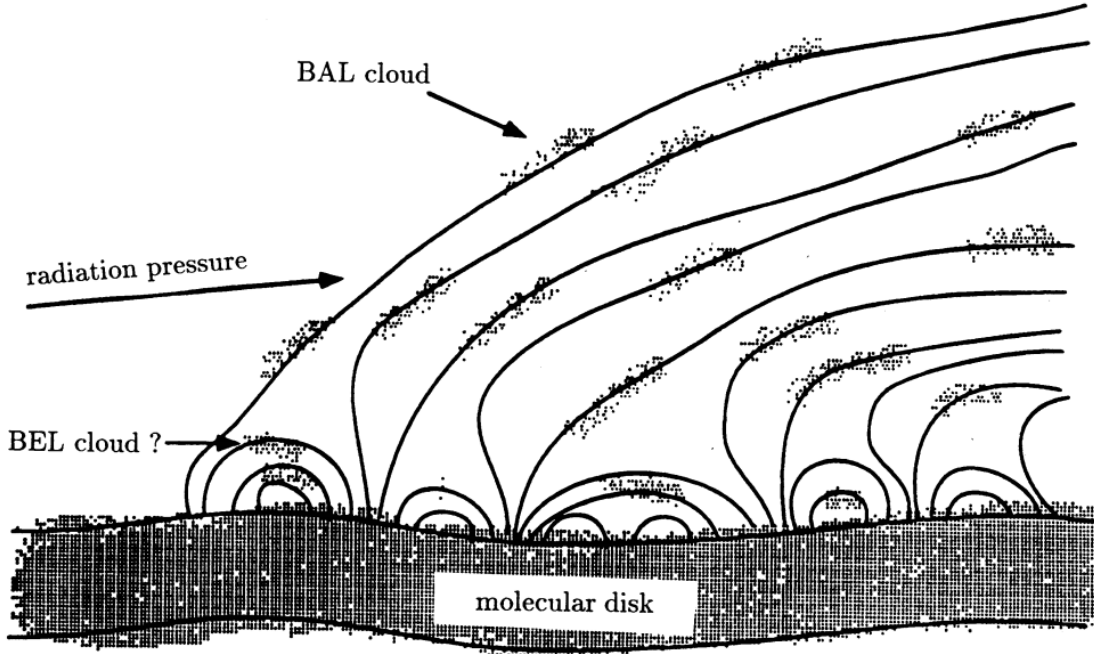


FIGURE 2.11: Credit: De Kool & Begelman 1995. A cartoon showing the components in the De Kool & Begelman model.

of around 10%, and that lower ionization material would be intercepted when the system was viewed from higher inclinations, potentially explaining some of the properties of LoBALQSOs.

2.3.3 Elvis 2000: A Structure for Quasars

[Elvis \(2000\)](#) expanded on the work of MCGV95 by proposing a simple disc wind model, empirically derived to explain as much of quasar phenomenology as possible within one unifying framework. The geometry of the Elvis' is shown in Fig. 2.12. As in the two previous models, observers looking into the wind cone will see a BALQSO, whereas observers looking down onto the wind will see a type 1 quasar. Initially, the wind rises vertically, so that observers looking underneath the flow will see NALs due to the small range of velocities intercepted by their line of sight.

The flow conserves angular momentum, such that the initial Keplerian velocities determine the BEL widths, before accelerating to BAL-like velocities of $\sim 0.1c$. The wind is assumed to be two-phase, with BEL and BAL clouds embedded in a warm, highly ionized medium (WHIM). This WHIM is responsible for WA-like absorption and the X-ray scattering phenomena seen in AGN. It is also responsible for confining the BAL

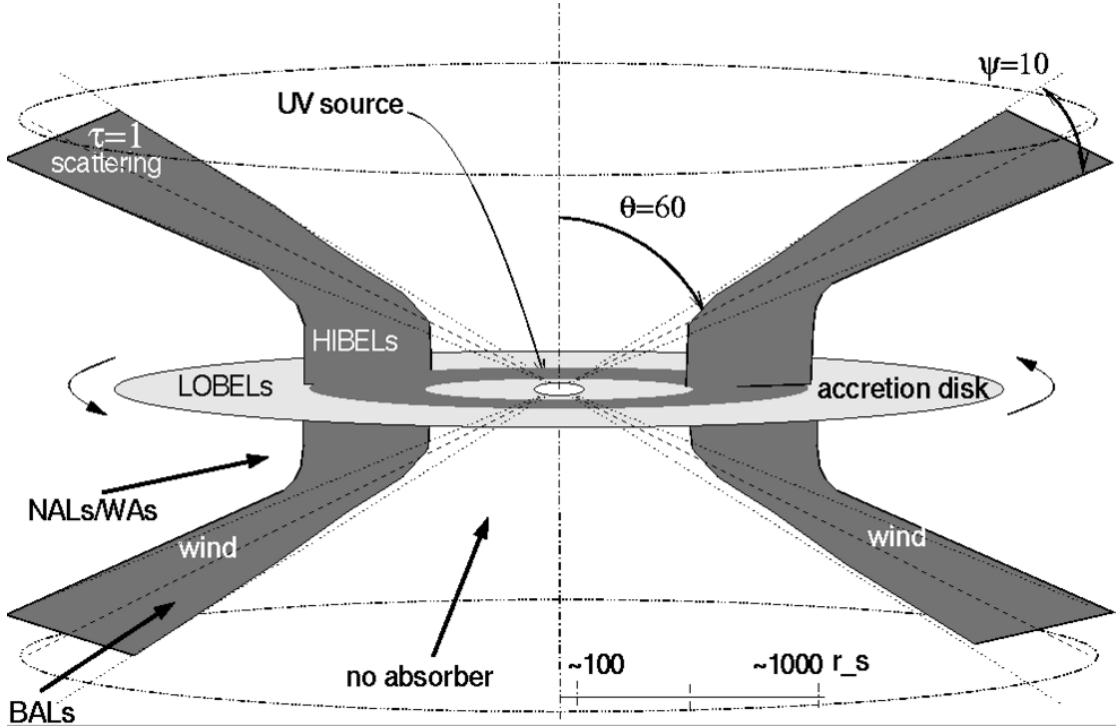


FIGURE 2.12: Credit: Martin Elvis. A schematic showing the main features of the Elvis model. A biconical wind rises from an accretion disc, and the observed spectrum is determined purely by the viewing angle of the observer.

and BEL clouds, allowing high densities and cooler temperatures to exist within the flow. The ionization structure for the wind is stratified, such that the material further out along the disc plane is somewhat shielded from the inner disc and X-rays. This allows the lower ionization BEL profiles to form in the right locations, and also means that LoBAL profiles would be seen at a subset of inclinations.

2.3.4 Proga et al.: Line-driven Hydrodynamic Models for AGN and CVs

Around the turn of the century, Daniel Proga and collaborators published a series of important papers in which they conducted hydrodynamic simulations of line-driven disc winds in AGN and CVs. In the first of these, the problem considered was that of disc winds in CVs (Proga et al. 1998). In their model, the disc was assumed to radiate according to the α -disc model, and the central WD was also included as a radiating source. They found that when the disc had an Eddington fraction of greater than $\approx 1/\mathcal{M}_{max}(t) = 0.001$, then strong, line-driven outflows were driven from a few WD radii with bending angles of $\sim 45^\circ$. This result agreed qualitatively with outflows in

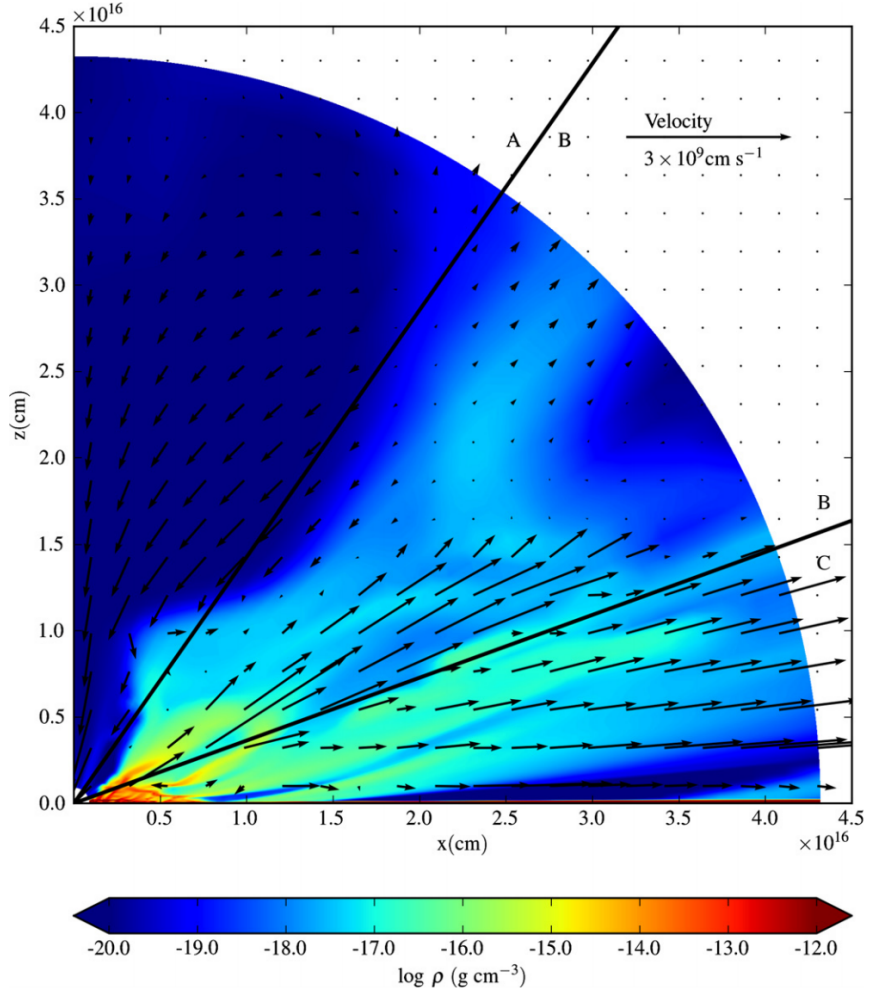


FIGURE 2.13: Credit: Higginbottom et al. 2014.. A snapshot of the PK04 model. Colours shows the density and arrows show the velocity of the flow. The radial lines separate three areas described by H14.

CVs, and later efforts to compute synthetic line profiles produced promising results (Proga et al. 2002). This was the first successful demonstration of line driving in a full hydrodynamic simulation.

The same principle was then applied to the problem of AGN outflows, with the additional complication of an ionization X-ray source now included (Proga et al. 2000; Proga & Kallman 2004, hereafter PK04). A density snapshot from the PK04 model is shown in Fig. 2.13. An inner ‘failed’ wind formed in this simulation, which initially rose up from the disc before being over-ionized by the central X-rays. Crucially, this acted as a shield, similarly to the hitchhiking gas proposed by MCGV95, and allowed a line-driven wind to be accelerated further out in the disc. This outflow can be seen clearly in Fig. 2.13.

One of the interesting results of the Proga-led simulations is that they tended to produce

somewhat unsteady, clumpy flows. In the CV case, this was caused by the interaction between the line force and gravity, as both force terms varied differently with height. In the AGN case, it was instead due to the critical importance of the ionization state on the line force. Parcels of gas can only be accelerated when if they have the ‘right’ ionization state, and this depends critically on their density and the radiation field they see. This causes an interplay between the dynamics of the flow and the path of ionizing radiation, which are coupled. The radiation field also helped determine the geometry of the outflow, as increasing the strength of the radiation interior to the launch radius tends to flatten out the wind and lead to more equatorial outflows ([Proga 2005](#)). This is particularly important when considering quasar unification, as it means the viewing angles of BALQSOs can provide information about where the wind is launched.

It is worth noting that the smaller scale LDI could not be included in this model, partly for computational reasons and partly because of the approximations used to treat the radiation field. Treating the radiation transport is also important for other reasons. [Higginbottom et al. \(2014\)](#), hereafter H14) showed that, in this particular geometry, multiple scattering renders shielding region ineffective, and radiation will simply find its way around the failed wind to over-ionize the flow beyond. Ideally, full radiative transfer and hydrodynamical simulations would be used to estimate the viability of line-driven winds. Our team is currently working on this problem (see H14 for the first step); however, much can also be learned from simpler, kinematic prescriptions for outflows, which can then be treated with full radiative transfer and ionization treatments.

2.4 A Kinematic Prescription for a Biconical Wind

[Shlosman & Vitello \(1993\)](#), hereafter SV93) expanded on the work of the stellar wind community (e.g. [Abbott & Lucy 1985](#)) in proposing a kinematic model for an accretion disc wind. Unlike hydrodynamical models, this model has no real predictive power in terms of velocities and mass-loss rates. Instead, one sets these quantities in advance and examines the resultant properties of the flow and emergent spectra. The SV93 prescription is the most common way of describing the outflow in the radiative transfer code PYTHON (see chapter 3) and has been used to simulate spectra for CVs ([Long & Knigge 2002](#); [Matthews et al. 2015](#), chapter 4), AM CVn systems ([Kusterer et al. 2014](#)) and AGN/quasars ([Higginbottom et al. 2013](#); [Matthews et al. 2016](#); [Yong et al. 2016](#),

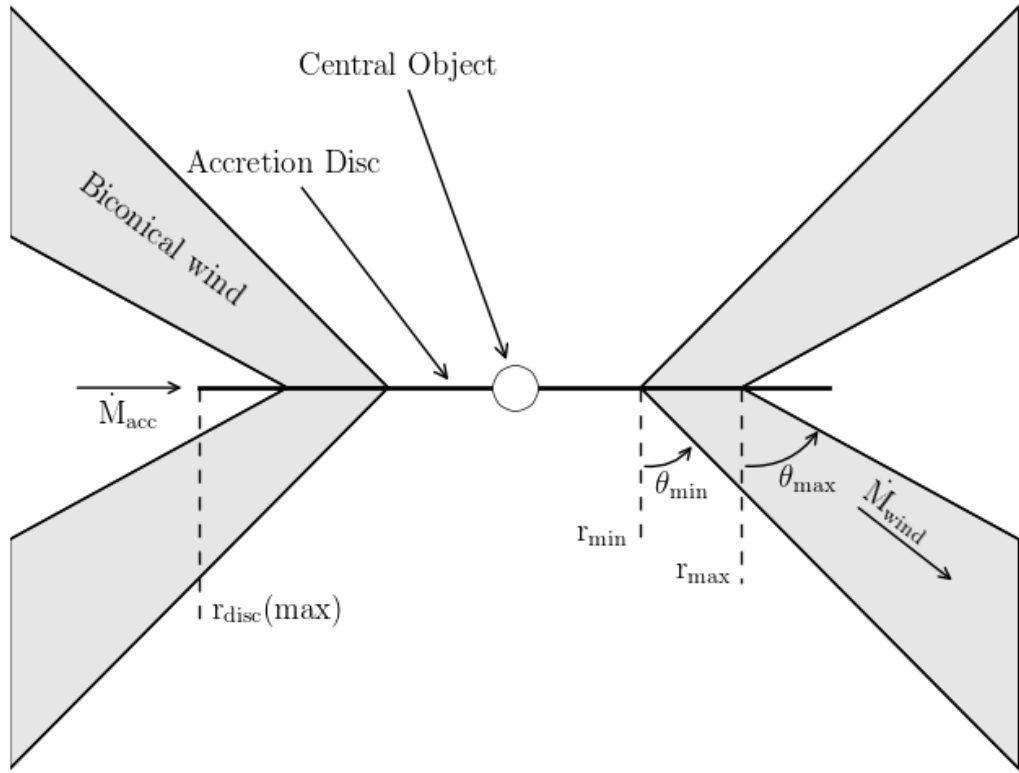


FIGURE 2.14: A schematic showing the geometry and kinematics of the SV93 model.

chapter 5). A similar philosophy applied to the model of Knigge et al. (1995), which has been used in similar applications (Long & Knigge 2002; Sim et al. 2008, 2010a), as well as for young-stellar objects (YSOs; Sim et al. 2005). Kinematic prescriptions have thus been a useful tool in providing quantitative tests of conceptual models, and specifically for assessing their ability to reproduce the observed spectra of a variety of disc wind systems.

In the SV93 parametrization, a smooth, biconical disc wind emanates from the accretion disc between r_{\min} and r_{\max} . A schematic is shown in Fig. 2.14. The covering fraction of the outflow is also controlled by the inner and outer opening angles of the wind, θ_{\min} and θ_{\max} , and the launch angle of the other streamlines is given by

$$\theta(r_0) = \theta_{\min} + (\theta_{\max} - \theta_{\min}) \left(\frac{r_0 - r_{\min}}{r_{\max} - r_{\min}} \right)^{\gamma}, \quad (2.10)$$

where r_0 is the launch radius of the streamline.

The poloidal (non-rotational) velocity field of the wind, v_l , is given by

$$v_l = v_0 + [v_\infty(r_0) - v_0] \frac{(l/R_v)^\alpha}{(l/R_v)^\alpha + 1}, \quad (2.11)$$

where l is the poloidal distance along a particular wind streamline. The terminal velocity along a streamline, v_∞ , is set to a fixed multiple of v_{esc} , the escape velocity at the launch point. The terminal velocity will therefore be higher for streamlines closer to the inner disc edge. The launch velocity from the disc surface, v_0 , is assumed to be constant (set to 6 km s⁻¹). Once the wind is launched, it accelerates, reaching half of its terminal velocity at $l = R_v$. The velocity law exponent α controls how quickly the wind accelerates. Larger values of α cause the main region of acceleration to occur close to R_v , whereas smaller values correspond to fast acceleration close to the disc (see Fig. 2.15). The rotational velocity v_ϕ is Keplerian at the base of the streamline and the wind conserves specific angular momentum, such that

$$v_\phi r = v_k r_0, \quad (2.12)$$

where $v_k = (GM_{WD}/r_0)^{1/2}$.

The mass-loss rate per unit surface area, \dot{m}' , can be controlled by a free parameter λ_m such that

$$\dot{m}' \propto \dot{M}_W r_0^{\lambda_m} \cos[\theta(r_0)], \quad (2.13)$$

where \dot{M}_W is the total mass loss rate in the wind. This equation is normalised so that when integrated over both sides of the disc the correct \dot{M}_W emerges. I have adopted $\lambda = 0$ throughout this thesis, which corresponds to uniform mass loss across the disc. The density at a given point can then be calculated by imposing mass conservation and using the velocity law. At the base of the wind, the density is given by

$$\rho(r_0) = \frac{\dot{m}'(r_0)}{v_z(r_0)}. \quad (2.14)$$

At a coordinate (r, z) in the wind, the density is then

$$\rho(r, z) = \frac{r_0}{r} \frac{dr_0}{dr} \frac{\dot{m}'(r_0)}{v_z(r, z)} \quad (2.15)$$

where the corresponding r_0 is found by considering the streamline that passes through

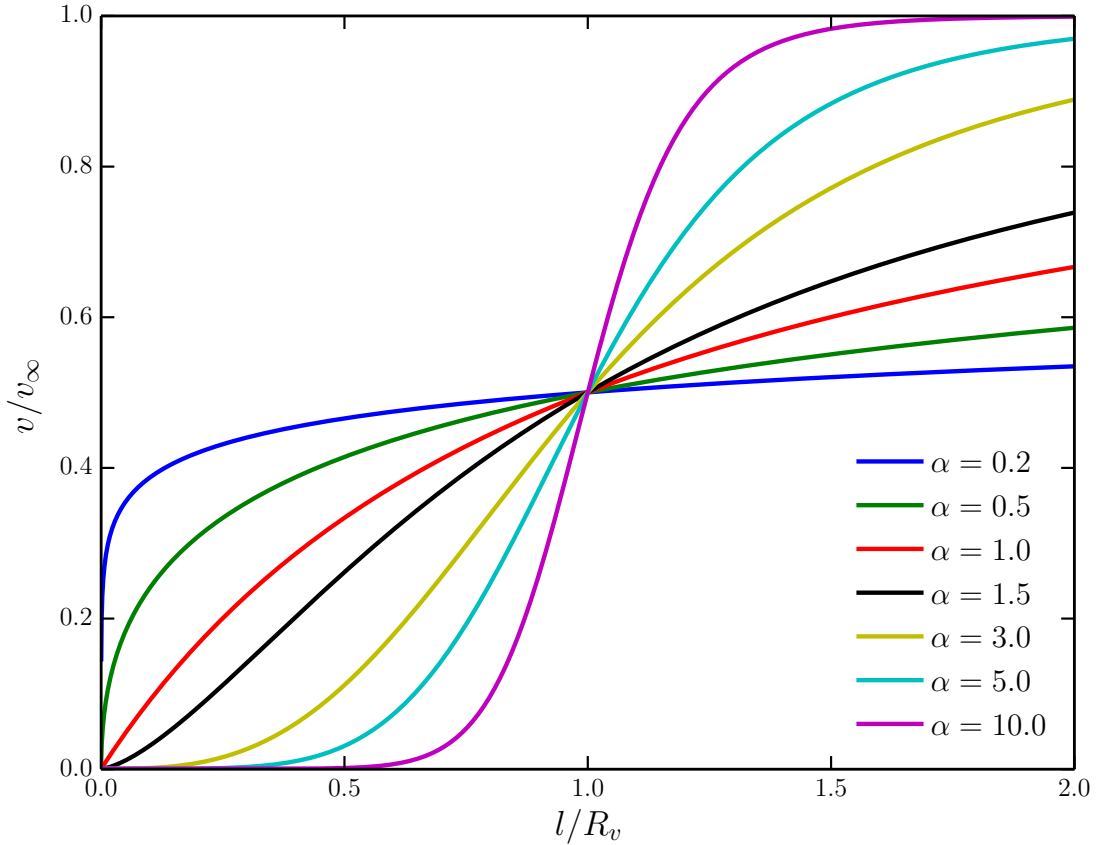


FIGURE 2.15: The SV93 velocity law for various values of the acceleration exponent, α .

(r, z) . These equations govern the kinematics and densities in the wind in the SV93 prescription, which is used extensively throughout this thesis.

2.5 The big picture: AGN Feedback

The event horizon of a $10^9 M_\odot$ BH is approximately 10^{15} cm, a billionth of the radius of a typical galactic bulge. This is roughly the ratio in size between a small coin and the Earth. Even the sphere of gravitational influence of the BH is roughly 1000 times smaller than the size of the galactic bulge. Despite this vast difference in scale, there is strong evidence that the physics on the scale of the gravitational radius of the BH affects the evolution and dynamics of its host galaxy. This becomes less surprising when considering the *energetics* of accretion. The binding energy of a galactic bulge, with mass M_{bulge} and velocity dispersion σ_* , is

$$E_{bulge} \approx M_{bulge} \sigma_*^2, \quad (2.16)$$

while the energy released in growing a black hole to a mass M'_{BH} is (equation 1.3, assuming $\eta = 0.1$)

$$E_{BH} \approx 0.1M'_{BH}c^2. \quad (2.17)$$

By combining these two equations, and substituting in typical numbers ($\sigma_* = 0.001c$, $M'_{BH}/M_{bulge} = 10^{-3}$), we can show that

$$\frac{E_{BH}}{E_{bulge}} \approx 10^{-4} \left(\frac{c}{\sigma_*} \right)^2 \sim 10. \quad (2.18)$$

In other words, the energy released when growing a BH can significantly exceed the binding energy of the galactic bulge. This energetic argument is, of course, not sufficient to claim that the accreting BH must affect its host. For example, if the radiated energy never experienced an optical depth of ~ 1 , it could not couple to the galactic bulge. However, we have already seen that many outflows in AGN possess kinetic luminosities that are significant compared to the bolometric luminosity. Thus, outflows (and jets) may provide a mechanism by which the vast accretion energies can be transferred to the BH environment.

2.5.1 Observational evidence for feedback

Perhaps the most famous pieces of evidence for some kind of long-distance relationship between a central BH and its host galaxy are the $M_{BH} - \sigma_*$ (Ferrarese & Merritt 2000; Gebhardt et al. 2000; Gultekin et al. 2009) and $M_{BH} - M_{bulge}$ (Magorrian et al. 1998; Häring & Rix 2004; McConnell & Ma 2013) correlations, shown in Fig. 2.16 and Fig. 2.17, respectively. By themselves, these correlations would not necessarily imply that the AGN is having an impact on its environment. Indeed, there are many different theoretical models for the origin of these relations (e.g Somerville et al. 2001; Adams et al. 2001; Burkert & Silk 2001; King 2003; Croton et al. 2006; Kormendy & Ho 2013). However, there are many other clues that outflows and jets from AGN can affect the host galaxy evolution and morphology.

The galaxy luminosity function describes the number of galaxies as a function of luminosity and is generally modelled with the Schechter (1976) function. Theories of galaxy evolution tend to overpredict the number of galaxies at the high luminosity end, which can be avoided by invoking quenching of star formation by the central AGN (e.g. Read

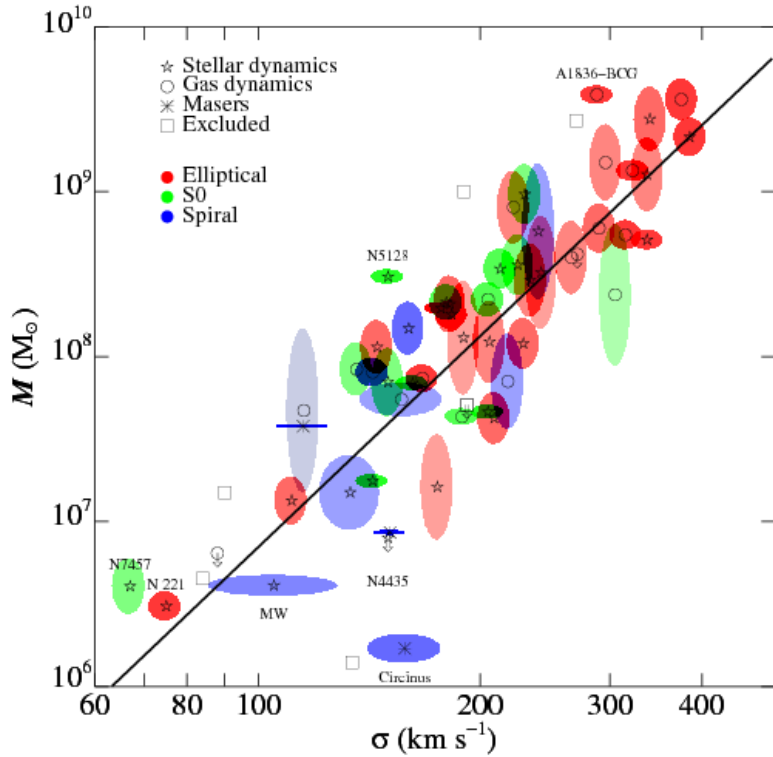


FIGURE 2.16: Credit: Gultekin et al. 2009. The $M_{BH} - \sigma_*$ correlation.

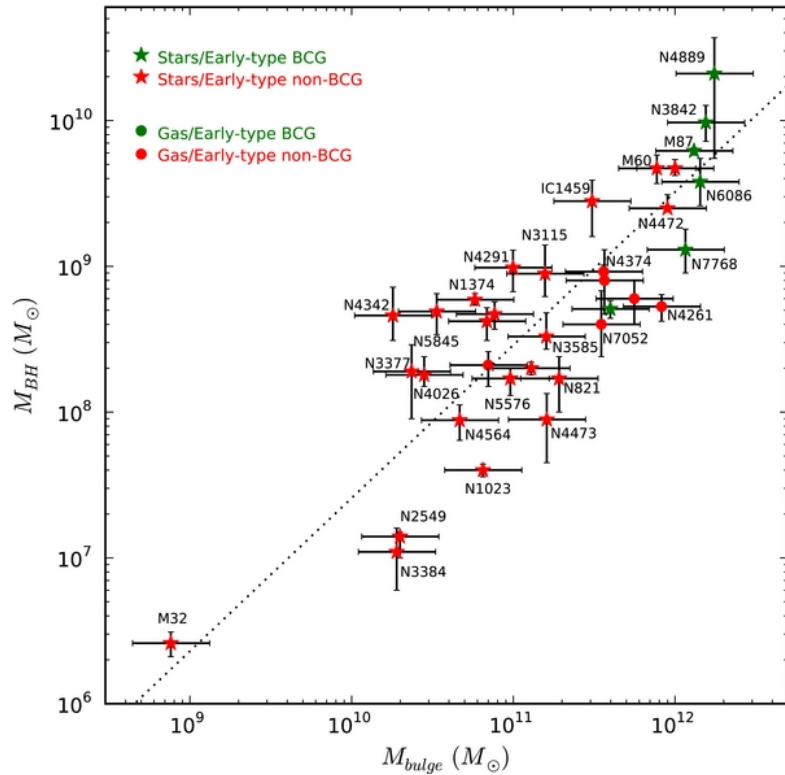


FIGURE 2.17: Credit: McConnell & Ma 2013. The $M_{BH} - M_{bulge}$ correlation.

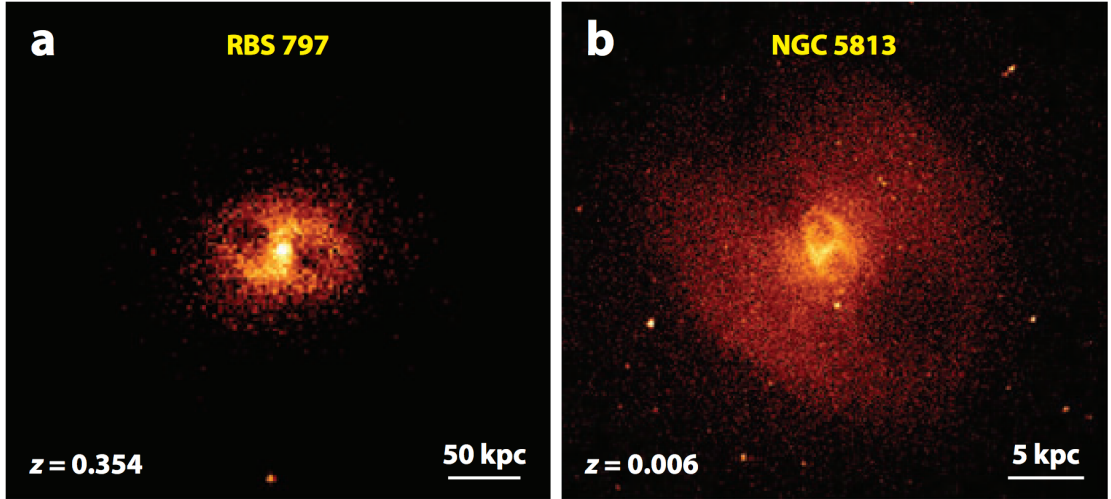


FIGURE 2.18: Figure adapted from Fabian 2012. Chandra X-ray images showing two examples of X-ray cavities, illustrating how a radio jet from an AGN can have a dramatic impact on its environment. a) The RBS 797 Cluster (Cavagnolo et al. 2011). b) elliptical galaxy NGC 5813 (Randall et al. 2011).

& Trentham 2005; Bongiorno et al. 2016). Galaxies also show bimodality in their colour distributions (Strateva et al. 2001; Bell et al. 2003; Baldry et al. 2004), with a clear separation between a blue, star-forming main sequence, and a red sequence with lower specific star formation rate (sSFR). Furthermore, these two sequences tend to lie in the same regions of colour space as the host galaxies of high and low Eddington fraction AGN respectively, implying that the AGN may be directly responsible for quenching the star formation and moving a galaxy onto the ‘red and dead’ branch. This has been demonstrated in several numerical simulations (e.g. Springel et al. 2005; Croton et al. 2006).

There is also evidence that AGN are energetically significant on scales larger than the galactic bulge. X-ray observations of cool core clusters and elliptical galaxies can show dramatic X-ray cavities or bubbles up to 50 kpc across, with a radio-loud AGN at the centre (Randall et al. 2011; Cavagnolo et al. 2011; Fabian 2012, Fig. 2.18). This shows how radio jets can significantly impact the surrounding gas, a flavour of feedback known as ‘radio’ or ‘kinetic’ mode. These cavities also provide an estimate of the kinetic power of a radio jet, as the volume of the bubble and surrounding gas pressure gives a rough estimate of the PV work done by the jet. This can be divided by an age estimate for the cavity, giving powers of up to $10^{46} \text{ erg s}^{-1}$, which are weakly correlated with the radio luminosity of the source, and can be large for modest radio power (Bîrzan et al. 2008).

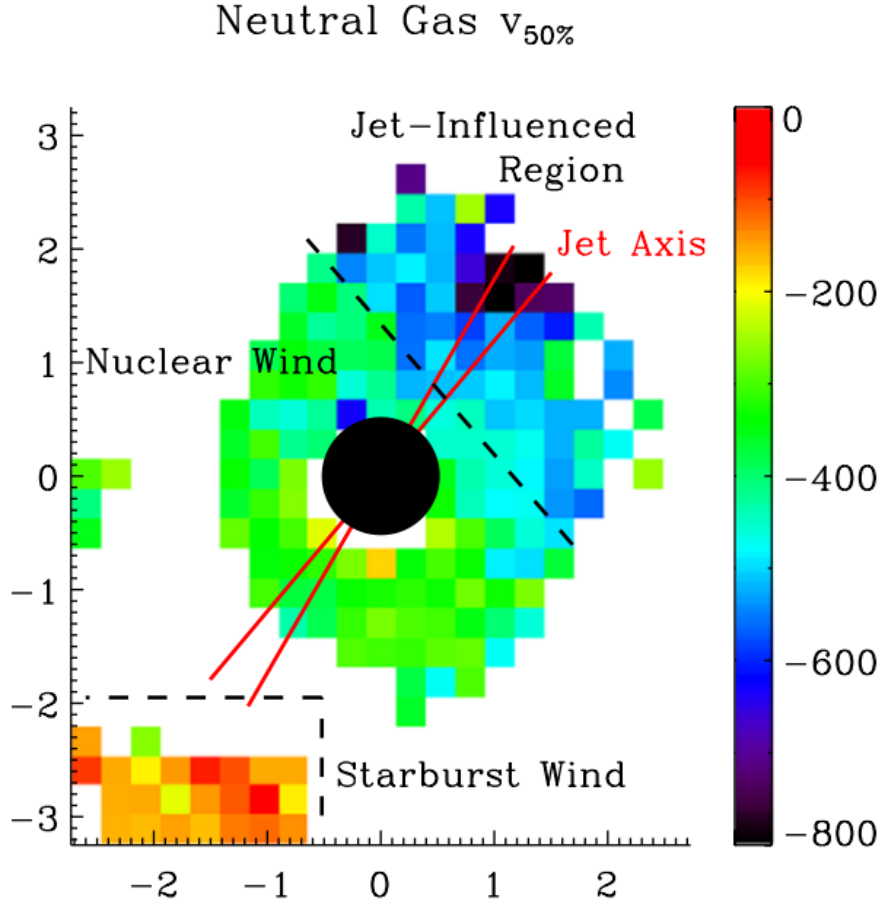


FIGURE 2.19: Credit: Rupke & Veilleux 2011. Results of Gaussian line profile fitting to integral field spectroscopy of Mrk 231. The quantity shown, $v_{50\%}$, corresponds to the centre of the fitted Gaussian profile and indicates that high outflow velocities are present in the neutral gas.

However, jets are not the only way for AGN to interact with their environment. I have already briefly discussed in section 2.1.3.3 how fast AGN winds can drive larger-scale molecular outflows. This can be seen spectacularly in the FeLoBALQSO Mrk231, where integrated field spectroscopy shows kiloparsec-scale neutral gas outflows (see Fig. 2.19; Rupke & Veilleux 2011). Furthermore, King (2003) expanded on the ideas of Silk & Rees (1998) and considered a super-Eddington, momentum-driven outflow expanding into the surrounding gas. This model naturally reproduces the observed slope of the $M_{BH} - \sigma_*$ relation. This line of argument was used to suggest that super-Eddington accretion must be common near the end of a quasar cycle, although it is worth noting that line-driving, or non-radiative driving, would mean that super-Eddington accretion rates are not required to drive such an outflow. Intriguingly, this means that understanding outflow physics has implications for the Soltan (1982) argument, SMBH spin and the accretion history of the Universe.

2.5.2 Alternative Explanations

It cannot yet be proven that AGN are the drivers of the observed galaxy colour evolution, high-end luminosity function discrepancy or BH-bulge correlations. In particular, it is also possible that mergers are responsible for these phenomena. For example, major galaxy mergers may explain the ‘red and dead’ branch of the galaxy colour bimodality (e.g. [Somerville et al. 2001](#); [Baldry et al. 2004](#)). However, AGN winds and jets are clearly energetically significant with respect to their host galaxies, so estimating their kinetic powers accurately is important in discriminating between in-situ and ex-situ scenarios.

Having established the astrophysical importance of outflows, I will now move on to discussing how we might go about accurately modelling the ionization states of accretion disc winds, and their emergent spectra.

Chapter 3

Testing Quasar Unification: Radiative Transfer In Clumpy Winds

This chapter is based on the publication:

Matthews J. H., Knigge C., Long K. S., Sim S. A., Higginbottom N., Mangham S. W., ‘Testing quasar unification: radiative transfer in clumpy winds’, 2016, MNRAS, 458, 293.

3.1 Introduction

In the earlier chapters I presented the evidence for accretion disc winds in quasars and luminous AGN, and showed how they may be responsible for more than just the broad absorption lines and P-Cygni profiles seen in quasar spectra. In particular, they offer a natural way to *unify* much of the complex phenomenology into one simple picture.

Here, I aim to test that picture using PYTHON, with the specific aim of determining whether it is possible to simulate the properties of the spectra of AGN, including BALQSOs, using simple kinematic prescriptions for biconical disc winds. Past results have been encouraging; H13 produced simulated spectra that resembled that of BALQSOs, as long as the luminosity of the X-ray source was relatively low, of order 10^{43} erg s⁻¹

and the mass loss rate was relatively high, of order the mass accretion rate. However, at higher X-ray luminosities, the wind was so ionized that UV absorption lines were not produced. In addition, and in part due to limitations in our radiative transfer code, the model failed to produce spectra with strong emission lines at any inclination angle.

Here I attempt to address both of these issues, by introducing clumping into PYTHON and a more complete treatment of H and He into the radiative transfer calculations. Thus, the simulations presented in this chapter treat H & He as full macro-atoms, and model metals as simple-atoms as described extensively in chapter 3. In order to correctly model the ionizing spectrum for simple-atoms I dispense with the ML93 modified Saha approach and fully solve the ionization balance using the spectral modelling approach described in section ???. Macro-atoms still have their ionization and excitation states calculated from MC estimators.

The kinematic model used once again follows the SV93 prescription, and is described, together with the clumping implementation, in section 3.2. Section 3.3 contains the results from a clumped model, with comparisons to observational data, as well as some discussion. Further discussion and examination of sensitivity to model parameters and viewing angle can be found in section 3.4, which expands somewhat on the work presented in (Matthews et al. 2016). Finally, I summarise the findings in section 3.5.

3.2 A Clumpy Biconical Disk Wind Model for Quasars

Here, I once again adopt the SV93 kinematic prescription for a biconical disc wind model described in section 2.4 LK02, H13 and M15. A schematic is shown in Fig. 4.4, with key aspects marked. The general biconical geometry is similar to that invoked by Murray et al. (1995) and Elvis (2000) to explain the phenomenology of quasars and BALQSOs.

3.2.1 Photon Sources

Two sources of r-packets are included in the model: An accretion disc and a central X-ray source. The accretion disc is assumed to be geometrically thin, but optically thick. Accordingly, the disc is modelled as an ensemble of blackbodies with a Shakura

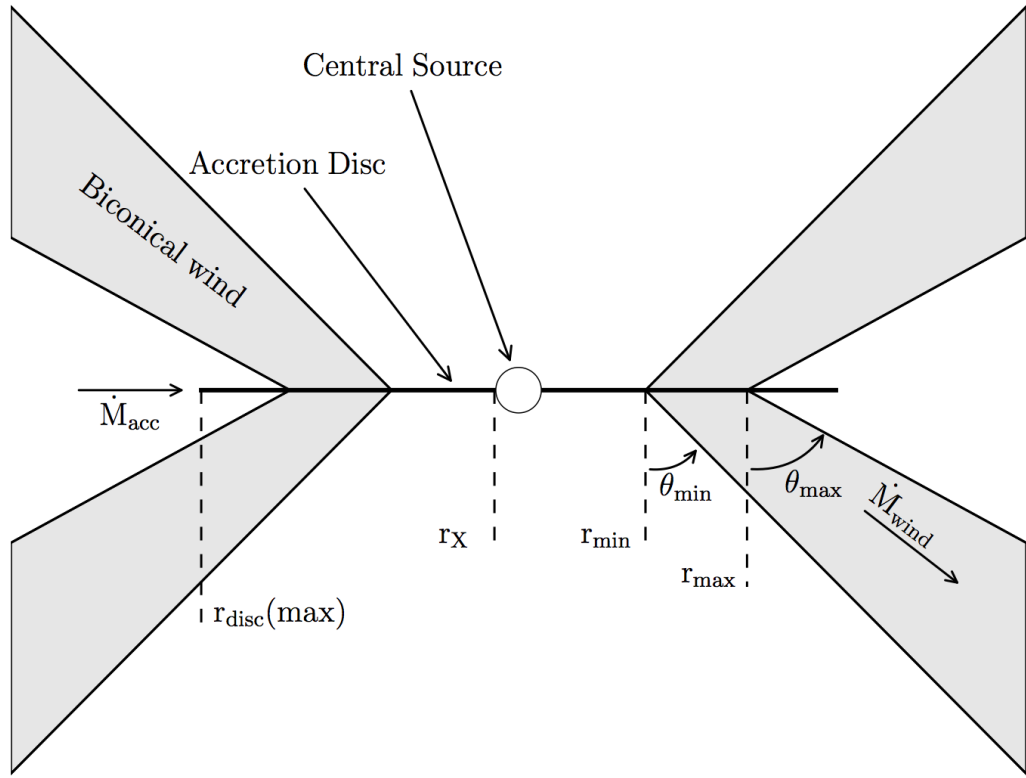


FIGURE 3.1: A cartoon showing the geometry and some key parameters of our biconical wind model.

& Sunyaev (1973) effective temperature profile. The emergent SED is then determined by the specified accretion rate (\dot{m}) and central BH mass (M_{BH}). All photon sources in our model are opaque, meaning that r -packets that strike them are destroyed. The inner radius of the disc extends to the innermost stable circular orbit (ISCO) of the BH. I assume a Schwarzschild BH with an ISCO at $6 r_G$, where $r_G = GM_{BH}/c^2$ is the gravitational radius. For a $10^9 M_\odot$ BH, this is equal to 8.85×10^{14} cm or $\sim 10^{-4}$ pc.

The X-ray source is treated as an isotropic sphere at the ISCO, which emits r -packets according to a power law in flux with index α_X , of the form

$$F_X(\nu) = K_X \nu^{\alpha_X}. \quad (3.1)$$

The normalisation, K_X of this power law is such that it produces the specified 2-10 keV luminosity, L_X . The input spectrum for our simulations is therefore a simple combination of a power law X-ray component and accretion disc spectrum; an example input spectrum is shown in Fig. 3.2. In actual fact, this spectrum will be angle dependent

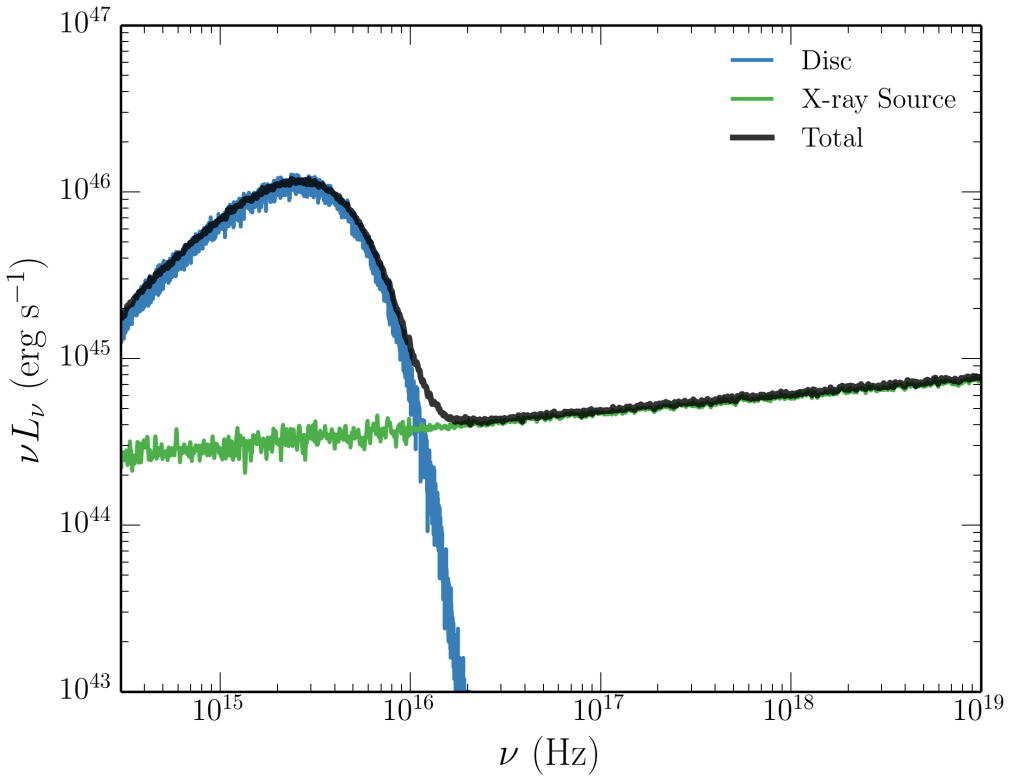


FIGURE 3.2: The input spectrum used for our quasar modelling.

due to the geometry of the system and the angular emissivity profile of the accretion disc (see sections 3.3.3 and 3.4.2). Photons, or r -packets, produced by the accretion disc and central X-ray source are reprocessed by the wind. This reprocessing is dealt with by enforcing strict radiative equilibrium (*modulo* adiabatic cooling; see section 2.3) via an indivisible energy packet constraint (see Lucy 2002, M15).

3.2.2 A Simple Approximation for Clumping

In previous modelling efforts with PYTHON, a smooth outflow was assumed, such that the density at a given point was determined only by the kinematic parameters and mass loss rate. However, as already discussed, AGN winds exhibit significant substructure – the outflow is expected to be *clumpy*, rather than smooth, and probably on a variety of scales. A clumpy outflow offers a possible solution to the so-called ‘over-ionization problem’ in quasar and AGN outflows (e.g. ??Hamann et al. 2013). This is the main motivation for incorporating clumping into our model.

Deciding on how to implement clumping into our existing wind models was not straightforward. First, and most importantly, the physical scale lengths and density contrasts in AGN outflows are not well-constrained from observations or theory. As a result, while one could envision in principle, clouds with a variety of sizes and density contrasts varying perhaps as function of radius, there would have been very little guidance on how to set nominal values of the various parameters of such a model. Second, there are significant computational difficulties associated with adequately resolving and realistically modelling a series of small scale, high density regions with a MCRT – or for that matter, a hydrodynamical – code. Given the lack of knowledge about the actual type of clumping, I have implemented a simple approximation used successfully in stellar wind modelling, known as *microclumping* (e.g. Hamann & Koesterke 1998; Hillier & Miller 1999; Hamann et al. 2008).

The underlying assumption of microclumping is that clump sizes are much smaller than the typical photon mean free path, and thus the clumps are both geometrically and optically thin. This approach allows one to treat clumps only in terms of their volume filling factor, f_V , instead of having to specify separately their size and density distributions. In our model, f_V is independent of position (see section 4.4). The inter-clump medium is modeled as a vacuum, although the outflow is still non-porous and axisymmetric. This approach therefore assumes that the inter-clump medium is unimportant in determining the output spectrum, which is expected to be true only when density constraints are large and the inter-clump medium is both very ionized and of low emissivity and opacity. The density of the clumps is multiplied by the “density enhancement” $D = 1/f_V$. Opacities, κ , and emissivities, ϵ , can then be expressed as

$$\kappa = f_V \kappa_C(D); \quad \epsilon = f_V \epsilon_C(D). \quad (3.2)$$

Here the subscript C denotes that the quantity is calculated using the enhanced density in the clump. The resultant effect is that, *for fixed temperature*, processes that are linear in density, such as electron scattering, are unchanged, as f_V and D will cancel out. However, any quantity that scales with the square of density, such as collisional excitation or recombination, will increase by a factor of D . In our models, the temperature is not fixed, and is instead set by balancing heating and cooling in a given cell. In the presence of an X-ray source, this thermal balance is generally dominated by bound-free heating and line cooling. The main effect of including clumping in our modelling is that it

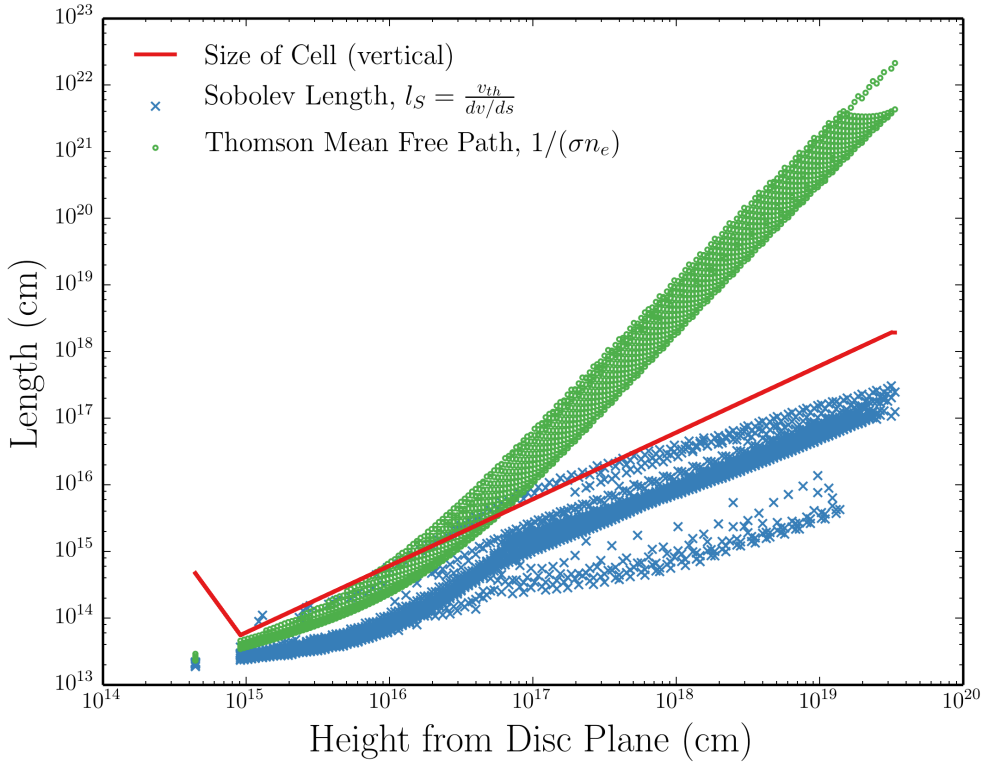


FIGURE 3.3: Some typical length scales for the fiducial model. This places a formal limit of $\sim 10^{12}$ cm on clump sizes in the microclumping framework, and confirms that the cells are sufficiently larger than the Sobolev length in almost all cases.

moderates the ionization state due to the increased density. This allows an increase in the ionizing luminosity, amplifying the amount of bound-free heating and also increasing the competing line cooling term (thermal line emission).

The shortest length scale in a Sobolev MCRT treatment such as ours is normally the Sobolev length, given by

$$l_S = \frac{v_{th}}{|dv/ds|} \quad (3.3)$$

This is typically $\sim 10^{13}$ cm near the disc plane, increasing outwards. The Sobolev length is shown, together with the size of the cell and Thomson mean free path, in Fig. 3.3. The mean density is used to calculate the Sobolev optical depth, which assumes that l_S is greater than the typical clump size. Thus for the microclumping assumption to be formally correct, clumps should be no larger than $\sim 10^{12}$ cm. This size scale is not unreasonable for quasar outflows, as [de Kool & Begelman \(1995\)](#) suggest that BAL flows may have low filling factors with clump sizes of $\sim 10^{11}$ cm.

Our clumping treatment is necessarily simple; it does not adequately represent the complex substructures and stratifications in ionization state expected in AGN outflows. Nevertheless, this parameterization allows simple estimates of the effect clumping has on the ionization state and emergent line emission.

3.2.3 The Simulation Grid

Using this prescription, I conducted a limited parameter search over a 5-dimensional parameter space involving the variables r_{min} , θ_{min} , f_V , α and R_v . The grid points are shown in Table 1. The aim here was to first fix M_{BH} and \dot{m} to their H13 values, and increase L_X to 10^{45} erg s $^{-1}$ (a more realistic value for a quasar of $10^9 M_\odot$ and an Eddington fraction of 0.2; see section 3.3.3).

These models were then evaluated based on how closely their synthetic spectra reproduced the following properties of quasars and BALQSOs:

- UV absorption lines with $BI > 0$ at $\sim 20\%$ of viewing angles (e.g. Knigge et al. 2010);
- Line emission emerging at low inclinations, with $EW \sim 40\text{\AA}$ in C IV 1550\AA (e.g. Shen et al. 2011);
- H recombination lines with $EW \sim 50\text{\AA}$ in Ly α (e.g. Shen et al. 2011);
- Mg II and Al III (LoBAL) absorption features with $BI > 0$ at a subset of BAL viewing angles;
- Verisimilitude with quasar composite spectra.

Here BI is the ‘Balnicity Index’ (Weymann et al. 1991), given by

$$BI = \int_{3000 \text{ km s}^{-1}}^{25000 \text{ km s}^{-1}} C \left(1 - \frac{f(v)}{0.9} \right) dv. \quad (3.4)$$

The constant $C = 0$ everywhere, unless the normalized flux has satisfied $f(v) < 0.9$ continuously for at least 2000 km s 1 , whereby C is set to 1.

In the next section, I present one of the most promising models, which I refer to as the fiducial model, and discuss the various successes and failures with respect to the

| Parameter | Grid Point Values | | |
|----------------|--------------------|--------------------|----------|
| r_{min} | $60r_g$ | $180r_g$ | $300r_g$ |
| θ_{min} | 55° | 70° | |
| R_v | 10^{18}cm | 10^{19}cm | |
| α | 0.5 | 0.6 | 0.75 |
| f_V | 0.01 | 0.1 | 1.5 |

TABLE 3.1: The grid points used in the parameter search. The sensitivity to some of these parameters is discussed further in section 3.4.1

above criteria. This allows us to gain insight into fundamental geometrical and physical constraints and assess the potential for unification. I then discuss the sensitivity to key parameters in section 3.4.1. The full grid, including output synthetic spectra and plots can be found at jhmatthews.github.io/quasar-wind-grid/.

3.3 Results and Analysis From A Fiducial Model

Here I describe the results from a fiducial model, and discuss these results in the context of the criteria presented in section 3.4. The parameters of this model are shown in Table 2. Parameters differing from the benchmark model of H13 are highlighted with an asterisk. In this section, I examine the physical conditions of the flow, and present the synthetic spectra, before comparing the X-ray properties of this particular model to samples of quasars and luminous AGN.

3.3.1 Physical Conditions and Ionization State

Fig. 3.4 shows the physical properties of the wind. The wind rises slowly from the disc at first, with densities within clumps of $n_H \sim 10^{11} \text{ cm}^{-3}$ close to the disc plane, where n_H is the local number density of H. To illustrate the degree of scale and density ranges in the model I also show n_e in the wind on a linear scale in Fig. 3.5. The flow then accelerates over a scale length of $R_V = 10^{19} \text{ cm}$ up to a terminal velocity equal to the escape velocity at the streamline base ($\sim 10,000 \text{ km s}^{-1}$). This gradual acceleration results in a wind that exhibits a stratified ionization structure, with low ionization material in the base of the wind giving way to highly ionized plasma further out. This is illustrated in Fig. 3.4 by the panels showing the ion fraction $F = n_j/n_{tot}$ of some important ions. The clumped wind produces the range of ionization states observed

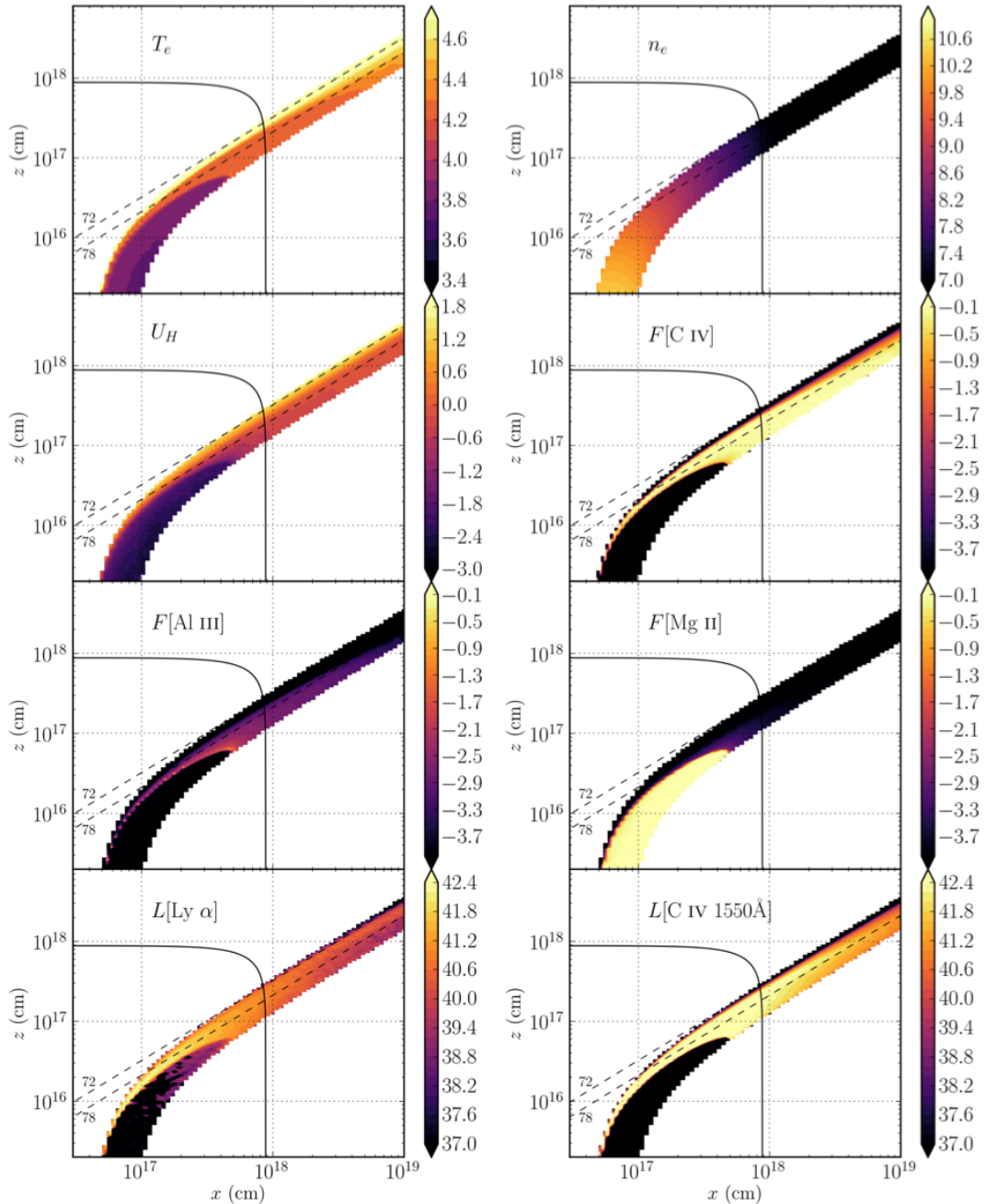


FIGURE 3.4: Contour plots showing the logarithm of some important physical properties of the outflow. The spatial scales are logarithmic and the x and z scales are not the same. Symbols are defined in the text. The solid black line marks a sphere at $1000 r_G$. The dotted lines show the 72° and 78° sightlines to the centre of the system, and illustrate that different sightlines intersect material of different ionization states. The line luminosities, L , represent the luminosity of photons escaping the Sobolev region for each line. These photons do not necessarily escape to infinity.

| Fiducial Parameters | Model | Value |
|------------------------|-------|--|
| M_{BH} | | $1 \times 10^9 M_\odot$ |
| \dot{m}_{acc} | | $5 M_\odot yr^{-1} \simeq 0.2 \dot{M}_{Edd}$ |
| α_X | | -0.9 |
| L_X | | $10^{45} \text{ erg s}^{-1}$ |
| $r_{disc}(\min) = r_X$ | | $6r_g = 8.8 \times 10^{14} \text{ cm}$ |
| $r_{disc}(\max)$ | | $3400r_g = 5 \times 10^{17} \text{ cm}$ |
| \dot{m}_{wind} | | $5 M_\odot yr^{-1}$ |
| r_{min} | | $300r_g = 4.4 \times 10^{16} \text{ cm}$ |
| r_{max} | | $600r_g = 8.8 \times 10^{16} \text{ cm}$ |
| θ_{min} | | 70.0° |
| θ_{max} | | 82.0° |
| $v_\infty(r_0)$ | | $v_{esc}(r_0)$ |
| R_v | | 10^{19} cm^* |
| α | | 0.5* |
| f_V | | 0.01* |
| n_x | | 100 |
| n_z | | 200 |

TABLE 3.2: Wind geometry parameters used in the fiducial model, as defined in the text and figure 1. Parameters differing from the benchmark model of H13 are highlighted with an asterisk.

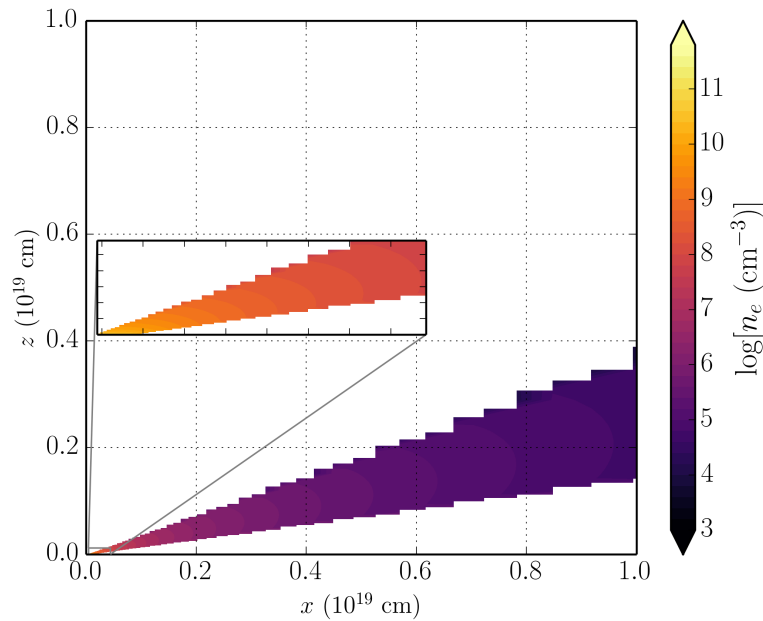


FIGURE 3.5: The electron density in the model, this time on linear axes in order to illustrate the density contrasts and scale of the system. The plot is on the scale of the acceleration length, whereas the inset is a box of $2700 \times 800r_G$, where the bottom left corner corresponds to the base of the innermost streamline.

in quasars and BALQSOs, while adopting a realistic $2 - 10$ keV X-ray luminosity of $L_X = 10^{45}$ erg s $^{-1}$. Without clumping, this wind would be over-ionized to the extent that opacities in e.g., C IV would be entirely negligible (see H13).

One common way to quantify the ionization state of a plasma is through the ionization parameter, U_H , given by equation ???. Shown in Fig. 3.4, the ionization parameter is a useful measure of the global ionization state, as it represents the ratio of the number density of H ionizing photons to the local H density. It is, however, a poor representation of the ionization state of species such as C IV as it encodes no information about the shape of the SED. In our case, the X-ray photons are dominant in the photoionization of the UV resonance line ions. This explains why a factor of 100 increase in X-ray luminosity requires a clumping factor of 0.01, even though the value of U_H decreases by only a factor of ~ 10 compared to H13.

The total line luminosity also increases dramatically compared to the unclumped model described by H13. This is because the denser outflow can absorb the increased X-ray luminosity without becoming over-ionized, leading to a hot plasma which produces strong collisionally excited line emission. This line emission typically emerges on the edge of the wind nearest the central source. The location of the line emitting regions is dependent on the ionization state, as well as the incident X-rays. The radii of these emitting regions is important, and can be compared to observations. The line luminosities, L , shown in the figure correspond to the luminosity in erg s $^{-1}$ of photons escaping the Sobolev region for each line. As shown in Fig. 3.4, the C IV 1550Å line in the fiducial model is typically formed between $100 - 1000 r_G$ ($\sim 10^{17} - 10^{18}$ cm). This is in rough agreement with the reverberation mapping results of Kaspi et al. (2007) for the $2.6 \times 10^9 M_\odot$ quasar S5 0836+71, and also compares favourably with microlensing measurements of the size of the C IV 1550Å emission line region in the BALQSO H1413+117 (O'Dowd et al. 2015).

3.3.2 Synthetic Spectra: Comparison to Observations

Fig. 3.6 shows the synthetic spectrum in the UV from the fiducial model. To assess the ability of the synthetic spectra to match real quasar spectra, I also show *Sloan Digital Sky Survey* (SDSS) quasar composites from Reichard et al. (2003), normalised to the flux at 2000Å for low inclinations. Unfortunately, the wide variety of line profile shapes and internal trough structure in BALQSOs tends to ‘wash out’ BAL troughs in composite

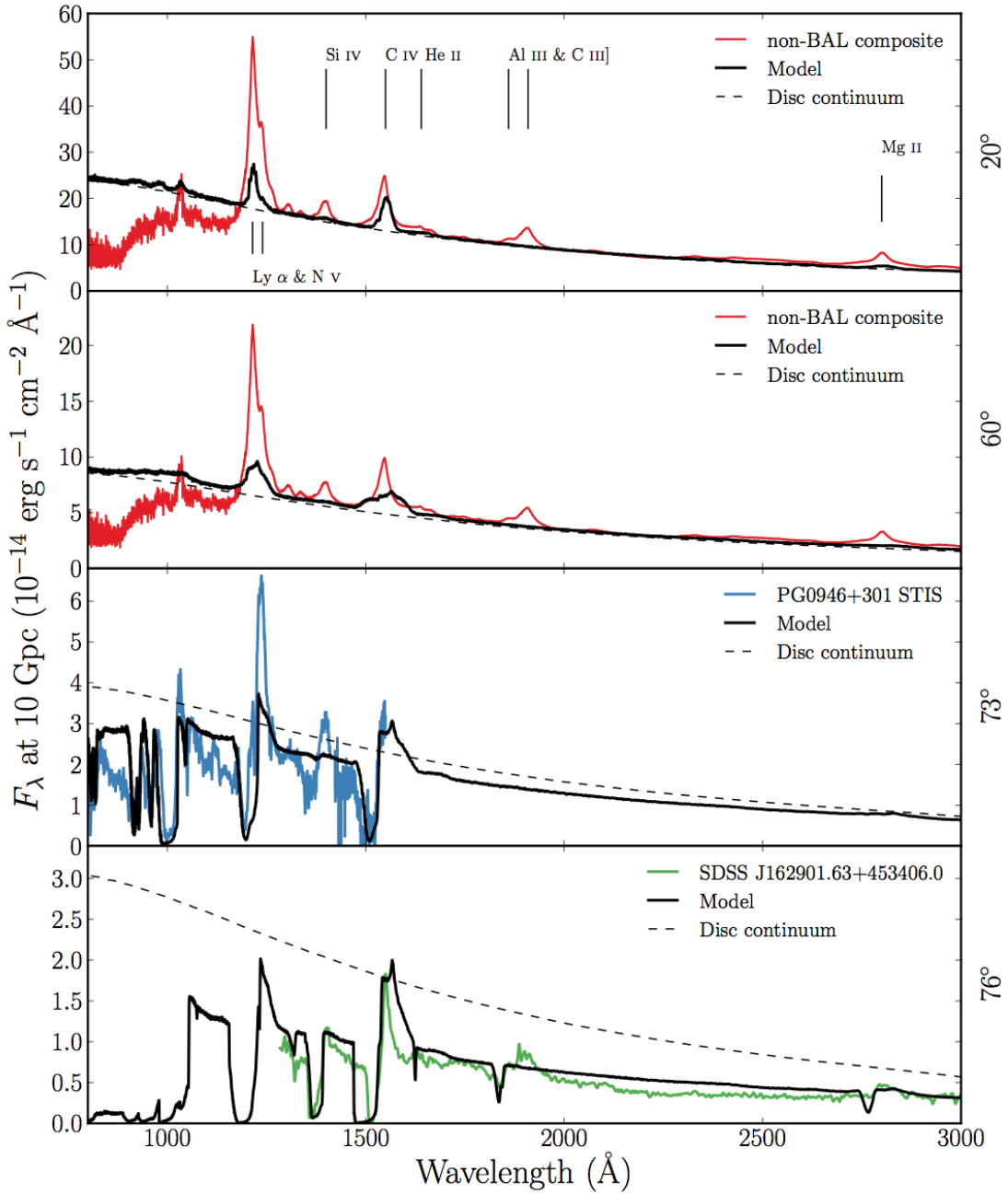


FIGURE 3.6: Synthetic spectra at four viewing angles for the fiducial model. At 20° and 60° I show a comparison to an SDSS quasar composite from Recihard et al. (2003). At 73° and 76° I show a comparison to an *HST* STIS spectrum of the high BALnicity BALQSO PG0946+301 (Arav et al. 2000), and an SDSS spectrum of the LoBAL quasar SDSS J162901.63+453406.0, respectively. The dotted line shows a disc only continuum to show the effect of the outflow on the continuum level. All the spectra are scaled to the model flux at 2000\AA , except for the *HST* STIS spectrum of PG0946+301, which is scaled to 1350\AA due to the incomplete wavelength coverage.

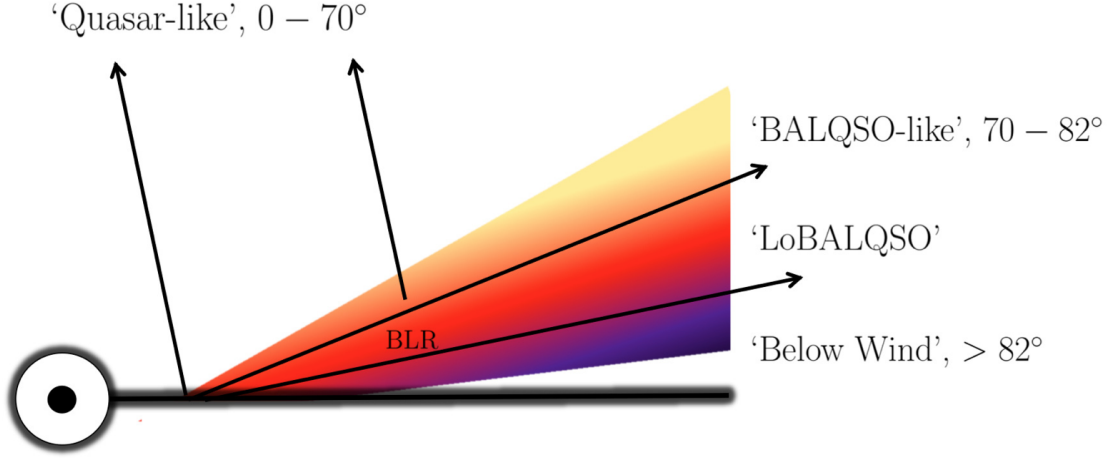


FIGURE 3.7: A cartoon describing the broad classes of sightline in the fiducial model, illustrating how geometric effects lead to the different emergent spectra. The colour gradient is approximate, but indicates the stratified ionization structure, from highly ionized (yellow) to low ionization (purple) material.

spectra to the extent that BALQSO composites do not resemble typical BALQSOs. Because of this, I instead compare to a *Hubble Space Telescope* STIS spectrum of the high BALnicity BALQSO PG0946+301 (Arav et al. 2000), and an SDSS spectrum of the LoBAL quasar SDSS J162901.63+453406.0, for the angles of 73° and 76° , respectively. A cartoon illustrating how geometric effects determine the output spectra is shown in Fig. 3.7.

3.3.2.1 Broad absorption lines ('BALQSO-like' angles)

The UV spectrum is characterised by strong BAL profiles at high inclinations ($> 70^\circ$). This highlights the first success of our model: clumping allows the correct ionization state to be maintained in the presence of strong X-rays, resulting in large resonance line opacities. At the highest inclinations, the cooler, low ionization material at the base of the wind starts to intersect the line of sight. This produces multiple absorption lines in species such as Mg II, Al III and Fe II. The potential links to LoBALQSOs and FeLoBALQSOs are discussed in section 2.4.

The high ionization BAL profiles are often saturated, and the location in velocity space of the strongest absorption in the profile varies with inclination. At the lowest inclination BAL sight lines, the strongest absorption occurs at the red edge, whereas at higher

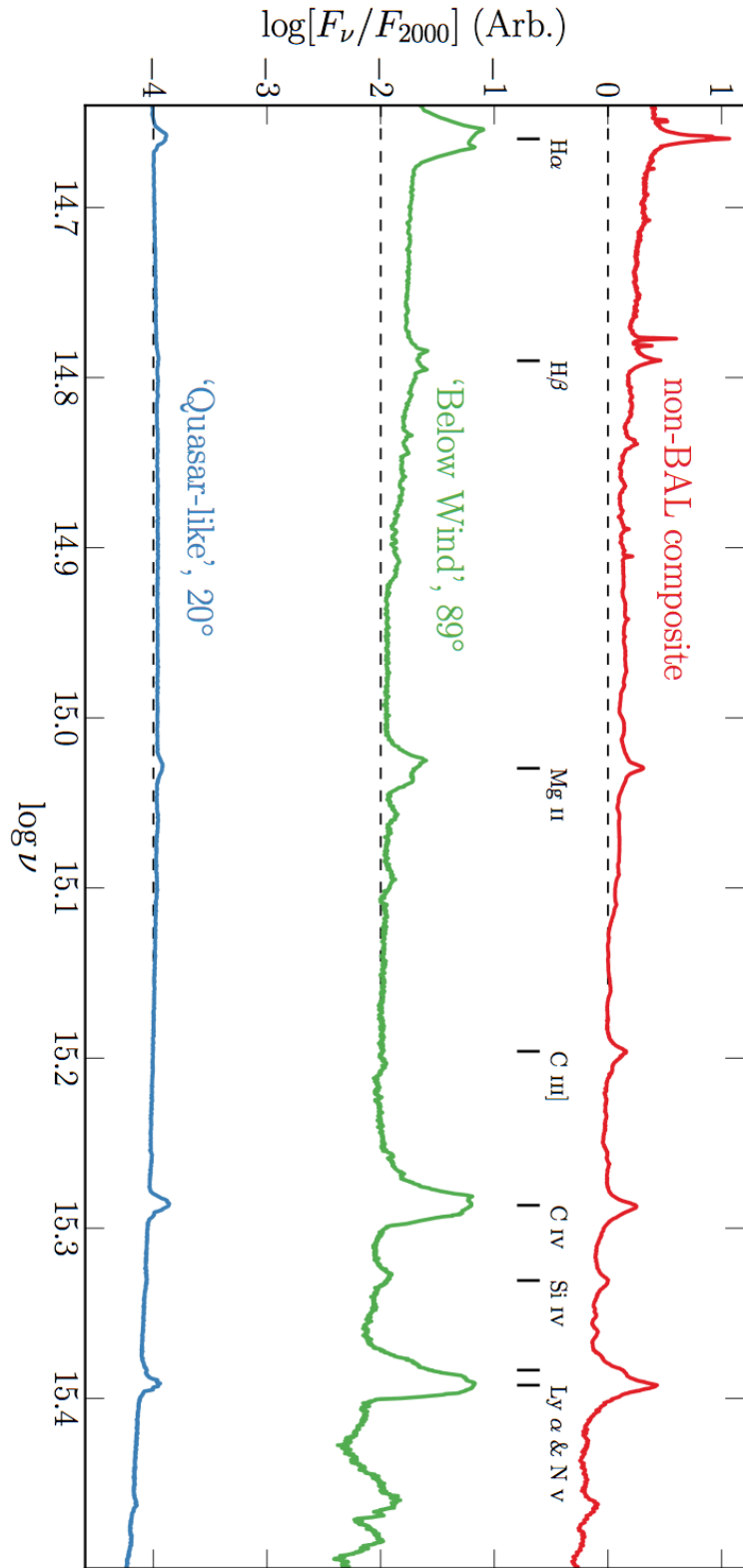


FIGURE 3.8: Synthetic spectra at two viewing angles, this time in frequency space and including the optical band, compared to the non-BAL SDSS quasar composite. The spectra are normalised to the flux at 2000Å, then an offset of 2 is applied per spectrum for clarity – the dotted lines show the zero point of F_ν/F_{2000} in each case.

| Property | Synthetic, 20° | Observed (S11) |
|--------------------------|-------------------|------------------|
| $\log L[\text{C IV}]$ | 44.60 | 44.42 ± 0.32 |
| $\log L[\text{Mg II}]$ | 43.92 | 43.54 ± 0.28 |
| $\log(\nu L_\nu)_{1350}$ | 46.42 | 46.01 ± 0.30 |
| $\log(\nu L_\nu)_{3000}$ | 46.18 | 45.79 ± 0.30 |

TABLE 3.3: Some derived spectral properties of the fiducial model, at 20°, compared to observations. The observed values are taken from the Shen et al. (2011) SDSS DR7 Quasar catalog, and correspond to mean values with standard deviations in log space from a subsample with $8.5 > \log(M_{BH}) < 9.5$ and $1.5 < \log(L_{bol}/L_{Edd}) < 0$, where the BH mass is a C IV virial estimate. Units are logarithms of values in erg s⁻¹.

inclinations (and for the strongest BALs) the trough has a sharp edge at the terminal velocity. This offers one potential explanation for the wide range of BALQSO absorption line shapes (see e.g. [Trump et al. 2006](#); [Knigge et al. 2008](#); [Filiz Ak et al. 2014](#)).

The absorption profiles seen in BALQSOs are often non-black, but saturated, with flat bases to the absorption troughs ([Arav et al. 1999a,b](#)). This is usually explained either as partial covering of the continuum source or by scattered contributions to the BAL troughs, necessarily from an opacity source not co-spatial with the BAL forming region. The scattered light explanation is supported by spectropolarimetry results ([Lamy & Hutsemékers 2000](#)). Our spectra do not show non-black, saturated profiles. Black, saturated troughs are seen at angles $i > 73^\circ$, and the BALs are non-saturated at lower inclinations. The reasons for this are inherent in the construction of our model. First, the microclumping assumption does not allow for porosity in the wind, meaning that it does not naturally produce a partial covering absorber. To allow this, an alternative approach such as *macroclumping* would be required (e.g. [Hamann et al. 2008](#); [Šurlan et al. 2012](#)). Second, our wind does not have a significant scattering contribution along sightlines which do not pass through the BAL region, meaning that any scattered component to the BAL troughs is absorbed by line opacity. This suggests that either the scattering cross-section of the wind must be increased (with higher mass loss rates or covering factors), or that an additional source of electron opacity is required, potentially in a polar direction above the disc. I note the scattering contribution from plasma in polar regions is significant in some ‘outflow-from-inflow’ simulations ([Kurosawa & Proga 2009](#); [Sim et al. 2012](#)).

3.3.2.2 Broad emission lines ('quasar-like' angles)

Unlike H13, significant collisionally excited line emission now emerges at low inclinations in the synthetic spectra, particular in the C IV and N V lines. Strong Ly α and weak He II 1640Å lines are also observed as a result of the improved treatment of recombination using macro-atoms. In the context of unification, this is a promising result, and shows that a biconical wind can produce significant emission at 'quasar-like' angles. To demonstrate this further, I show line luminosities and monochromatic continuum luminosities from the synthetic spectra in Table 3.3. These are compared to mean values from a subsample of the SDSS DR7 quasar catalog (Shen et al. 2011) with BH mass and Eddington fraction estimates similar to the fiducial model values (see caption). The spectra do not contain the strong C III] 1909Å line seen in the quasar composite spectra, but this is due to a limitation of our current treatment of C; semi-forbidden (intercombination) lines are not included in our modelling.

In Fig. 3.8, I show an F_ν spectrum with broader waveband coverage that includes the optical, showing that our synthetic spectra also exhibit H α and H β emission. In this panel, I include a low inclination and also a very high inclination spectrum, which looks underneath the wind cone. This model shows strong line emission with very similar widths and line ratios to the quasar composites, and the Balmer lines are double peaked, due to velocity projection effects. Such double-peaked lines are seen in so-called 'disc emitter' systems (e.g. Eracleous & Halpern 1994) but not the majority of AGN. The line equivalent widths (EWs) increase at high inclination due to a weakened continuum from wind attenuation, disc foreshortening and limb darkening. This effect also leads to a redder continuum slope, as seen in quasars, which is due to Balmer continuum and Balmer and Fe II line emission. This extreme 89° viewing angle cannot represent a typical quasar within a unified model, but does show that a model such as this can naturally reproduce quasar emission lines if the emissivity of the wind is increased *with respect to the disc continuum*. In addition, it neatly demonstrates how a stratified outflow can naturally reproduce the range of ionization states seen in quasars.

Despite a number of successes, there are some properties of the synthetic spectra that are at odds with the observations. First, the ratios of the EW of the Ly α and Mg II 2800Å lines to the EW of C IV 1550Å are much lower than in the composite spectra. Similar problems have also been seen in simpler photoionization models for

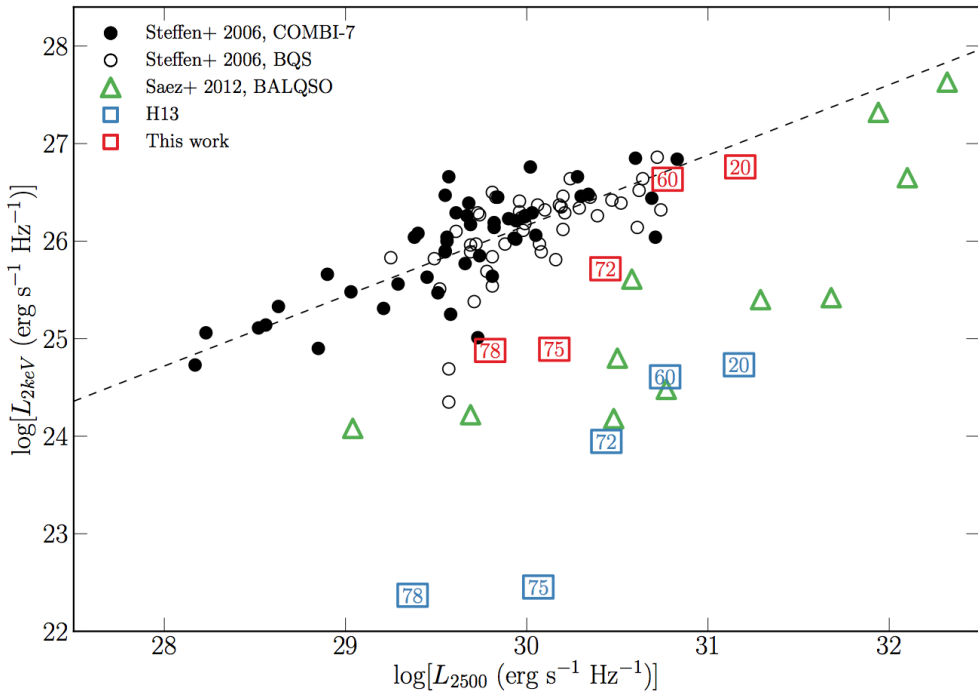


FIGURE 3.9: X-ray (2 keV) luminosity of the our clumped model (red squares) and the H13 model (blue squares), plotted against monochromatic luminosity at 2500Å. The points are labeled according to inclination; angles $> 70^\circ$ correspond to BALs in our scheme (see figure 4). Also plotted are measurements from the COMBI-7 AGN and the BQS samples (Steffen et al. 2006) and the Saez et al. (2012) sample of BALQSOs. The dotted line shows the best fit relation for non-BALQSOs from Steffen et al. (2006).

the BLR (Netzer 1990). It may be that a larger region of very dense ($n_e \sim 10^{10} \text{ cm}^{-3}$) material is needed, which could correspond to a disc atmosphere or ‘transition region’ (see e.g. Murray et al. 1995; Knigge et al. 1998a). While modest changes to geometry may permit this, the initial grid search did not find a parameter space in which the Ly α or Mg II EWs were significantly higher (see section 3.4.1). Second, EWs increase with inclination (see Fig. 3.6 and Fig. 3.8; also Fig. 3.10). This is discussed further in section 3.4.2.

3.3.3 X-ray Properties

The main motivation for adding clumping to the model was to avoid over-ionization of the wind in the presence of strong X-rays. Having verified that strong BALs appear in the synthetic spectra, it is also important to assess whether the X-ray properties of this fiducial model agree well with quasar and BALQSO samples for the relevant inclinations.

Fig. 3.9 shows the emergent monochromatic luminosity (L_ν) at 2 keV and plotted against L_ν at 2500Å for a number of different viewing angles in our model. The monochromatic luminosities are calculated from the synthetic spectra and thus include the effects of wind reprocessing and attenuation. In addition to model outputs, I also show the BALQSO sample of Saez et al. (2012) and luminous AGN and quasar samples from Steffen et al. (2006). The best fit relation from Steffen et al. (2006) is also shown. For low inclination, ‘quasar-like’ viewing angles, the model properties are in excellent agreement with AGN samples. The slight gradient from 20° to 60° in the models is caused by a combination of disc foreshortening and limb-darkening (resulting in a lower L_{2500} for higher inclinations), and the fact that the disk is opaque, and thus the X-ray source subtends a smaller solid angle at high inclinations (resulting in a lower L_{2keV} for higher inclinations).

The high inclination, ‘BALQSO-like’ viewing angles show moderate agreement with the data, and are X-ray weak due to bound-free absorption and electron scattering in the wind. Typically, BALQSOs show strong X-ray absorption with columns of $N_H \sim 10^{23} \text{ cm}^{-2}$ (Green & Mathur 1996; Mathur et al. 2000; Green et al. 2001; Grupe et al. 2003b). This is often cited as evidence that the BAL outflow is shielded from the X-ray source, especially as sources with strong X-ray absorption tend to exhibit deep BAL troughs and high outflow velocities (Brandt et al. 2000; Laor & Brandt 2002; Gallagher et al. 2006). Our results imply that the clumpy BAL outflow itself can be responsible for the strong X-ray absorption, and supports Hamann et al.’s (2013) suggestion that geometric effects explain the weaker X-ray absorption in mini-BALs compared to BALQSOs.

3.3.4 LoBALs and Ionization Stratification

At high inclinations, the synthetic spectra exhibit blue-shifted BALs in Al III and Mg II – the absorption lines seen in LoBALQSOs – and even show absorption in Fe II at the highest inclinations. Line profiles in velocity space for C IV, Al III and Mg II, are shown in Fig. 3.10 for a range of BALQSO viewing angles. Ionization stratification of the wind causes lower ionization material to have a smaller covering factor, as demonstrated by figures 3.4 and 3.10. This confirms the behaviour expected from a unification model such as Elvis (2000). LoBALs are only present at viewing angles close to edge-on ($i > 75^\circ$),

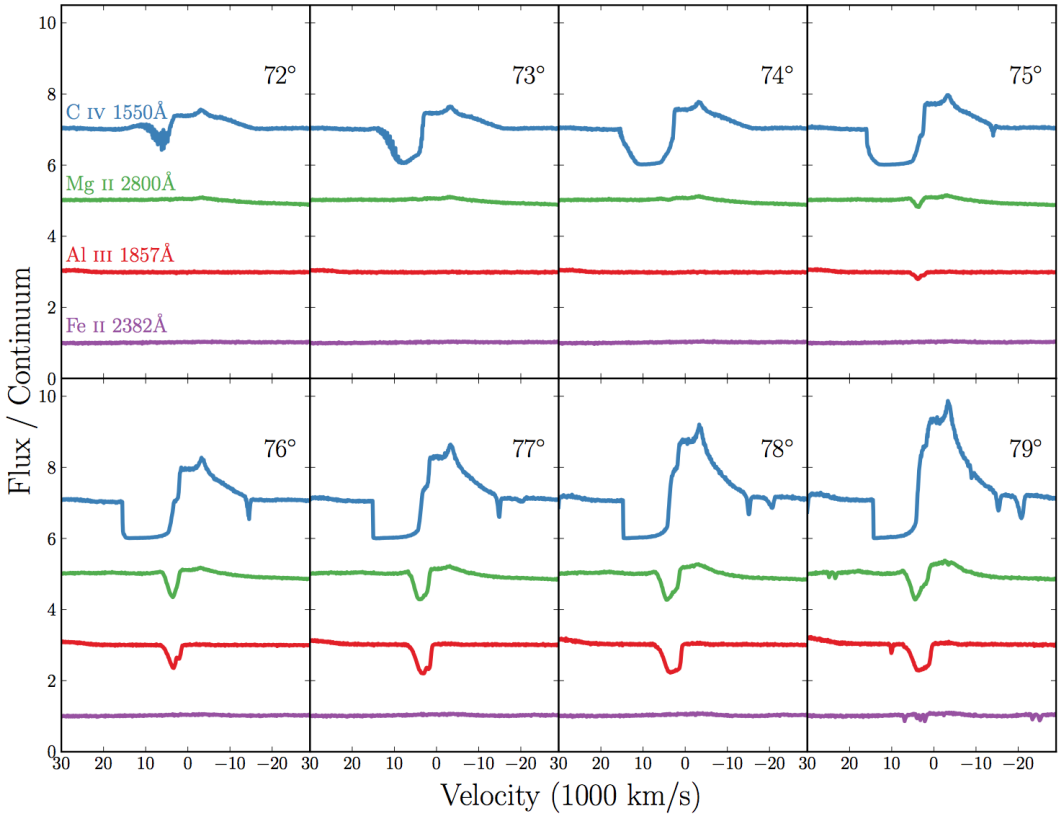


FIGURE 3.10: C IV, Mg II, Al III and Fe II line profiles for viewing angles from 72° – 79° . The profiles are plotted relative to the local continuum with an offset applied for clarity. Lower ionization profiles appear at a subset of high inclinations, compared to the ubiquitous C IV profile.

as predicted by polarisation results (Brotherton et al. 1997). As observed in a BALQSO sample by Filiz Ak et al. (2014), the model BAL troughs are wider and deeper when low ionization absorption features are present, and high ionization lines have higher blue-edge velocities than the low ionization species. There is also a correlation between the strength of LoBAL features and the amount of continuum attenuation at that sightline, particularly blueward of the Lyman edge as the low ionization base intersects the line-of-sight. A model such as this therefore predicts that LoBALQSOs and FeLoBALQSOs have stronger Lyman edge absorption and are more Compton-thick than HiBALQSOs and Type 1 quasars. An edge-on scenario also offers a potential explanation for the rarity of LoBAL and FeLoBAL quasars, due to a foreshortened and attenuated continuum, although BAL fraction inferences are fraught with complex selection effects (Goodrich 1997; Krolik & Voit 1998).

3.4 Discussion

3.4.1 Parameter Sensitivity

Having selected an individual fiducial model from the simulation grid, it is important to briefly explore how specialised this model is, and how small parameter changes can affect the synthetic spectra. Fig. 3.11 shows the EW at a low inclination, and BI at a high inclination for the simulation grid. A few conclusions can be drawn from this plot straight away. First, almost all the models with $f_V = 0.1$ are over-ionized, and fail to produce strong C IV BALs or emission lines. Second, it is difficult to significantly increase line emission while keeping the luminosity and mass loss rate of the system fixed. I show an additional point on figure 7 corresponding to a model with an order of magnitude higher X-ray luminosity and double the mass loss rate. As expected, this results in far higher line EWs, but fails to produce BALs because the collisionally excited emission swamps the BAL profile. In addition, this model would lie well above the expected $L_{2kev} - L_{2500}$ relation in figure 5. Such a high X-ray luminosity could therefore not be the cause of the strong line emission seen in *all* Type 1 quasars.

The parameter search presented here is by no means exhaustive, and conclusions may be limited by the specific parameterisation of the outflow kinematics used. Nevertheless, I suggest that the angular distribution of both the line and continuum emission is perhaps the crucial aspect to understand. With this in mind, obtaining reliable orientation indicators appears to be a crucial observational task if we are to further our understanding of BAL outflows and their connection, or lack thereof, to the broad line region.

3.4.2 Inclination Trends: FWHM and EW

EW increases with inclination in the fiducial model. This trend means that even though significantly denser models can match the line EWs fairly well at low inclinations, they will then possess overly strong red wings to the BAL P-Cygni profiles at high inclinations. The fact that the EW increase in our model are directly related to limb-darkening and foreshortening of the continuum. This appears to contradict observations, which show remarkably uniform emission line properties in quasars and BALQSOs (Weymann et al. 1991; DiPompeo et al. 2012a).

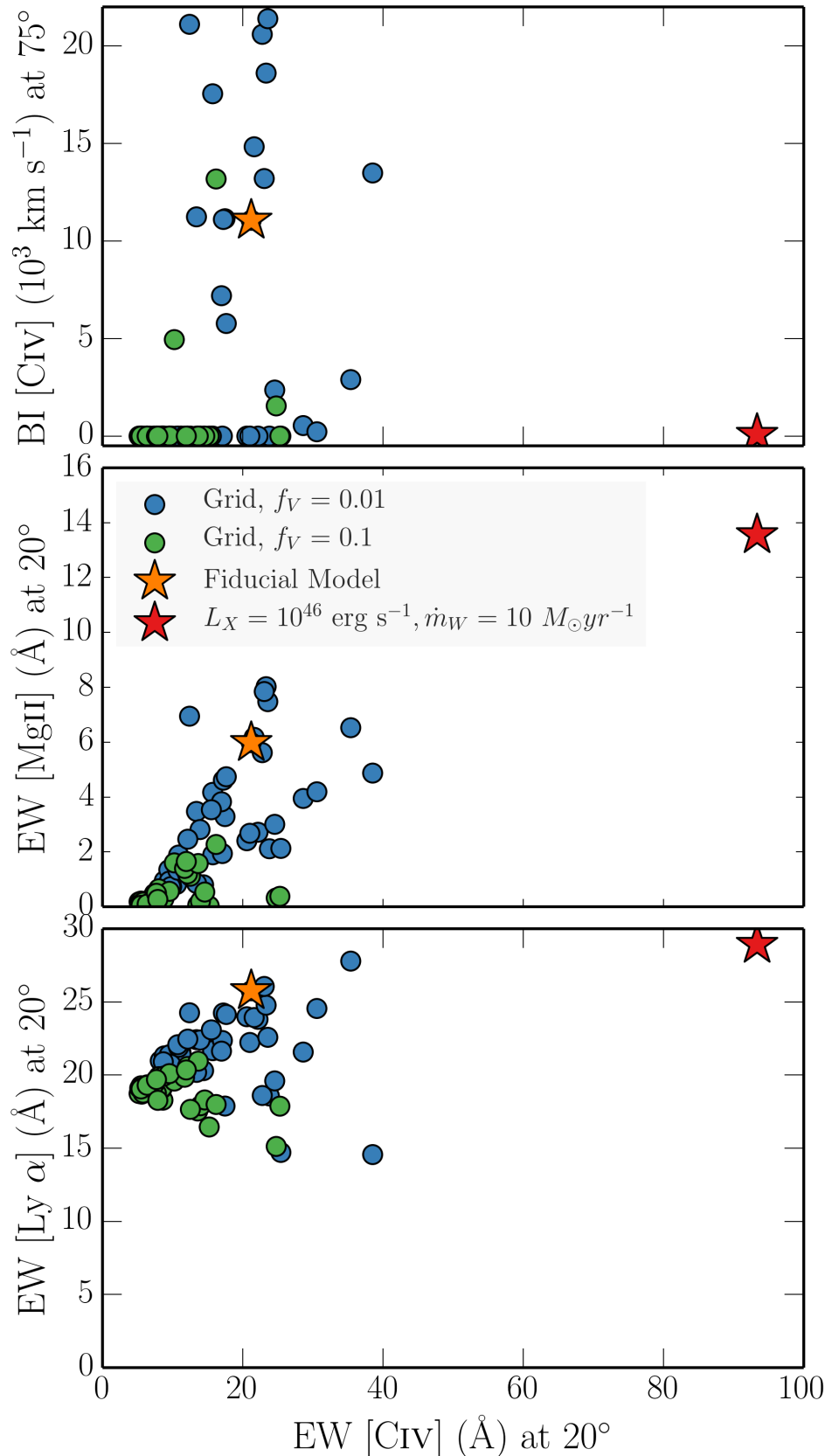


FIGURE 3.11: The EW of the C IV 1550 Å line at 20° plotted against a) the BI of C IV 1550 Å at 75°, b) the EW of the Mg II 2800 Å line at 20° and c) the EW of Ly α at 20°. The circles correspond to the simulation grid for two different values of f_V , and the fiducial model is marked with an orange star. I also show a higher X-ray luminosity model and a higher mass loss rate with a red star.

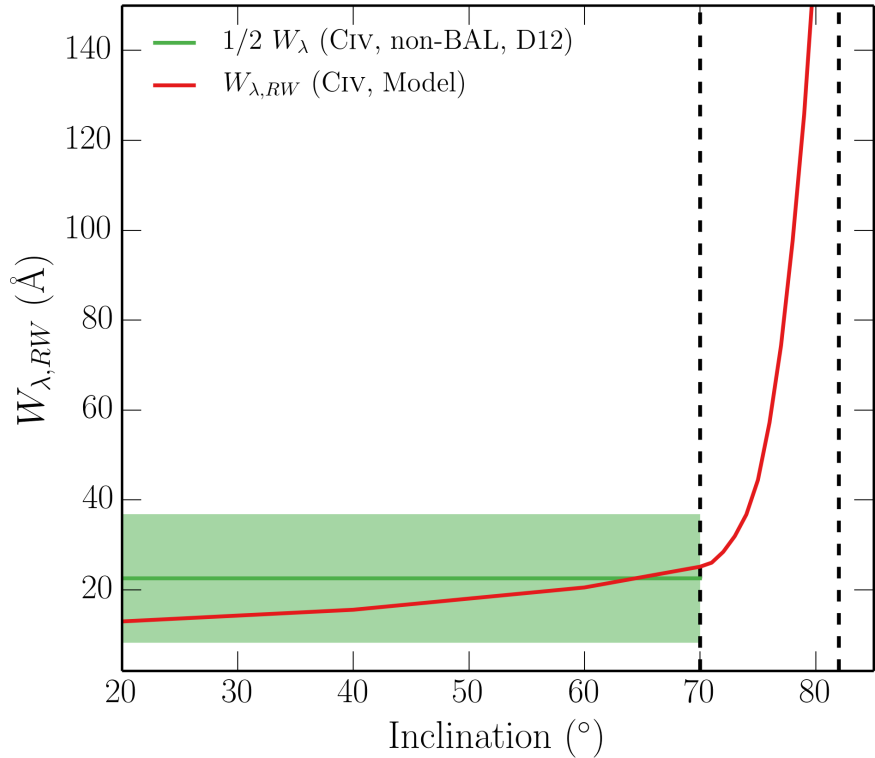


FIGURE 3.12: $W_{\lambda,RW}$ as a function of inclination in the fiducial model, compared to $1/2$ EW from the quasar sample of Di Pompeo et al. (2012; D12).

In order to quantitatively assess how emission lines change with inclination when blue-shifted absorption may affect the line profile, I define the ‘red wing equivalent width’ ($W_{\lambda,RW}$) as

$$W_{\lambda,RW} = \int_{\lambda_0}^{\lambda'} \left(1 - \frac{F_\lambda}{F_0} \right) d\lambda \quad (3.5)$$

where F_0 is the continuum flux and the integral is calculated from λ_0 , line centre, to a wavelength λ' where the flux has returned to the continuum level. This quantity is shown as a function of inclination in Fig. 3.12 for the C IV UV line. The $W_{\lambda,RW}$ expected from isotropic line emission and a foreshortened and limb darkened disc and $1/2$ equivalent widths from DiPompeo et al. (2012a) are also shown.

The variation of EW with inclination is significantly larger than the variation across the quasar population. The angular distribution of the disc continuum and line emission is clearly crucially important in determining the emergent broad line EWs, as suggested by, e.g., the analysis of Risaliti et al. (2011). I shall explore this question further in chapter 6.

3.4.2.1 FWHM and Black Hole Mass Estimates

In a recent study, [Yong et al. \(2016\)](#) used the SV93 wind prescription assess the variation of full-width at half-maximum (FWHM) of H β (and resultant BH mass estimates) with inclination in a disc wind model. Although their model is fairly simple – it does not include, for example, full radiative transfer or ionization physics – this analysis still gives interesting insights into how emission lines from a disc wind might bias BH mass estimates.

If the BLR gas is virialised, as often assumed, then the black hole mass is related to the velocity dispersion, Δv , of the gas by

$$M_{BH} = f \frac{\Delta v^2 R_{BLR}}{G}, \quad (3.6)$$

where R_{BLR} is some appropriate emissivity-weighted radius and is often either assumed, estimated from ionization arguments or calculated from reverberation mapping. When using FWHM to estimate the velocity dispersion the above equation can be rewritten as

$$M_{BH} = f_{FWHM} \left[c \frac{(FWHM)}{\lambda_0} \right]^2 \frac{R_{BLR}}{G}, \quad (3.7)$$

where λ_0 is the central wavelength of the line in question and the FWHM is in the same wavelength units. In a model such as ours the BH mass is known, and determines the escape velocities and rotational motions of the outflow. Thus, using a typical radius for line formation in the model it is trivial to calculate f_{FWHM} for each viewing angle. Fig. 3.13 shows f_{FWHM} as a function of inclination for the C IV, Mg II and H α emission lines in our model, assuming $R_{BLR} = 10^{17}$ cm. For C IV and Mg II the wind angles are not plotted as BAL profiles affect the measurement, and I have compared to H α rather than H β due to the low H β luminosity at some viewing angles. Nevertheless, this value should trace f_{FWHM} from H β fairly well.

The values from our model agree fairly well with the predictions of [Yong et al. \(2016\)](#) from their simpler analysis, suggesting that, at least in this specific set-up, radiative transfer and ionization has a minimal role in determining the emergent FWHM. Instead, the effect is dominated by velocity projection effects. The reason for the significantly

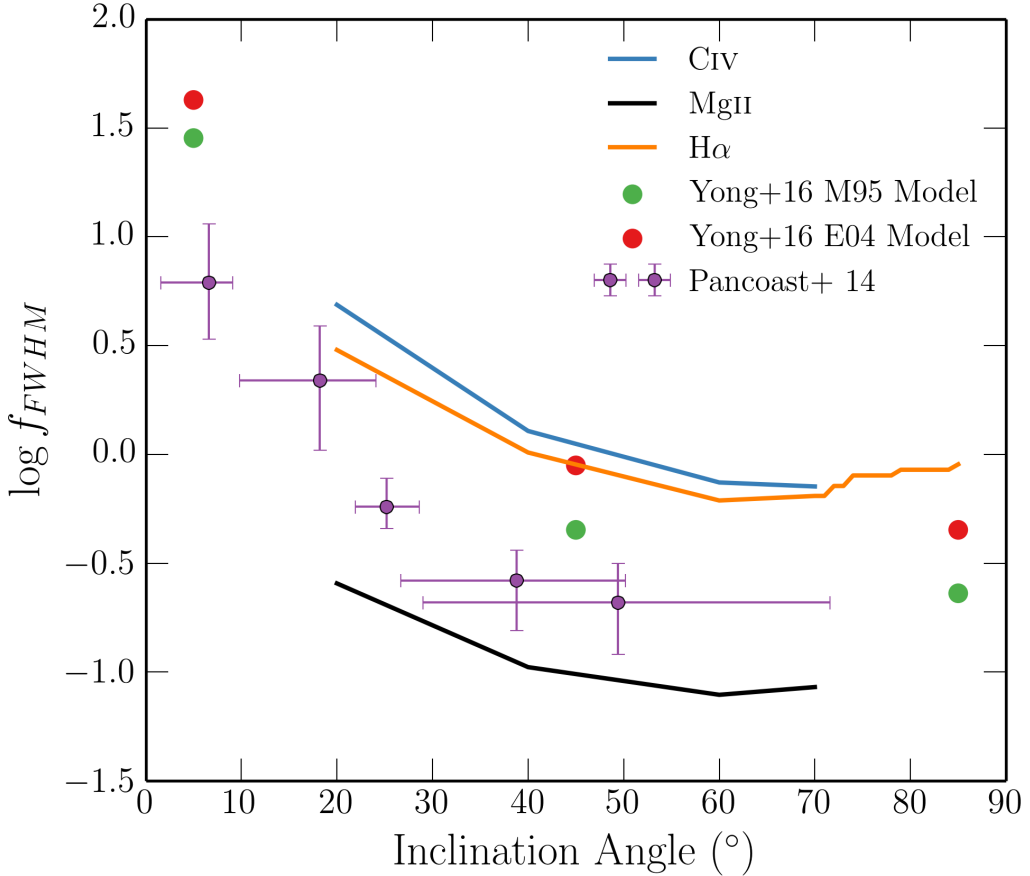


FIGURE 3.13: f_{FWHM} as a function of inclination from the fiducial model for three different lines, compared to values from Yong et al. 2016 and Pancoast et al. 2014.

lower values for Mg II is that it is actually formed well inside $R_{BLR} = 10^{17}$ cm, highlighting the dangers of using a single BLR radius for BH mass estimates from different lines.

3.5 Summary And Conclusions

I have carried out MCRT simulations using a simple prescription for a biconical disc wind, with the aim of expanding on the work of H13. To do this, two main improvements were necessary: First, I included a simple treatment of clumping, and second, the modelling of recombination lines was improved by treating H and He as ‘macro-atoms’. Having selected a fiducial model from an initial simulation grid, I assessed the viability of such a model for geometric unification of quasars, and found the following main points:

1. Clumping moderates the ionization state sufficiently to allow for the formation of strong UV BALs while agreeing well with the X-ray properties of luminous AGN and quasars.
2. A clumpy outflow model naturally reproduces the range of ionization states expected in quasars, due to its stratified density and temperature structure. LoBAL line profiles are seen at a subset of viewing angles, and Fe II absorption is seen at particularly high inclinations.
3. The synthetic spectra show Ly α line and weak He II 1640Å line as a result of our improved treatment of recombination using macro-atoms. Balmer emission lines and a Balmer recombination continuum are also seen in the optical spectrum, but this is only really significant at high inclination where the continuum is suppressed.
4. The higher X-ray luminosity causes a significant increase in the strength of the collisionally excited emission lines produced by the model. However, the equivalent-width ratios of the emission lines do not match observations, suggesting that a greater volume of dense ($n_e \sim 10^{10} \text{ cm}^{-3}$) material may be required.
5. The line EWs in the synthetic spectra increase with inclination. BAL and non-BAL quasar composites have comparable EWs, so our model fails to reproduce this behaviour. If the BLR emits fairly isotropically then for a foreshortened, limb-darkened accretion disc it is not possible to achieve line ratios at low inclinations that are comparable to those at high inclinations. I suggest that understanding the angular distribution of line and continuum emission is a crucial question for theoretical models.

This work confirms a number of expected outcomes from a geometric unification model, and suggests that a simple biconical geometry such as this can come close to explaining much of the phenomenology of quasars. However, our conclusions pose some challenges to a picture in which BALQSOs are explained by an *equatorial* wind rising from a classical thin disc, and suggest the angular distribution of emission is important to understand if this geometry is to be refuted or confirmed. I suggest that obtaining reliable observational orientation indicators and exploring a wider parameter space of outflow geometries in simulations are obvious avenues for future work.

Chapter 4

Quasar Emission Lines as Probes of Orientation and Unification

This chapter is based on a paper in preparation:

Matthews J. H., Knigge C., ‘Quasar Emission Lines as Probes of Orientation and Unification’, to be submitted to MNRAS.

4.1 Introduction

In the previous chapter, I presented tests of geometric unification models using MCRT and photoionization simulations. One of the key results from that analysis is that trends with inclination prohibit models with equatorial outflows matching observations, as the EW of the emission lines tend to increase with inclination. This trend has clear implications for the geometries of BAL outflows; the viewing angle may determine many of the selection effects at work and must therefore be understood before the true covering factor of BAL outflows can be accurately determined. The covering factor and opening angle of the outflow are important quantities to measure in order to calculate the feedback efficiency (e.g. [Borguet et al. 2012](#)), and make inferences about the outflow physics (e.g. [Proga 2005](#)).

Unlike in galactic accretion disc systems, measuring inclinations for quasars and AGN is notoriously difficult, and obtaining reliable orientation indicators is thus an important

observational goal for the community. Perhaps as a result of this problem, directly opposing geometries have been proposed for BAL outflows (see section ??). Here, I use observational data from the Sloan Digital Sky Survey to constrain the inclinations of BAL quasars. Similar attempts have been made previously with different diagnostics; for example, by considering radio properties (Zhou et al. 2006; DiPompeo et al. 2012b), polarisation (Brotherton et al. 2006) and general emission line properties (DiPompeo et al. 2012a).

This chapter is structured as follows. First, I describe the data sample and selection criteria being used. I begin by simply examining the distributions of the EW of the O III 5007Å emission line, EW[O III], and comparing the BAL and non-BAL quasar distributions. In section 4.3 I review the angular distribution of continuum emission one would expect from simple α -disc models, as well as exploring the same quantity in more advanced disc models computed with AGNSPEC. I then use these theoretical angular distributions applied to a simple toy model in section 4.4, and conduct MC simulations in an attempt to fit the observed BAL and non-BAL quasar distributions of EW[O III], using a similar approach to Risaliti et al. (2011, hereafter R11). In section 4.5 I discuss the results in the context of radio and polarisation measurements of AGN, as well as exploring the location of BAL quasars in ‘Eigenvector 1’ parameter space. Finally, in section 4.6, I summarise the findings.

4.2 Data Sample

The data sample is based upon the Shen et al. (2011, hereafter S11) catalog of 105,783 quasars from the The Sloan Digital Sky Survey (SDSS) Data Release 7 (DR7). As I will use emission line diagnostics in this study, this sample must be further divided according to which emission lines are present in the SDSS wavelength range at a given redshift. Sample A contains all quasars within the redshift range $0.35 < z < 0.83$, such that the Mg II 2800A and O III 5007Å line EWs are both measured, and Mg II BAL identification is possible. Sample B contains all quasars within the redshift range $1.45 < z < 2.28$, such that the EWs and presence of BALs in Mg II 2800A and CIV 1550A are both measurable. The details of these samples are shown in table 1.

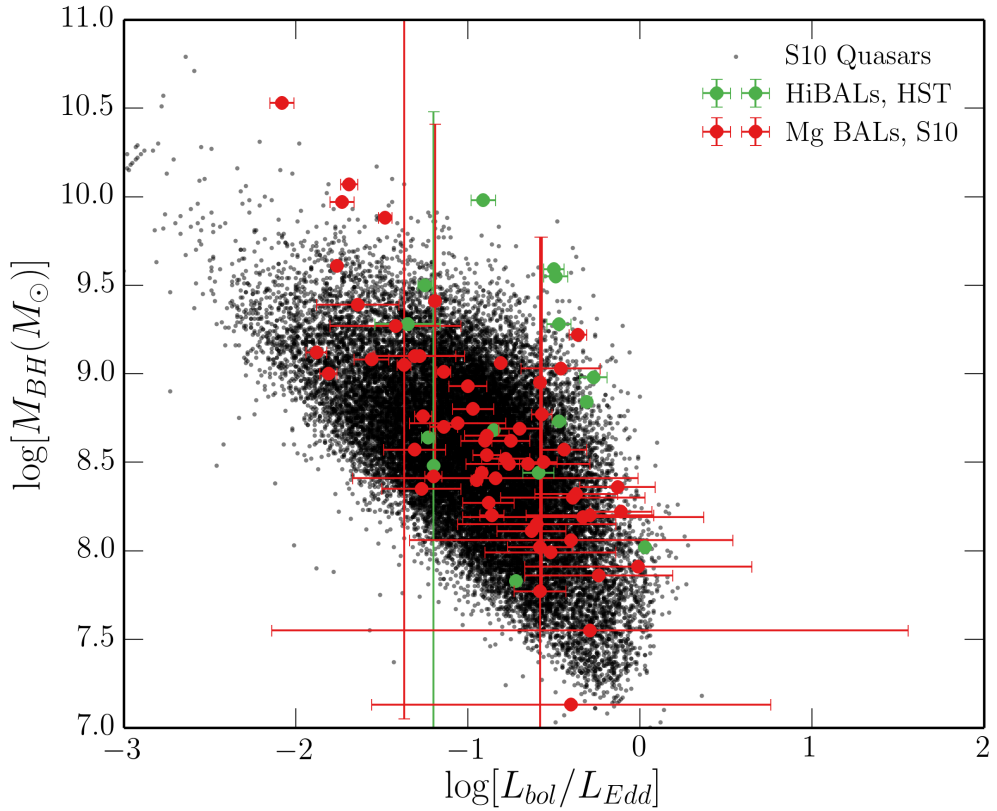


FIGURE 4.1: BH mass and Eddington fraction for the BAL samples plotted over the overall quasar sample from S11.

In attempting to draw broad conclusions about unification models as a whole, we would like to be able to construct a large homogenous dataset of *HiBAL* and non-BAL quasars, both with O III 5007Å EWs. Unfortunately, the wavelength limits of SDSS do not allow this. One of the problems with using just LoBAL quasars as tests of unification is that there is evidence that they are drawn from a different population than normal quasars, perhaps suggesting an *evolutionary* origin. Examples include anomalously high LoBAL fractions in dust-reddened quasar samples (Urrutia et al. 2009) and infra-red selected samples (Dai et al. 2012); although see also Lazarova et al. (2012). To partially address this issue, I also build a small sample of HiBAL quasars in SDSS by cross-matching the S11 catalog with BALs identified in the HST COS archive. BALs were selected from the COS spectra using the balnicity index, BI , defined in equation ???. HST objects were designated as HiBALs by satisfying the condition that $BI > 0$ in one of CIV, NV, SiIV. The mass and Eddington fraction measurements from S11, with errorbars, are shown against the background distribution of all quasars.

Fig. 2 shows histograms of a number of different emission line properties for samples A

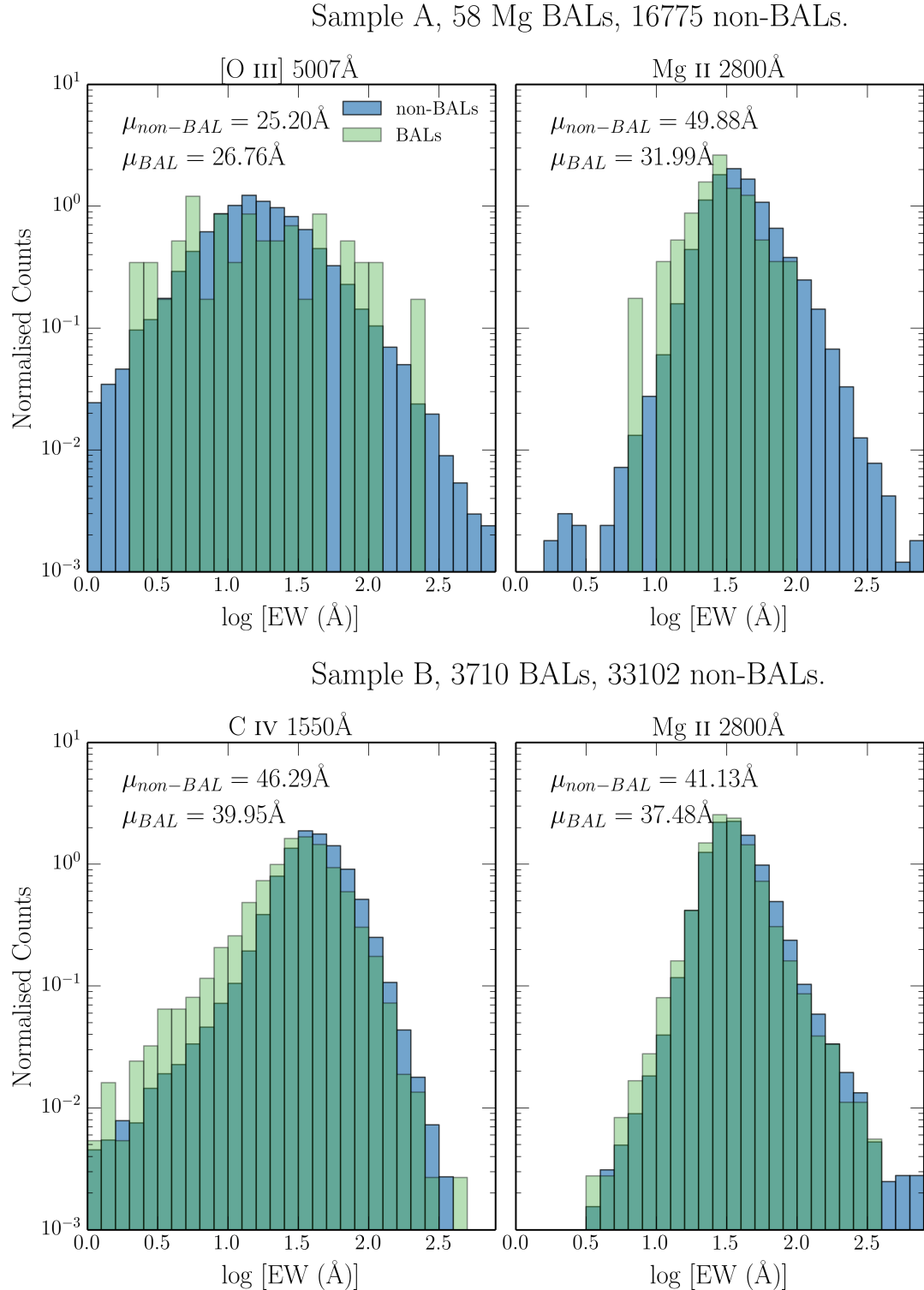


FIGURE 4.2: Histograms of equivalent widths for three emission lines from the two different samples.

and B. As discussed by previous authors (e.g. [Weymann et al. 1991](#)), I find that BAL and non-BAL quasars really do seem to possess very similar emission line properties. The EW is related to the ‘face-on’ equivalent width, EW_0 by the equation

$$EW = EW_0 / \epsilon(\theta) \quad (4.1)$$

where θ is the viewing angle with respect to the symmetry axis and $\epsilon(\theta)$ is the ‘angular emissivity function’, which describes how the continuum luminosity from the disc varies as a function of viewing angle. For a foreshortened disc this is simply $\epsilon(\theta) = \cos \theta$.

Thus, if BAL quasars are viewed from a larger viewing angle on average then one would expect them to possess higher EWs, with a broader distribution. It is already apparent from figure 1 that the BAL distribution mean is not systematically higher than the non-BAL mean – in fact, it is lower. This is not expected from a model in which the continuum is foreshortened and BAL outflows are at all equatorial. This problem is examined further in section 4.4. First, I will examine the motivations for different forms of $\epsilon(\theta)$ in AGN and quasars.

4.3 The Angular Distribution of Emission from an Accretion Disc

The most widely-used theoretical model for an accretion disc was proposed by Shakura & Sunyaev (1973; hereafter SS73). There are a number of well-documented problems when fitting AGN SEDs with SS73 accretion disc models (REFs), and there are also tensions with the ‘accretion disc size’ relation from time lags ([Edelson et al. 2015](#)) and microlensing ([Morgan et al. 2010](#)). Despite these problems, [Capellupo et al. \(2015\)](#) recently had some success fitting VLT XSHOOTER spectra of AGN when the effects of GR, mass-loss and comptonisation were included. In this section, I start by discussing the angular distribution of emission from an SS73 disc, before discussing opacity and GR effects. In order to explore these effects, I use AGNSPEC ([Hubeny et al. 2000](#); [Davis & Hubeny 2006](#); [Davis et al. 2007](#)). I stress that the discussion here is not limited to SS73 discs; the only real condition for the expected angular distributions derived here is that the disc is geometrically thin and optically thick.

4.3.1 Standard Thin Disc Models

Any geometrically thin, optically thick disc will appear foreshortened and limb darkened (if temperature decreases with height from the central disc plane). Foreshortening is a simple $\cos \theta$ geometric effect, where θ is the inclination with respect to the vertical z axis, which is perpendicular to the disc plane. Limb darkening, $\eta(\theta)$, is given by

$$\eta(\theta) = a(1 + b \cos \theta), \quad (4.2)$$

where a is a normalisation constant and b governs the strength of the limb darkening. $b = 3/2$, known as the Eddington approximation tends to give good agreement with solar observations (e.g. [Mihalas 1978](#)). The two effects can be combined to give an angular emissivity function, of

$$\epsilon(\theta) = a \cos \theta \left(1 + \frac{3}{2} \cos \theta\right). \quad (4.3)$$

4.3.2 Including GR, Comptonisation and Opacity Effects

In reality, limb darkening is not frequency independent and depends on the bound-free and bound-bound opacities in the disc. In addition, it has been shown that GR can ‘isotropize’ the radiation field in XRBs ([Zhang et al. 1997](#); [Muñoz-Darias et al. 2013](#)), in some cases overcoming foreshortening effects. To assess the impact of GR and disc opacities on $\epsilon(\theta)$ I use AGNSPEC models, which uses stellar atmosphere calculations to calculate the SED in a series of annuli, before using the KERRTRANS code to calculate the emergent SED by ray-tracing along Kerr geodesics. Fig. 4.3 shows $\epsilon(\theta)$ as a function of θ for AGNSPEC models for minimally and maximally spinning BHs, compared to foreshortened and limb-darkened predictions for SS73 models. Clearly, there is very little effect; the accretion disc is still strongly anisotropic in the relevant wavebands.

4.4 Predicted EW distributions compared to observations: A Monte Carlo approach

I assume $\epsilon(\theta) = \cos \theta$, as this is the conservative estimate.

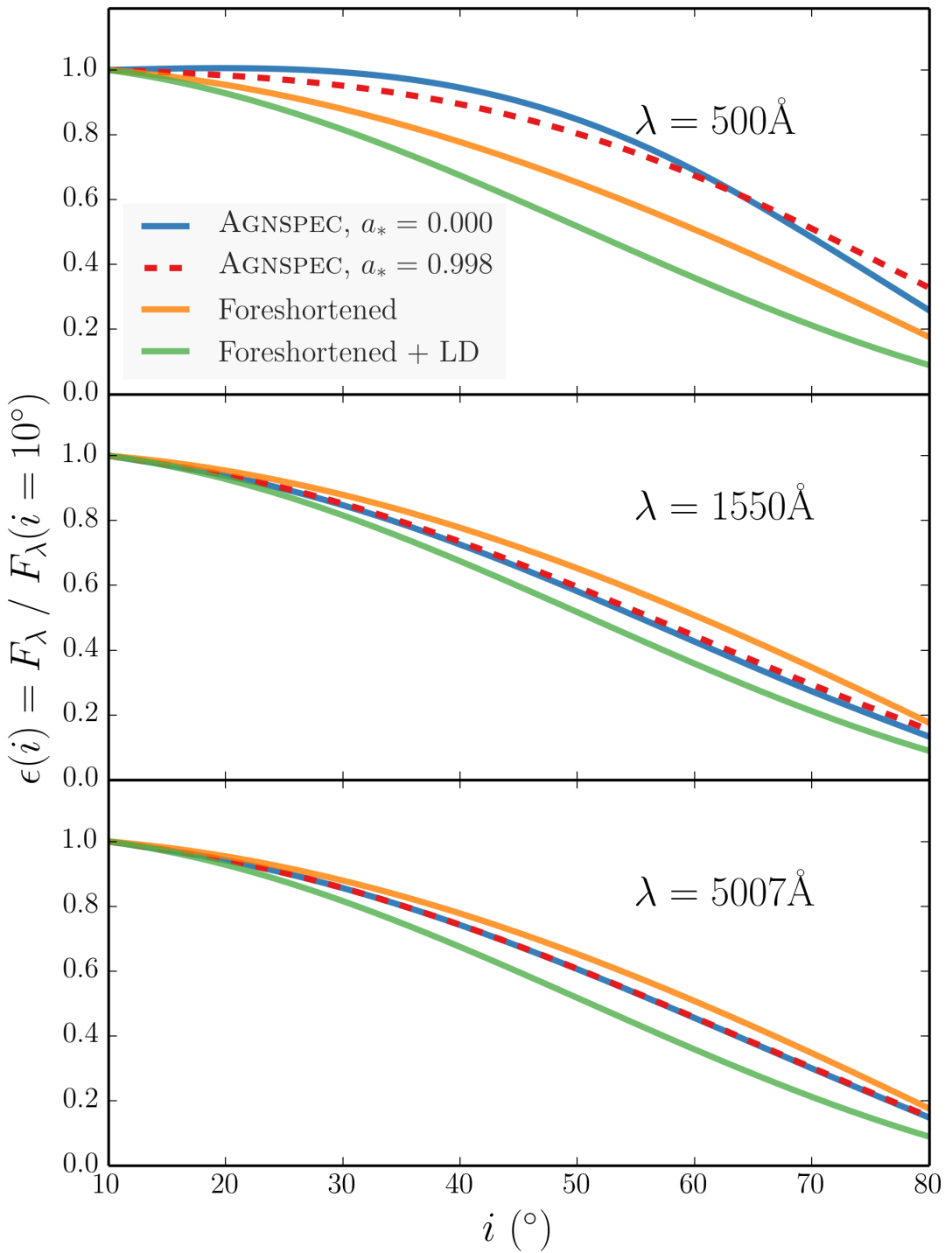


FIGURE 4.3: Monochromatic continuum luminosities from AGNSPEC and classical thin disc models.

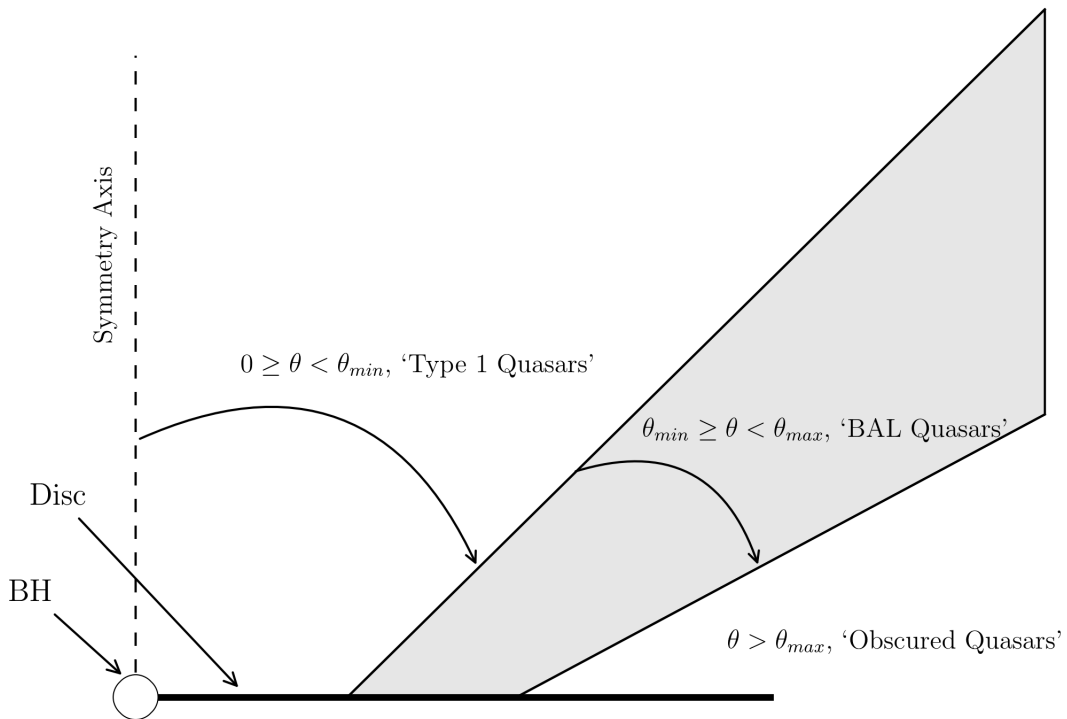


FIGURE 4.4: The geometry of the toy model used to carry out the Monte Carlo simulations

The Monte Carlo simulation undergoes the following steps:

1. A set of isotropic angles is chosen such that $P(\theta) \propto d\Omega(\theta)$. If $\theta_{min} < \theta < \theta_{max}$ then the fake object is flagged as a mock BAL. If $\theta < \theta_{min}$ then the fake object is designated a non-BAL, and otherwise the object is ignored. To be included in the sample, the object also has to survive a selection test based on a arbitrary flux selection limit, to simulate the distribution of angles in a flux-limited sample.
2. I then construct a best estimate of the intrinsic (i.e. ‘face-on’) EW distribution for non-BAL quasars. This is done via a χ^2 minimisation, by finding the gaussian with μ and σ which best reproduces the observed distribution when convolved with the non-BAL angles generated in the previous step. a χ^2 minimisation.
3. For each mock sample, a EW_0 is drawn from the intrinsic gaussian.
4. A mock EW is estimated such that $EW = EW_0/\epsilon(\theta)$, and this process is repeated to build up a mock sample of objects.

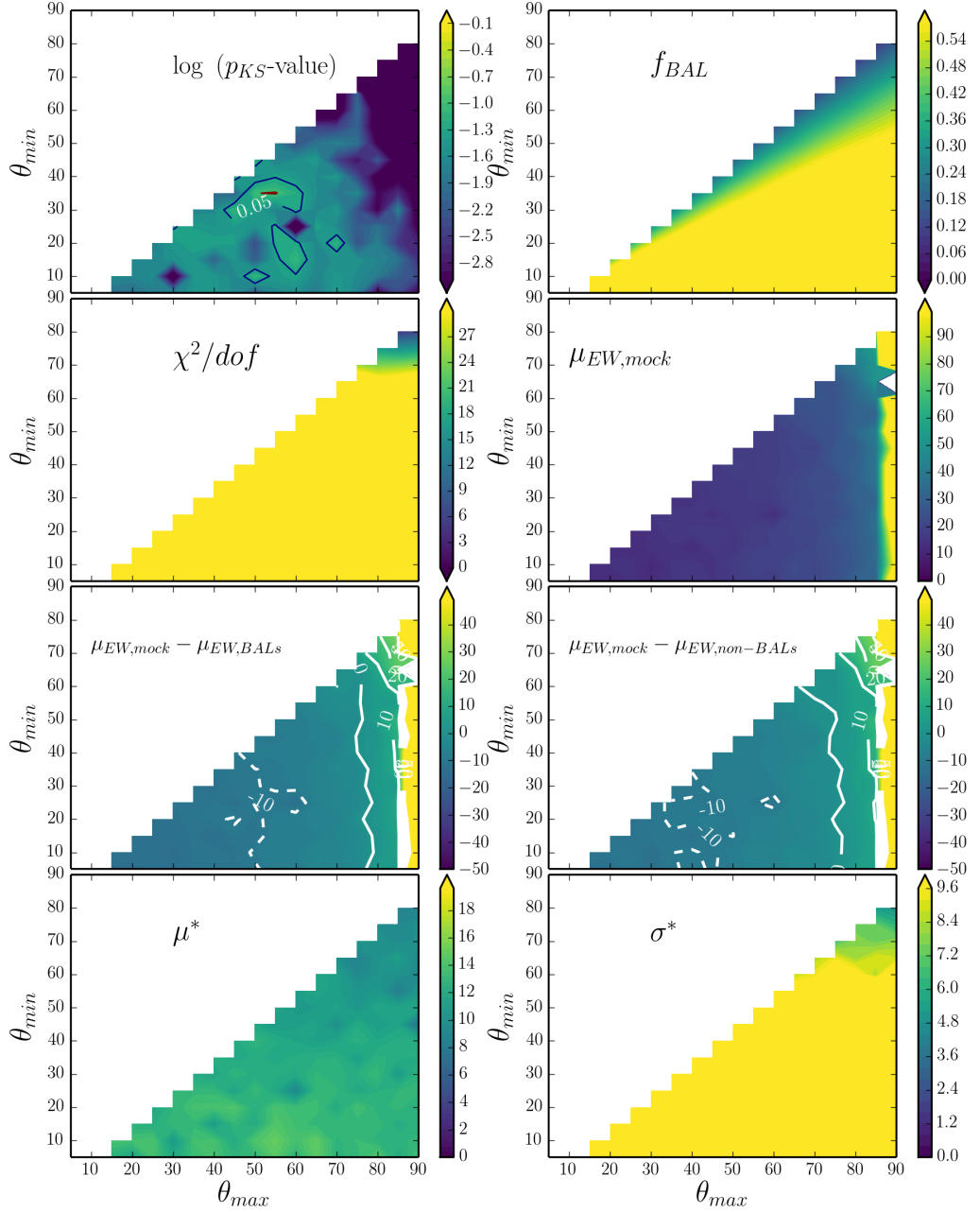


FIGURE 4.5: Contour plots from the Monte Carlo simulations.

| Par. A | Par. B | $r_{corr,AB}$ (non- BALs) | $r_{corr,AB}$ (BALs) |
|---------------------------------|------------------------------|---------------------------------|-------------------------|
| $\log[\text{EW}[\text{O III}]]$ | $\text{FWHM}[\text{H}\beta]$ | 0.14 | 0.18 |
| $\log[\text{EW}[\text{O III}]]$ | R_{FeII} | -0.51 | -0.67 |
| $\text{FWHM}[\text{H}\beta]$ | R_{FeII} | -0.26 | -0.42 |

TABLE 4.1: Eigenvector 1 correlation coefficients

5. The number of objects in the mock sample with $\theta_{min} < \theta < \theta_{max}$ is recorded, providing an estimate of the expected BAL fraction for this wind geometry. This already includes a selection effect for the weaker continuum flux.
6. The value of the K-S test statistic is recorded, in which the mock BAL sample is compared to the real BAL sample. The mean and variance of the mock sample is also recorded. This allows us to ascertain which regions of parameter space best fit the observed BAL distribution

This process is repeated for a grid of θ_{min} and θ_{max} . The results are shown in figure 4.5, in which the mean, standard deviation and f_{BAL} are shown as a function of θ_{min} and θ_{max} . As expected, equatorial viewing angles are strongly disfavoured.

4.5 Discussion

I have demonstrated that the EW distributions of the O III 5007Å emission line in quasars is not consistent with a model in which BAL quasars are viewed from equatorial angles and the continuum emission originates from a foreshortened accretion disc. This conclusion would be strengthened were I to include limb darkening. This conclusion is extendible to the broad emission lines, with the caveat that those lines are dipole transitions and so opacity effects can change the angular distribution of emission. I will now explore how the above results compare to other observations of quasars that are expected to probe system orientation.

4.5.1 Eigenvector 1

Eigenvector 1 (EV1) is a fundamental parameter space for AGN and quasars ([Boroson & Green 1992](#); [Sulentic et al. 2000](#); [Marziani et al. 2001](#); [Shen & Ho 2014](#)). It relates the

FWHM of H β , FWHM[H β], the relative iron strength, R_{FeII} and the EW[O III]. Both EW[O III] and FWHM[H β] have been used as orientation indicators, and so comparing the BAL EV1 distribution to the non-BAL EV1 distribution is particularly interesting.

Fig. 4.6 shows the quasar distribution from sample A in EV1 parameter space, with BAL quasars from samples A and B overplotted. (Shen & Ho 2014, hereafter SH14) propose that the main inclination driver in the parameter space is FWHM[H β], and that high inclination sources should thus cluster around a diagonal line from the lower right to upper left quadrants. Conversely, R11’s analysis instead suggests that high inclination sources should cluster around high EW OIII widths. As EW[O III] and FWHM[H β] are very weakly correlated (Spearman’s rank coefficient of 0.13), this means they should lie to the left of the parameter space. Inspection of the figure clearly shows that BAL quasars are not only found in one region of the EV1 parameter space.

In order to assess this more quantitatively, I have shown contours of quasar counts overlaid on the scatter plot. The contours correspond to the number of objects in each bin, where the bins are of size $\Delta R_{\text{FeII}} = 0.2$ and $\Delta \text{FWHM}[\text{H}\beta] = 500 \text{km s}^{-1}$. The percentage of quasars falling within the inner contour is 45%, whereas only 18% of BAL quasars fall in the space. Conversely, 24% of BAL quasars fall outside the outermost contour compared to 10% of non-BAL quasars. It would therefore appear that BAL quasars are preferentially clustered towards the high-mass and high-inclination end of EV1 space (under the interpretation of SH14). This is further illustrated by Fig. 4.7, which shows the LoBAL fraction in the same bins, compared to the mean LoBAL fraction. This is again suggestive of an overdensity towards the upper right of the parameter space. It is also clear that a unification picture in which BAL quasars are viewed exclusively from high inclinations is ruled out, under both the R11 and SH14 interpretations.

Larger datasets, preferably including HiBAL quasars with EV1 measurements, are needed in order to properly constrain the EV1 behaviour of BAL quasars. However, overall, the behaviour of FWHM[H β] strengthens the above conclusion that BAL quasars are not always viewed from extreme inclinations.

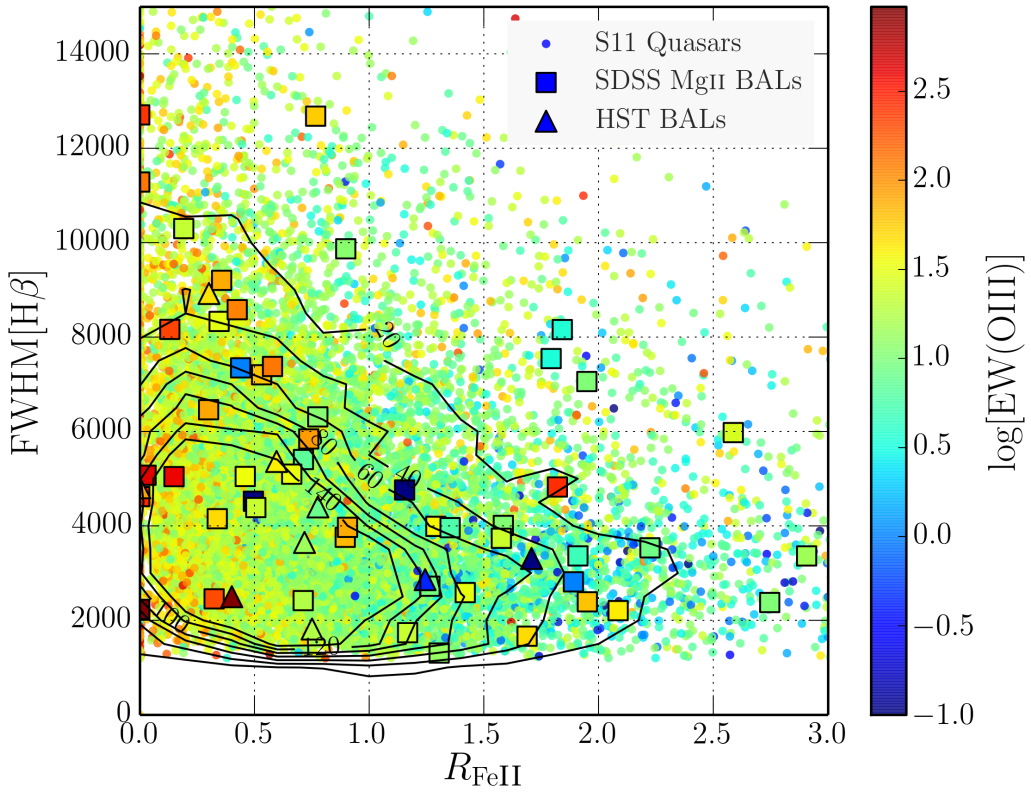


FIGURE 4.6: Eigenvector 1 for BAL and non-BAL quasars. FWHM of the $H\beta$ line plotted against the relative iron strength, R_{FeII} . The colour coding corresponds to the EW of OIII. The dots mark all quasars from sample A, while the squares mark those with Mg II BALs. The triangles show the HST BAL quasars from sample B.

4.5.2 Radio Observations

Fig. ? shows the equivalent width distributions in radio-loud quasars, split into core or lobe dominated. This designation is commonly used as an orientation indicator (Orr & Browne 1982; Wills & Brotherton 1995). Although th

In this case, we can see that A full investigation of this is beyond the scope

4.5.3 Polarisation

Polarisation measurements of BAL quasars tend to show two properties. The first is a polarisation angle of $\gtrsim 60^\circ$ with respect to the radio jet axis in RL source (Brotherton et al. 2006). The second is a polarisation percentage of around 2.4 times greater, on average, than the non-BAL population. The polarisation percentages of a sample of

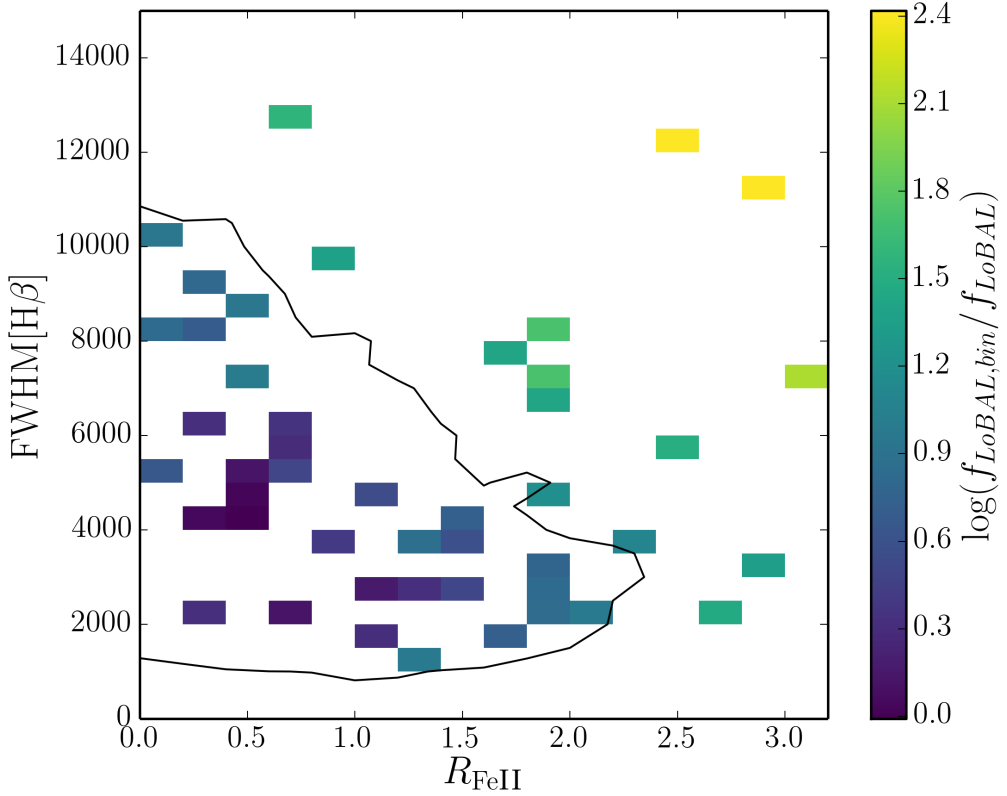


FIGURE 4.7: LoBAL fraction compared to mean LoBAL fraction in Eigenvector 1 space. The contour shows the outermost contour from Fig. 4.6 for reference.

BAL quasars from REF are compared to the Type I and Type II AGN populations from REF in Fig. 4.8.

The polarisation properties of BAL quasars offer some of the best insights into the geometries of BAL outflows, some of which appear to be in contrast with the conclusions drawn from emission line and radio properties.

4.5.4 Theoretical Considerations

Discuss Proga models: They tend to rise fairly equatorially (see eg. PK04) Talk to Nick?

4.6 Conclusions

I have explored the emission line properties of BAL and non-BAL quasars and found that they are inconsistent with a unification picture in which BAL outflows rise equatorially from a foreshortened or limb darkened accretion disc. Based on these findings, it is

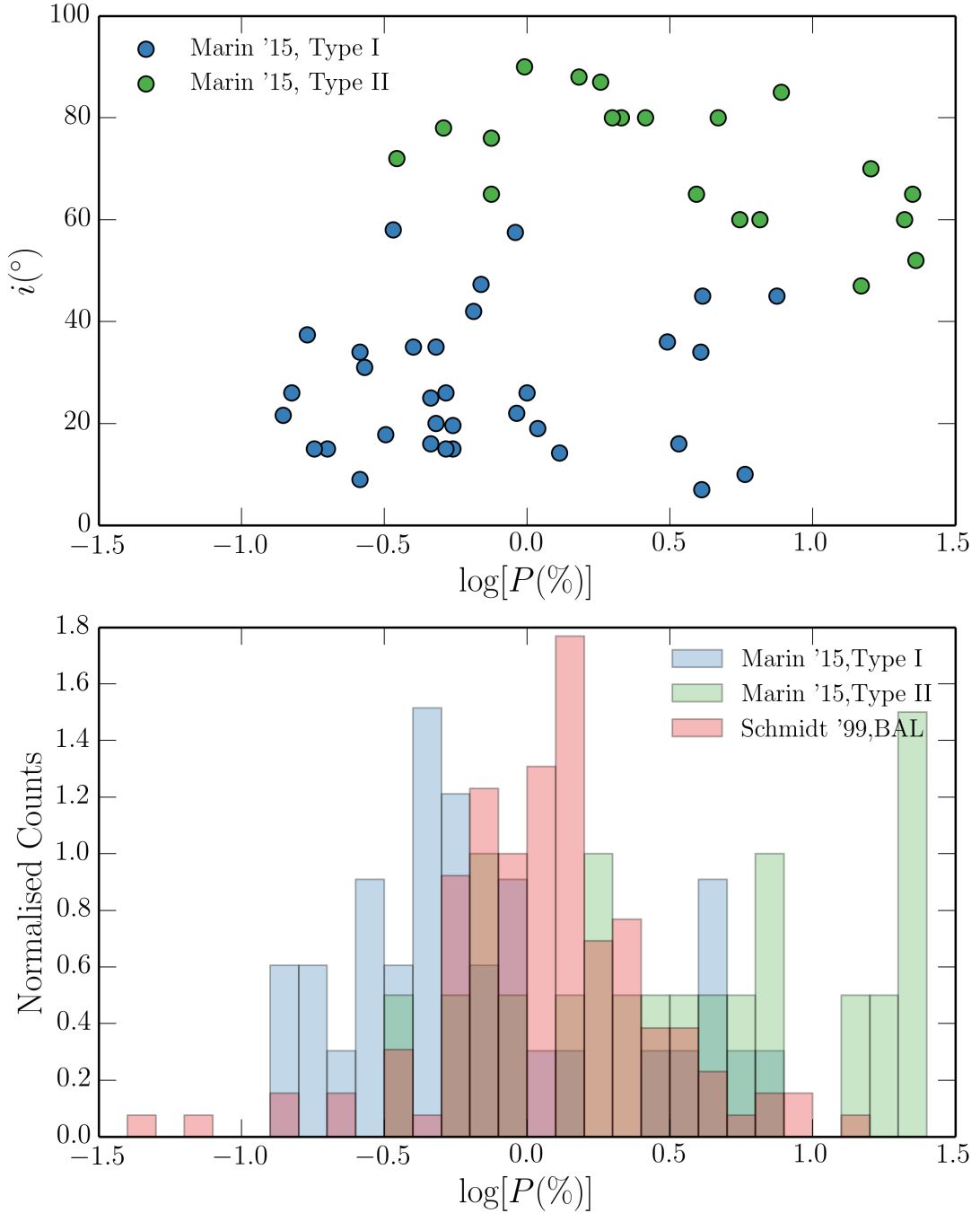


FIGURE 4.8: *Top:* Polarisation percentages as a function of measured inclination from Marin et al. (2015) for Type I and Type II AGN. *Bottom:* Histograms of polarisation percentages for BAL quasars from Schmidt et al. (1999) together with the Marin et al. (2015) AGN sample.

possible to construct a few possible scenarios that are not ruled out by the above results. these conclusions have the caveat that I have assumed that conclusions drawn about LoBAL quasars can be extended to BAL quasars in general.

- *Scenario 1:* The quasar continuum is roughly isotropic, which is not expected from a geometrically thin, optically thick accretion disc. I have demonstrated that general relativistic effects cannot account for this discrepancy in the UV. Reprocessing by surrounding dense plasma with a large covering factor or limb brightening in the disc may provide possible explanations which this analysis cannot yet confirm or refute.
- *Scenario 2:* Quasar discs are strongly anisotropic, as expected from a geometrically thin, optically thick accretion disc. In this case, BAL outflows cannot only emerge at extreme inclinations and should instead be seen at very similar angles to non-BAL quasars. Polarisation measurements need to be reconciled with this hypothesis. I recommend that future RT modelling efforts explore different outflow geometries and that detailed polarisation modelling is undertaken to constrain the outflow opening angles.
- *Scenario 3:* The geometric unification model does not explain the incidence of BALs in quasars, or requires an additional component which is *time-dependent*, such as an evolutionary or accretion state origin for BAL outflows. In this scenario, BAL quasars would be seen from very similar angles to non-BAL quasars. However, the evidence for this is limited and there is no good model for why outflows would exist only for $\sim 20\%$ of a quasar's lifetime. Even if this is the case, then the covering factor of the outflow still needs to be constrained in order to estimate the BAL duty cycle.

Regardless of the conclusions about BAL quasars and their outflow geometries, this analysis allows conclusions to be drawn about the *overall* quasar population. In scenario 1, the EW[O III] distribution of quasars cannot be driven by inclination as suggested by ([Risaliti et al. 2011](#)). It is also clear from the work presented here that $\log R$, EW[O III] and FWHM H β are *cannot all* be reliable orientation indicators. Furthermore, if a geometric unification does explain BAL quasars, then absorption effects cannot be responsible for the observed EW[O III] distribution. The above conclusions each pose a

different challenge to the current understanding of, respectively, accretion physics, polarisation measurements and geometric unification models. This work therefore adds to the growing evidence that our simplest models are not sufficient to describe the overall quasars and that alternatives should be sought.

Chapter 5

Conclusions

“...and the credits rave as the critics roll.”

Mike Vennart, Silent/Transparent

In the first study I demonstrated that accretion disc winds can have a profound impact on the optical spectra of CVs – a region of the spectrum often assumed to have nothing to do with outflows.

In chapter 5, I applied similar techniques to the question of quasar unification.

5.1 Suggestions for Future Work

5.1.1 CVs as Accretion and Outflow Laboratories

5.1.2 Improving the Treatment of Clumping

5.1.3 Expanding the Capabilities of python

5.1.4 Obtaining Reliable Orientation Indicators

5.2 Closing Remarks

Bibliography

- Abbott D. C., 1982, ApJ 259, 282
- Abbott D. C., Lucy L. B., 1985, ApJ 288, 679
- Adams F. C., Graff D. S., Richstone D. O., 2001, ApJ Letters 551, L31
- Alexander D. M., Bauer F. E., Brandt W. N., Daddi E. et al., 2011, ApJ 738, 44
- Allen J. T., Hewett P. C., Maddox N., Richards G. T., Belokurov V., 2011, MNRAS 410, 860
- Antonucci R., 1988, in M. Kafatos (ed.), Supermassive Black Holes, p. 26
- Antonucci R., 2013, Nature 495, 165
- Antonucci R., Geller R., Goodrich R. W., Miller J. S., 1996, ApJ 472, 502
- Antonucci R. R. J., Miller J. S., 1985, ApJ 297, 621
- Arav N., 1996, ApJ 465, 617
- Arav N., Becker R. H., Laurent-Muehleisen S. A., Gregg M. D. et al., 1999a, ApJ 524, 566
- Arav N., Korista K. T., Barlow T. A., Begelman, 1995, Nature 376, 576
- Arav N., Korista K. T., de Kool M., Junkkarinen V. T., Begelman M. C., 1999b, ApJ 516, 27
- Arévalo P., Uttley P., 2006, MNRAS 367, 801
- Balbus S. A., Hawley J. F., 1991, ApJ 376, 214
- Baldi R. D., Capetti A., Robinson A., Laor A., Behar E., 2016, MNRAS

- Baldry I. K., Glazebrook K., Brinkmann J., Ivezić Ž. et al., 2004, ApJ 600, 681
- Baptista R., Silveira C., Steiner J. E., Horne K., 2000, MNRAS 314, 713
- Bartlett E., 2013, Ph.D. thesis, University of Southampton
- Becker R. H., White R. L., Gregg M. D., Brotherton M. S. et al., 2000, ApJ 538, 72
- Begelman M. C., McKee C. F., Shields G. A., 1983, ApJ 271, 70
- Bell E. F., McIntosh D. H., Katz N., Weinberg M. D., 2003, ApJs 149, 289
- Belloni T. (ed.), 2010, The Jet Paradigm, Vol. 794 of *Lecture Notes in Physics, Berlin Springer Verlag*
- Benz A. O., Fuerst E., Kiplinger A. L., 1983, Nature 302, 45
- Bîrzan L., McNamara B. R., Nulsen P. E. J., Carilli C. L., Wise M. W., 2008, ApJ 686, 859
- Blandford R. D., Payne D. G., 1982, MNRAS 199, 883
- Blandford R. D., Znajek R. L., 1977, MNRAS 179, 433
- Bondi H., 1952, MNRAS 112, 195
- Bondi H., Hoyle F., 1944, MNRAS 104, 273
- Bongiorno A., Schulze A., Merloni A., Zamorani G. et al., 2016, A&A 588, A78
- Bonning E. W., Cheng L., Shields G. A., Salviander S., Gebhardt K., 2007, ApJ 659, 211
- Borguet B., Hutsemékers D., 2010, A&A 515, A22
- Borguet B. C. J., Arav N., Edmonds D., Chamberlain C., Benn C., 2013, ApJ 762, 49
- Borguet B. C. J., Edmonds D., Arav N., Dunn J., Kriss G. A., 2012, ApJ 751, 107
- Boroson T. A., Green R. F., 1992, ApJs 80, 109
- Boroson T. A., Meyers K. A., 1992, ApJ 397, 442
- Bowler R. A. A., Hewett P. C., Allen J. T., Ferland G. J., 2014, MNRAS 445, 359
- Braito V., Reeves J. N., Dewangan G. C., George I. et al., 2007, ApJ 670, 978

- Brandt W. N., Laor A., Wills B. J., 2000, ApJ 528, 637
- Brotherton M. S., De Breuck C., Schaefer J. J., 2006, MNRAS 372, L58
- Brotherton M. S., Tran H. D., van Breugel W., Dey A., Antonucci R., 1997, ApJ Letters 487, L113
- Brown J. C., Richardson L. L., Antokhin I., Robert C. et al., 1995, A&A 295, 725
- Burkert A., Silk J., 2001, ApJ Letters 554, L151
- Capellupo D. M., Hamann F., Barlow T. A., 2014, MNRAS 444, 1893
- Capellupo D. M., Hamann F., Shields J. C., Rodríguez Hidalgo P., Barlow T. A., 2011, MNRAS 413, 908
- Capellupo D. M., Hamann F., Shields J. C., Rodríguez Hidalgo P., Barlow T. A., 2012, MNRAS 422, 3249
- Capellupo D. M., Netzer H., Lira P., Trakhtenbrot B., Mejía-Restrepo J., 2015, MNRAS 446, 3427
- Cappi M., Mihara T., Matsuoka M., Hayashida K. et al., 1996, ApJ 458, 149
- Cassinelli J. P., 1979, ARAA 17, 275
- Castor J. I., Abbott D. C., Klein R. I., 1975, ApJ 195, 157
- Castor J. L., 1974, MNRAS 169, 279
- Cavagnolo K. W., McNamara B. R., Wise M. W., Nulsen P. E. J. et al., 2011, ApJ 732, 71
- Chamberlain C., Arav N., Benn C., 2015, MNRAS 450, 1085
- Chartas G., Kochanek C. S., Dai X., Poindexter S., Garmire G., 2009, ApJ 693, 174
- Chen B., Dai X., Baron E., 2013a, ApJ 762, 122
- Chen B., Dai X., Baron E., Kantowski R., 2013b, ApJ 769, 131
- Clavel J., Schartel N., Tomas L., 2006, A&A 446, 439
- Cohen M. H., Ogle P. M., Tran H. D., Vermeulen R. C. et al., 1995, ApJ Letters 448, L77

- Cohen R. D., Puetter R. C., Rudy R. J., Ake T. B., Foltz C. B., 1986, ApJ 311, 135
- Connolly S. D., McHardy I. M., Dwelly T., 2014, MNRAS 440, 3503
- Connolly S. D., McHardy I. M., Skipper C. J., Emmanoulopoulos D., 2016, MNRAS
- Coppejans D. L., Körding E. G., Miller-Jones J. C. A., Rupen M. P. et al., 2015, MNRAS 451, 3801
- Cordova F. A., Mason K. O., 1982, ApJ 260, 716
- Cottis C. E., Goad M. R., Knigge C., Scaringi S., 2010, MNRAS 406, 2094
- Crenshaw D. M., Rodriguez-Pascual P. M., Penton S. V., Edelson R. A. et al., 1996, ApJ 470, 322
- Croton D. J., Springel V., White S. D. M., De Lucia G. et al., 2006, MNRAS 365, 11
- Crummy J., Fabian A. C., Gallo L., Ross R. R., 2006, MNRAS 365, 1067
- Dabrowski Y., Fabian A. C., Iwasawa K., Lasenby A. N., Reynolds C. S., 1997, MNRAS 288, L11
- Dai X., Kochanek C. S., Chartas G., Kozłowski S. et al., 2010, ApJ 709, 278
- Dai X., Shankar F., Sivakoff G. R., 2008, ApJ 672, 108
- Dai X., Shankar F., Sivakoff G. R., 2012, ApJ 757, 180
- Davis S. W., Hubeny I., 2006, ApJs 164, 530
- Davis S. W., Woo J.-H., Blaes O. M., 2007, ApJ 668, 682
- de Kool M., Begelman M. C., 1995, ApJ 455, 448
- Denney K. D., De Rosa G., Croxall K., Gupta A. et al., 2014, ApJ 796, 134
- Dexter J., Agol E., 2011, ApJ Letters 727, L24
- Dhillon V. S., 1996, in A. Evans, J. H. Wood (eds.), IAU Colloq. 158: Cataclysmic Variables and Related Objects, Vol. 208 of *Astrophysics and Space Science Library*, 3
- Dhillon V. S., Rutten R. G. M., 1995, MNRAS 277, 777

- Díaz Trigo M., Boirin L., 2015, ArXiv e-prints
- DiPompeo M. A., Brotherton M. S., Cales S. L., Runnoe J. C., 2012a, MNRAS 427, 1135
- DiPompeo M. A., Brotherton M. S., De Breuck C., 2012b, ApJ 752, 6
- Done C., Davis S. W., Jin C., Blaes O., Ward M., 2012, MNRAS 420, 1848
- Done C., Jin C., 2015, ArXiv e-prints
- Drew J., Verbunt F., 1985, MNRAS 213, 191
- Echevarria J., 1988, MNRAS 233, 513
- Edelson R., Gelbord J. M., Horne K., McHardy I. M. et al., 2015, ApJ 806, 129
- Edge D. O., Shakeshaft J. R., McAdam W. B., Baldwin J. E., Archer S., 1959, MmRA 68, 37
- Eggleton P. P., 1983, ApJ 268, 368
- Ehman J. R., Dixon R. S., Kraus J. D., 1970, AJ 75, 351
- Ekers J. A., 1969, Australian Journal of Physics Astrophysical Supplement 7
- Elitzur M., 2012, ApJ Letters 747, L33
- Elitzur M., Ho L. C., Trump J. R., 2014, MNRAS 438, 3340
- Elvis M., 2000, ApJ 545, 63
- Elvis M., Wilkes B. J., McDowell J. C., Green R. F. et al., 1994, ApJs 95, 1
- Emmanoulopoulos D., Papadakis I. E., Dovčiak M., McHardy I. M., 2014, MNRAS 439, 3931
- Emmanoulopoulos D., Papadakis I. E., McHardy I. M., Arévalo P. et al., 2012, MNRAS 424, 1327
- Eracleous M., Halpern J. P., 1994, ApJs 90, 1
- Fabian A. C., 2012, ARAA 50, 455
- Fabian A. C., Kunieda H., Inoue S., Matsuoka M. et al., 1994, PASJ 46, L59

- Fabian A. C., Nandra K., Reynolds C. S., Brandt W. N. et al., 1995, MNRAS 277, L11
- Fath E. A., 1909, Lick Observatory Bulletin 5, 71
- Feldmeier A., 1995, A&A 299, 523
- Fender R. P., 2001, MNRAS 322, 31
- Fender R. P., Belloni T. M., Gallo E., 2004, MNRAS 355, 1105
- Fender R. P., Gallo E., Russell D., 2010, MNRAS 406, 1425
- Ferrarese L., Merritt D., 2000, ApJ Letters 539, L9
- Filiz Ak N., Brandt W. N., Hall P. B., Schneider D. P. et al., 2012, ApJ 757, 114
- Filiz Ak N., Brandt W. N., Hall P. B., Schneider D. P. et al., 2014, ApJ 791, 88
- Flohic H. M. L. G., Eracleous M., Bogdanović T., 2012, ApJ 753, 133
- Foltz C. B., Weymann R. J., Morris S. L., Turnshek D. A., 1987, ApJ 317, 450
- Frank J., King A., Raine D., 1992, Accretion power in astrophysics.
- Friend D. B., Abbott D. C., 1986, ApJ 311, 701
- Fukumura K., Tombesi F., Kazanas D., Shrader C. et al., 2015, ApJ 805, 17
- Gallagher S. C., Brandt W. N., Chartas G., Garmire G. P., 2002, ApJ 567, 37
- Gallagher S. C., Brandt W. N., Chartas G., Priddey R. et al., 2006, ApJ 644, 709
- Gallagher S. C., Brandt W. N., Sambruna R. M., Mathur S., Yamasaki N., 1999, ApJ 519, 549
- Gallo E., Fender R. P., Pooley G. G., 2003, MNRAS 344, 60
- Gandhi P., Höning S. F., Kishimoto M., 2015, ApJ 812, 113
- Gandhi P., Terashima Y., Yamada S., Mushotzky R. F. et al., 2013, ApJ 773, 51
- Ganguly R., Bond N. A., Charlton J. C., Eracleous M. et al., 2001, ApJ 549, 133
- Ganguly R., Sembach K. R., Tripp T. M., Savage B. D., Wakker B. P., 2006, ApJ 645, 868

- Gardner E., Done C., 2016, ArXiv e-prints
- Gebhardt K., Bender R., Bower G., Dressler A. et al., 2000, ApJ Letters 539, L13
- Ghosh K. K., Punsly B., 2007, ApJ Letters 661, L139
- Gibson R. R., Jiang L., Brandt W. N., Hall P. B. et al., 2009, ApJ 692, 758
- Gierliński M., Done C., 2004, MNRAS 349, L7
- Gierliński M., Done C., 2006, MNRAS 371, L16
- Giustini M., Cappi M., Chartas G., Dadina M. et al., 2011, A&A 536, A49
- Gofford J., Reeves J. N., Braito V., Nardini E. et al., 2014, ApJ 784, 77
- Gofford J., Reeves J. N., McLaughlin D. E., Braito V. et al., 2015, MNRAS 451, 4169
- Gofford J., Reeves J. N., Tombesi F., Braito V. et al., 2013, MNRAS 430, 60
- Goodrich R. W., 1997, ApJ 474, 606
- Goodrich R. W., Miller J. S., 1995, ApJ Letters 448, L73
- Green A. R., McHardy I. M., Lehto H. J., 1993, MNRAS 265, 664
- Green P. J., Aldcroft T. L., Mathur S., Wilkes B. J., Elvis M., 2001, ApJ 558, 109
- Green P. J., Mathur S., 1996, ApJ 462, 637
- Greenstein J. L., Oke J. B., 1982, ApJ 258, 209
- Groot P. J., Rutten R. G. M., van Paradijs J., 2004, A&A 417, 283
- Grupe D., Mathur S., Elvis M., 2003a, AJ 126, 1159
- Grupe D., Mathur S., Elvis M., 2003b, AJ 126, 1159
- Grupe D., Nousek J. A., 2015, AJ 149, 85
- Gu M., Cao X., 2009, MNRAS 399, 349
- Gültekin K., Richstone D. O., Gebhardt K., Lauer T. R. et al., 2009, ApJ 698, 198
- Haardt F., Maraschi L., 1991, ApJ Letters 380, L51
- Hall P. B., Anderson S. F., Strauss M. A., York D. G. et al., 2002, ApJs 141, 267

- Hall P. B., Anosov K., White R. L., Brandt W. N. et al., 2011, MNRAS 411, 2653
- Halpern J. P., 1984, ApJ 281, 90
- Hamann F., Chartas G., McGraw S., Rodriguez Hidalgo P. et al., 2013, MNRAS 435, 133
- Hamann W.-R., Koesterke L., 1998, A&A 335, 1003
- Hamann W.-R., Leuenhagen U., Koesterke L., Wessolowski U., 1992, A&A 255, 200
- Hamann W.-R., Oskinova L. M., Feldmeier A., 2008, in W.-R. Hamann, A. Feldmeier, L. M. Oskinova (eds.), Clumping in Hot-Star Winds, 75
- Hamann W.-R., Wessolowski U., Koesterke L., 1994, A&A 281, 184
- Häring N., Rix H.-W., 2004, ApJ Letters 604, L89
- Hassall B. J. M., 1985, MNRAS 216, 335
- Haug K., 1987, AP&SS 130, 91
- Hazard C., Mackey M. B., Shimmins A. J., 1963, Nature 197, 1037
- Hazard C., Morton D. C., Terlevich R., McMahon R., 1984, ApJ 282, 33
- Heap S. R., Boggess A., Holm A., Klinglesmith D. A. et al., 1978, Nature 275, 385
- Heil L. M., Vaughan S., Uttley P., 2012, MNRAS 422, 2620
- Hessman F. V., Robinson E. L., Nather R. E., Zhang E.-H., 1984, ApJ 286, 747
- Higginbottom N., Knigge C., Long K. S., Sim S. A., Matthews J. H., 2013, MNRAS 436, 1390
- Higginbottom N., Proga D., Knigge C., Long K. S. et al., 2014, ApJ 789, 19
- Hillier D. J., 1984, ApJ 280, 744
- Hillier D. J., 1991, A&A 247, 455
- Hillier D. J., Miller D. L., 1999, ApJ 519, 354
- Hoare M. G., Drew J. E., 1991, MNRAS 249, 452
- Hoare M. G., Drew J. E., 1993, MNRAS 260, 647

- Hogg J. D., Reynolds C., 2015, ArXiv e-prints
- Honeycutt R. K., Schlegel E. M., Kaitchuck R. H., 1986, ApJ 302, 388
- Hönig S. F., Kishimoto M., Tristram K. R. W., Prieto M. A. et al., 2013, ApJ 771, 87
- Horne K., 1993, Eclipse Mapping of Accretion Disks: The First Decade, 117
- Horne K., Marsh T. R., 1986, MNRAS 218, 761
- Hoyle F., Lyttleton R. A., 1939, Proceedings of the Cambridge Philosophical Society 35, 405
- Hubeny I., Agol E., Blaes O., Krolik J. H., 2000, ApJ 533, 710
- Idan I., Lasota J.-P., Hameury J.-M., Shaviv G., 2010, A&A 519, A117
- Ioannou Z., van Zyl L., Naylor T., Charles P. A. et al., 2003, A&A 399, 211
- Iwasawa K., Fabian A. C., Mushotzky R. F., Brandt W. N. et al., 1996a, MNRAS 279, 837
- Iwasawa K., Fabian A. C., Reynolds C. S., Nandra K. et al., 1996b, MNRAS 282, 1038
- Janiuk A., Czerny B., Madejski G. M., 2001, ApJ 557, 408
- Ju W., Stone J. M., Zhu Z., 2016, ArXiv e-prints
- Kaastra J. S., Kriss G. A., Cappi M., Mehdićpour M. et al., 2014, Science 345, 64
- Kaastra J. S., Mewe R., Liedahl D. A., Komossa S., Brinkman A. C., 2000, A&A 354, L83
- Kafka S., Honeycutt R. K., 2004, AJ 128, 2420
- Kaspi S., Brandt W. N., Maoz D., Netzer H. et al., 2007, ApJ 659, 997
- King A., 2003, ApJ Letters 596, L27
- Knigge C., Baraffe I., Patterson J., 2011, ApJs 194, 28
- Knigge C., Drew J. E., 1997, ApJ 486, 445
- Knigge C., Long K. S., Blair W. P., Wade R. A., 1997, ApJ 476, 291
- Knigge C., Long K. S., Wade R. A., Baptista R. et al., 1998a, ApJ 499, 414

- Knigge C., Long K. S., Wade R. A., Baptista R. et al., 1998b, ApJ 499, 414
- Knigge C., Scaringi S., Goad M. R., Cottis C. E., 2008, MNRAS 386, 1426
- Knigge C., Woods J. A., Drew J. E., 1995, MNRAS 273, 225
- Konigl A., Kartje J. F., 1994, ApJ 434, 446
- Koratkar A., Blaes O., 1999, PASP 111, 1
- Körding E., Rupen M., Knigge C., Fender R. et al., 2008, Science 320, 1318
- Körding E. G., Jester S., Fender R., 2006, MNRAS 372, 1366
- Kormendy J., Ho L. C., 2013, ARAA 51, 511
- Kotani T., Ebisawa K., Dotani T., Inoue H. et al., 2000, ApJ 539, 413
- Kotov O., Churazov E., Gilfanov M., 2001, MNRAS 327, 799
- Kraft R. P., Mathews J., Greenstein J. L., 1962, ApJ 136, 312
- Kriss G. A., Krolik J. H., Otani C., Espey B. R. et al., 1996, ApJ 467, 629
- Krolik J. H., Begelman M. C., 1986, in Bulletin of the American Astronomical Society, Vol. 18 of *BAAS*, 903
- Krolik J. H., Kriss G. A., 2001, ApJ 561, 684
- Krolik J. H., Voit G. M., 1998, ApJ Letters 497, L5
- Kudoh T., Shibata K., 1997, ApJ 474, 362
- Kurosawa R., Proga D., 2009, ApJ 693, 1929
- Kusterer D.-J., Nagel T., Hartmann S., Werner K., Feldmeier A., 2014, A&A 561, A14
- Kuulkers E., Motta S., Kajava J., Homan J. et al., 2015, The Astronomer's Telegram 7647
- La Dous C., 1989, MNRAS 238, 935
- Lamy H., Hutsemékers D., 2000, A&A 356, L9
- Laor A., 1991, ApJ 376, 90

- Laor A., Brandt W. N., 2002, ApJ 569, 641
- Laor A., Davis S. W., 2014, MNRAS 438, 3024
- Lasota J.-P., 2001, NAR 45, 449
- Lazarova M. S., Canalizo G., Lacy M., Sajina A., 2012, ApJ 755, 29
- Liebert J., Stockman H. S., 1985, in D. Q. Lamb, J. Patterson (eds.), *Cataclysmic Variables and Low-Mass X-ray Binaries*, Vol. 113 of *Astrophysics and Space Science Library*, p. 151
- Long K. S., Blair W. P., Davidsen A. F., Bowers C. W. et al., 1991, ApJ Letters 381, L25
- Long K. S., Knigge C., 2002, ApJ 579, 725
- Long K. S., Wade R. A., Blair W. P., Davidsen A. F., Hubeny I., 1994, ApJ 426, 704
- Lucy L. B., Solomon P. M., 1970, ApJ 159, 879
- Lusso E., Worseck G., Hennawi J. F., Prochaska J. X. et al., 2015, MNRAS 449, 4204
- Lynden-Bell D., 1969, Nature 223, 690
- Lyubarskii Y. E., 1997, MNRAS 292, 679
- MacGregor K. B., Hartmann L., Raymond J. C., 1979, ApJ 231, 514
- Madau P., Ghisellini G., Fabian A. C., 1994, MNRAS 270, L17
- Magdziarz P., Blaes O. M., Zdziarski A. A., Johnson W. N., Smith D. A., 1998, MNRAS 301, 179
- Magorrian J., Tremaine S., Richstone D., Bender R. et al., 1998, AJ 115, 2285
- Mangham S. W., Knigge C., Matthews J. H., Long K. S. et al., 2016, in prep.
- Marinucci A., Bianchi S., Matt G., Alexander D. M. et al., 2016, MNRAS 456, L94
- Marscher A. P., 2006, in P. A. Hughes, J. N. Bregman (eds.), *Relativistic Jets: The Common Physics of AGN, Microquasars, and Gamma-Ray Bursts*, Vol. 856 of *American Institute of Physics Conference Series*, p. 1
- Marsh T. R., Horne K., 1990, ApJ 349, 593

- Marziani P., Sulentic J. W., Zwitter T., Dultzin-Hacyan D., Calvani M., 2001, ApJ 558, 553
- Mathur S., Green P. J., Arav N., Brotherton M. et al., 2000, ApJ Letters 533, L79
- Matt G., Guainazzi M., Maiolino R., 2003, MNRAS 342, 422
- Matthews J. H., Knigge C., Long K. S., Sim S. A., Higginbottom N., 2015, MNRAS 450, 3331
- Matthews J. H., Knigge C., Long K. S., Sim S. A. et al., 2016, MNRAS
- Matzeu G. A., Reeves J. N., Nardini E., Braito V. et al., 2016, MNRAS 458, 1311
- Mauche C. W., 1996, ArXiv Astrophysics e-prints
- Mauche C. W., Raymond J. C., 1987, ApJ 323, 690
- McConnell N. J., Ma C.-P., 2013, ApJ 764, 184
- McHardy I. M., Koerding E., Knigge C., Uttley P., Fender R. P., 2006, Nature 444, 730
- McHardy I. M., Papadakis I. E., Uttley P., 1999, Nuclear Physics B Proceedings Supplements 69, 509
- Merloni A., Heinz S., di Matteo T., 2003, MNRAS 345, 1057
- Mihalas D., 1978, Stellar atmospheres /2nd edition/
- Miller L., Turner T. J., 2013, ApJ Letters 773, L5
- Miller L., Turner T. J., Reeves J. N., 2008, A&A 483, 437
- Misawa T., Charlton J. C., Eracleous M., Ganguly R. et al., 2007, ApJs 171, 1
- Misawa T., Eracleous M., Chartas G., Charlton J. C., 2008, ApJ 677, 863
- Misra R., Kembhavi A. K., 1998, ApJ 499, 205
- Mitsuda K., Inoue H., Nakamura N., Tanaka Y., 1989, PASJ 41, 97
- Morabito L. K., Dai X., Leighly K. M., Sivakoff G. R., Shankar F., 2013, ArXiv e-prints
- Morgan C. W., Kochanek C. S., Morgan N. D., Falco E. E., 2010, ApJ 712, 1129

- Motta S., Beardmore A., Oates S., Sanna N. P. M. K. A. et al., 2015, The Astronomer's Telegram 7665
- Muñoz-Darias T., Coriat M., Plant D. S., Ponti G. et al., 2013, MNRAS 432, 1330
- Murray N., Chiang J., 1996, Nature 382, 789
- Murray N., Chiang J., 1997, ApJ 474, 91
- Murray N., Chiang J., Grossman S. A., Voit G. M., 1995, ApJ 451, 498
- Nandra K., Pounds K. A., 1994, MNRAS 268, 405
- Narayan R., McClintock J. E., 2012, MNRAS 419, L69
- Narayan R., McClintock J. E., Tchekhovskoy A., 2014, Energy Extraction from Spinning Black Holes Via Relativistic Jets, 523
- Narayan R., Yi I., 1994, ApJ Letters 428, L13
- Narayan R., Yi I., 1995, ApJ 452, 710
- Nardini E., Reeves J. N., Gofford J., Harrison F. A. et al., 2015, Science 347, 860
- Nestor D., Hamann F., Rodriguez Hidalgo P., 2008, MNRAS 386, 2055
- Netzer H., 1990, in R. D. Blandford, H. Netzer, L. Woltjer, T. J.-L. Courvoisier, M. Mayor (eds.), Active Galactic Nuclei, p. 57
- Neugebauer G., Oke J. B., Becklin E. E., Matthews K., 1979, ApJ 230, 79
- Noebauer U. M., Long K. S., Sim S. A., Knigge C., 2010, ApJ 719, 1932
- North M., Knigge C., Goad M., 2006, MNRAS 365, 1057
- O'Dowd M. J., Bate N. F., Webster R. L., Labrie K., Rogers J., 2015, ArXiv e-prints
- Orr A., Molendi S., Fiore F., Grandi P. et al., 1997, A&A 324, L77
- Orr M. J. L., Browne I. W. A., 1982, MNRAS 200, 1067
- Osaki Y., 1974, PASJ 26, 429
- Otani C., Kii T., Reynolds C. S., Fabian A. C. et al., 1996, PASJ 48, 211
- Ouyed R., Pudritz R. E., 1997, ApJ 482, 712

- Owocki S., 2014, ArXiv e-prints
- Owocki S. P., Castor J. I., Rybicki G. B., 1988, ApJ 335, 914
- Owocki S. P., Rybicki G. B., 1984, ApJ 284, 337
- Owocki S. P., Rybicki G. B., 1985, ApJ 299, 265
- Parmar A. N., Oosterbroek T., Boirin L., Lumb D., 2002, A&A 386, 910
- Patterson J., 1984, ApJs 54, 443
- Patterson J., 1994, PASP 106, 209
- Patterson J., Patino R., Thorstensen J. R., Harvey D. et al., 1996, AJ 111, 2422
- Pauldrach A., Puls J., Kudritzki R. P., 1986, A&A 164, 86
- Pauldrach A. W. A., Kudritzki R. P., Puls J., Butler K., Hunsinger J., 1994, A&A 283, 525
- Pelletier G., Pudritz R. E., 1992, ApJ 394, 117
- Penrose R., Floyd R. M., 1971, Nature Physical Science 229, 177
- Pereyra N. A., Kallman T. R., Blondin J. M., 1997, ApJ 477, 368
- Perley R. A., Dreher J. W., Cowan J. J., 1984, ApJ Letters 285, L35
- Ponti G., Fender R. P., Begelman M. C., Dunn R. J. H. et al., 2012, MNRAS 422, L11
- Potash R. I., Wardle J. F. C., 1980, ApJ 239, 42
- Pounds K., Lobban A., Reeves J., Vaughan S., 2016, MNRAS 457, 2951
- Pounds K. A., Nandra K., Stewart G. C., Leighly K., 1989, MNRAS 240, 769
- Pounds K. A., Reeves J. N., 2009, MNRAS 397, 249
- Prinja R. K., Smith L. J., 1992, A&A 266, 377
- Proga D., 2003, ApJ 585, 406
- Proga D., 2005, in J.-M. Hameury, J.-P. Lasota (eds.), The Astrophysics of Cataclysmic Variables and Related Objects, Vol. 330 of *Astronomical Society of the Pacific Conference Series*, 103

- Proga D., Kallman T. R., 2004, ApJ 616, 688
- Proga D., Kallman T. R., Drew J. E., Hartley L. E., 2002, ApJ 572, 382
- Proga D., Stone J. M., Drew J. E., 1998, MNRAS 295, 595
- Proga D., Stone J. M., Kallman T. R., 2000, ApJ 543, 686
- Puccetti S., Fiore F., Risaliti G., Capalbi M. et al., 2007, MNRAS 377, 607
- Puebla R. E., Diaz M. P., Hillier D. J., Hubeny I., 2011, ApJ 736, 17
- Randall S. W., Forman W. R., Giacintucci S., Nulsen P. E. J. et al., 2011, ApJ 726, 86
- Read J. I., Trentham N., 2005, Philosophical Transactions of the Royal Society of London Series A 363
- Reeves J. N., O'Brien P. T., Ward M. J., 2003, ApJ Letters 593, L65
- Reeves J. N., Wynn G., O'Brien P. T., Pounds K. A., 2002, MNRAS 336, L56
- Reichard T. A., Richards G. T., Hall P. B., Schneider D. P. et al., 2003, AJ 126, 2594
- Reynolds C. S., 1999, in J. Poutanen, R. Svensson (eds.), High Energy Processes in Accreting Black Holes, Vol. 161 of *Astronomical Society of the Pacific Conference Series*, 178
- Reynolds C. S., Fabian A. C., 1995, MNRAS 273, 1167
- Ringwald F. A., Naylor T., 1998, AJ 115, 286
- Risaliti G., Elvis M., Fabbiano G., Baldi A. et al., 2007, ApJ Letters 659, L111
- Risaliti G., Elvis M., Nicastro F., 2002, ApJ 571, 234
- Risaliti G., Salvati M., Marconi A., 2011, MNRAS 411, 2223
- Romanova M. M., Ustyugova G. V., Koldoba A. V., Chechetkin V. M., Lovelace R. V. E., 1997, ApJ 482, 708
- Ross R. R., Fabian A. C., 2005, MNRAS 358, 211
- Rottenberg J. A., 1952, MNRAS 112, 125
- Rupke D. S. N., Veilleux S., 2011, ApJ Letters 729, L27

- Rutten R. G. M., van Paradijs J., Tinbergen J., 1992, A&A 260, 213
- Sabra B. M., Hamann F., 2001, ApJ 563, 555
- Scaringi S., Körding E., Uttley P., Knigge C. et al., 2012, MNRAS 421, 2854
- Scaringi S., Maccarone T. J., Koerding E., Knigge C. et al., 2015, ArXiv e-prints
- Schechter P., 1976, ApJ 203, 297
- Schmidt M., 1963, Nature 197, 1040
- Schmidt M., 1965a, ApJ 141, 1295
- Schmidt M., 1965b, ApJ 141, 1
- Schmutz W., 1997, A&A 321, 268
- Setti G., Woltjer L., 1989, A&A 224, L21
- Seyfert C. K., 1943, ApJ 97, 28
- Shakura N. I., Sunyaev R. A., 1973, A&A 24, 337
- Shankar F., Calderone G., Knigge C., Matthews J. et al., 2016, ApJ Letters 818, L1
- Shaviv G., Wehrse R., 1991, A&A 251, 117
- Shen Y., Ho L. C., 2014, Nature 513, 210
- Shen Y., Richards G. T., Strauss M. A., Hall P. B. et al., 2011, ApJs 194, 45
- Shi Y., Rieke G. H., Smith P., Rigby J. et al., 2010, ApJ 714, 115
- Shlosman I., Vitello P., 1993, ApJ 409, 372
- Silk J., Rees M. J., 1998, A&A 331, L1
- Silva C., Uttley P., Costantini E., 2015, in The Extremes of Black Hole Accretion, 63
- Sim S. A., Drew J. E., Long K. S., 2005, MNRAS 363, 615
- Sim S. A., Long K. S., Miller L., Turner T. J., 2008, MNRAS 388, 611
- Sim S. A., Miller L., Long K. S., Turner T. J., Reeves J. N., 2010a, MNRAS 404, 1369
- Sim S. A., Proga D., Kurosawa R., Long K. S. et al., 2012, MNRAS 426, 2859

- Sim S. A., Proga D., Miller L., Long K. S., Turner T. J., 2010b, MNRAS 408, 1396
- Simon L. E., Hamann F., 2010, MNRAS 409, 269
- Sluse D., Hutsemékers D., Anguita T., Braibant L., Riaud P., 2015, ArXiv e-prints
- Smak J., 1981, ACTAA 31, 395
- Sobolewska M. A., Siemiginowska A., Gierliński M., 2011, MNRAS 413, 2259
- Soltan A., 1982, MNRAS 200, 115
- Somerville R. S., Primack J. R., Faber S. M., 2001, MNRAS 320, 504
- Springel V., Di Matteo T., Hernquist L., 2005, ApJ Letters 620, L79
- Stalin C. S., Srianand R., Petitjean P., 2011, MNRAS 413, 1013
- Stockman H. S., Angel J. R. P., Miley G. K., 1979, ApJ Letters 227, L55
- Strateva I., Ivezić Ž., Knapp G. R., Narayanan V. K. et al., 2001, AJ 122, 1861
- Struve O., 1935, ApJ 81, 66
- Suleimanov V., Hertfelder M., Werner K., Kley W., 2014, ArXiv e-prints
- Sulentic J. W., Zwitter T., Marziani P., Dultzin-Hacyan D., 2000, ApJ Letters 536, L5
- Surdej J., Hutsemekers D., 1987, A&A 177, 42
- Thorne K. S., 1974, ApJ 191, 507
- Tohline J. E., Osterbrock D. E., 1976, ApJ Letters 210, L117
- Tombesi F., Cappi M., Reeves J. N., Palumbo G. G. C. et al., 2010, A&A 521, A57
- Tombesi F., Meléndez M., Veilleux S., Reeves J. N. et al., 2015, Nature 519, 436
- Tran H. D., 2001, ApJ Letters 554, L19
- Trump J. R., Hall P. B., Reichard T. A., Richards G. T. et al., 2006, ApJs 165, 1
- Ueda Y., Inoue H., Tanaka Y., Ebisawa K. et al., 1998, ApJ 492, 782
- Urrutia T., Becker R. H., White R. L., Glikman E. et al., 2009, ApJ 698, 1095
- Urry C. M., Padovani P., 1995, PASP 107, 803

- Ustyugova G. V., Koldoba A. V., Romanova M. M., Chechetkin V. M., Lovelace R. V. E., 1999, ApJ 516, 221
- Uttley P., Cackett E. M., Fabian A. C., Kara E., Wilkins D. R., 2014, AAPR 22, 72
- Uttley P., McHardy I. M., 2001, MNRAS 323, L26
- Uttley P., McHardy I. M., Vaughan S., 2005, MNRAS 359, 345
- Šurlan B., Hamann W.-R., Kubát J., Oskinova L. M., Feldmeier A., 2012, A&A 541, A37
- Van de Sande M., Scaringi S., Knigge C., 2015, MNRAS 448, 2430
- Voit G. M., Weymann R. J., Korista K. T., 1993, ApJ 413, 95
- Wade R. A., 1984, MNRAS 208, 381
- Wade R. A., 1988, ApJ 335, 394
- Walton D. J., Miller J. M., Harrison F. A., Fabian A. C. et al., 2013, ApJ Letters 773, L9
- Wang B., Han Z., 2012, NAR 56, 122
- Warner B., 2003, Cataclysmic Variable Stars
- Weymann R. J., Morris S. L., Foltz C. B., Hewett P. C., 1991, ApJ 373, 23
- White N. E., Stella L., Parmar A. N., 1988, ApJ 324, 363
- Wills B. J., Brotherton M. S., 1995, ApJ Letters 448, L81
- Woltjer L., 1959, ApJ 130, 38
- Woods D. T., Klein R. I., Castor J. I., McKee C. F., Bell J. B., 1996, ApJ 461, 767
- Yong S. Y., Webster R. L., King A. L., 2016, PASA 33, e009
- Zakamska N. L., Strauss M. A., Krolik J. H., Collinge M. J. et al., 2003, AJ 126, 2125
- Zanstra H., 1929, Publications of the Dominion Astrophysical Observatory Victoria 4, 209
- Zhang S. N., Cui W., Chen W., 1997, ApJ Letters 482, L155

Zhou H., Wang T., Wang H., Wang J. et al., 2006, ApJ 639, 716

Zubovas K., King A., 2013, ApJ 769, 51